2016

The development of a silicon detector quality assurance system for high dose rate brachytherapy

Anthony A. Espinoza
University of Wollongong

THE DEVELOPMENT OF A SILICON DETECTOR QUALITY ASSURANCE SYSTEM FOR HIGH DOSE RATE BRACHYTHERAPY

A dissertation submitted in fulfilment of
the requirements for the award of the degree of

Doctor of Philosophy

from

UNIVERSITY OF WOLLONGONG

by

Anthony A. Espinoza

B.Med. Rad. Physics
M.Sci. (Research)

School of Engineering Physics
Faculty of Engineering

2016

CERTIFICATION

I, Anthony A. Espinoza, declare that this thesis, submitted in fulfilment of the requirements for the award of Doctor of Philosophy, in the School of Engineering Physics, Faculty of Engineering, University of Wollongong, is wholly my own work unless otherwise referenced or acknowledged. The document has not been submitted for qualifications at any other academic institution.

Anthony A. Espinoza
February 2016

Table of Contents

List of Tables

List of Figures

List of Abbreviations

^{192}Ir Iridium-192

2D Two-dimensional

3D Three dimensional

AAPM American Association of Physicists in Medicine

ACPSEM Australasian College of Physical Scientists and Engineers in Medicine

ADC Analogue-to-Digital Converter

AFE Analog Front End

DAQ Data Acquisition

FOV Field of View

FPGA Field Programmable Gate Array

LINAC Linear Accelerator

MP The Magic Plate

MPh The Magic Phantom

PMMA Polymethylmethacrylate

PSD Plastic scintillator detector

PVC Polyvinyl chloride

SDD Source-to-Detector Distance

TG43-U1 Task Group 43 Update

TPS Treatment Planning System

TRUS Transrectal ultrasound

USB Universal Serial Bus

The development of a silicon detector quality assurance system for high dose rate brachytherapy

Anthony A. Espinoza

A Thesis for Doctorate of Philosophy

School of Engineering Physics
University of Wollongong

ABSTRACT

Prostate cancer was the most commonly diagnosed cancer in males in Australia in 2012, with over 18,560 cases. It is estimated that 1 in 9 men in Australia will develop prostate cancer at one time in their lives, with the risk of being diagnosed by age of 85 close to 1 in 5. In 2011 – 2012, over 2000 prostate cancer patients were treated by radiation therapy. Brachytherapy accounted for 62% of radiotherapy procedures in prostate cancer-related hospitalisations over this period.

High Dose Rate (HDR) brachytherapy is the temporary insertion of a radioactive source directly in or close to a tumour. Small, hollow catheters are inserted into the treatment region and a remote afterloader is used to drive the highly active radiation source through each catheter to deliver dose. The remote afterloader fully controls the placement of the source, by driving it to planned points inside of each catheter, for an amount of time determined to deliver the planned dose to the tumour.

As there can be complications resulting from an incorrect treatment of HDR brachytherapy, it is essential that methods and instrumentation for quality assurance (QA) are available to medical physicists. Direct and accurate verification the treatment plan delivery and the functionality of the remote afterloader are of paramount importance in ensuring appropriate treatment. Currently, there are no comprehensive QA solutions available for HDR brachytherapy.

This aim of this thesis is to develop a novel HDR QA system, the "Magic Plate", using an 11×11 array of silicon epitaxial diodes, fast readout electronics and a software tool kit, capable of triangulating the HDR source position in three-dimensions. A HDR brachytherapy specialised casing, the "Magic Phantom", was designed and tested for pretreatment delivery confirmation of any HDR brachytherapy plan. A feasibility study was performed to assess the "Magic Plate" in real-time verification during patient treatment.

KEYWORDS: High dose rate brachytherapy, quality assurance, diode array

Acknowledgements

I would like to acknowledge all those who have supported and assisted me during my research and helping me complete this PhD.

First and foremost, I would like to express my appreciation and gratitude to my primary supervisor, Professor Anatoly Rosenfeld. Without his guidance, continuous support and encouragement, this thesis would not have been possible. Under his supervision, this project was given a firm direction from the start and and would provide good discussion and ideas to problems encountered.

I would like to thank Dr. Marco Petasecca for his all his support that he has given me over the course of both my Masters and PhD degrees. His supervision, advice and endless assistance allowed this project to reach its potential. His mentoring and friendship was essential in me becoming a researcher and preparing me for my career ahead. He is an expert in detectors and electronics, and had designed the data acquisition systems used throughout my PhD.

My thanks to Dr. Stephanie Corde-Tehei for being a great supporter of this project and of myself. Her involvement in every step of this research gave me a solid direction and helped me to improve this work. She was always there to facilitate experiment sessions, provide feedback on articles and this thesis.

I thank Mr Andrew Howie for all his assistance and time he gave to this project. He assisted in facilitating experimental sessions, use of the treatment planning systems and also provided valuable feedback to articles. He was an integral member of this research and helped improved the clinical relevance of this study.

I would like to thank the following people for their contribution to this project, Dr. Joseph Bucci, Associate Professor Michael Lerch, Dr. Dean Cutajar and Karen Ford. Each of these people supported myself and this work, and for this they have my appreciation.

I would like to express my gratitude for the support I received from Australian Rotary Health and the Rotary Club of Penrith Valley. It was an honour to have their assistance to undertake this project.

I would also like to thank the support of my friends and colleagues during my research. Bradley Beeksma, who worked with me on this project at the beginning. We performed the first preliminary experiments together and began the system development and preliminary design of the Magic Phantom. Iolanda Fuduli, who was responsible for the firmware side of the data acquisitions used in this project. Abdullah Aldosari, who continued my Masters research and we worked together in using the CMRP detector systems for external beam radiotherapy during my research.

Michael Weaver, who guided me during my learning of C++ and software design. His extensive knowledge of communication between electronics and software was a great resource whenever I encountered problems during development. Matthew Newall and Mitchell Duncan, who were the first users of the software I had developed, apart from myself, and helped me apply my work to their projects and overall improve the quality of the software. Special thanks to Lachlan Chartier for all his efforts reading and helping to improve the writing of my thesis and journal publications.

I would like to thank my friends and family, for without their support I would not have been able to undertake or complete this work. Finally, I would like to thank my partner Mel for her love, encouragement and for her extensive work on this thesis.

List of Publications

M. Petasecca, A. Cullen, I. Fuduli, **A. Espinoza**, C. Porumb, C. Stanton, A. H. Aldosari, E. Bräuer-Krisch, H. Requardt, A. Bravin, V. Perevertaylo, A. B. Rosenfeld, and M. L. F. Lerch, "X-Tream: a novel dosimetry system for Synchrotron Microbeam Radiation Therapy," *J. Instrum.*, vol. 7, no. 07, pp. P07022-P07022, Jul. 2012.

P. Metcalfe, A. Quinn, K. Loo, M. Lerch, M. Petasecca, J. Wong, N. Hardcastle, M. Carolan, J. McNamara, D. Cutajar, I. Fuduli, **A. Espinoza**, C. Porumb, and A. Rosenfeld, "Review of four novel dosimeters developed for use in radiotherapy," *J. Phys. Conf. Ser.*, vol. 444, p. 012008, Jun. 2013.

A. Espinoza, B. Beeksma, M. Petasecca, I. Fuduli, C. Porumb, D. Cutajar, S. Corde, M. Jackson, M. L. F. Lerch, and A. B. Rosenfeld, "The feasibility study and characterization of a two-dimensional diode array in 'magic phantom' for high dose rate brachytherapy quality assurance.," *Med. Phys.*, vol. 40, no. 11, p. 111702, Nov. 2013.

A. H. Aldosari, **A. Espinoza**, D. Robinson, I. Fuduli, C. Porumb, S. Alshaikh, M. Carolan, M. L. F. Lerch, V. Perevertaylo, A. B. Rosenfeld, and M. Petasecca, "Characterization of an Innovative p-type Epitaxial Diode for Dosimetry in Modern External Beam Radiotherapy," *IEEE Trans. Nucl. Sci.*, vol. 60, no. 6, pp. 4705-4712, Dec.

2013.

I. Fuduli, M. K. Newall, **A. Espinoza**, C. S. Porumb, M. Carolan, M. L. F. Lerch, P. Metcalfe, A. B. Rosenfeld, and M. Petasecca, "Multichannel Data Acquisition System comparison for Quality Assurance in external beam radiation therapy," *Radiat. Meas.*, pp. 7-10, Jun. 2014.

I. Fuduli, C. Porumb, **A. Espinoza**, A. H. Aldosari, M. Carolan, M. L. F. Lerch, P. Metcalfe, A B. Rosenfeld, and M. Petasecca, "A comparative analysis of multichannel Data Acquisition Systems for quality assurance in external beam radiation therapy," *J. Instrum.*, vol. 9, no. 06, pp. T06003-T06003, Jun. 2014.

A. H. Aldosari, M. Petasecca, **A. Espinoza**, M. K. Newall, I. Fuduli, C. Porumb, Alshaikh, S., Alrowaili, Z. a., Weaver, M., Metcalfe, P., Carolan, M., Lerch, M. L. F., Perevertaylo, V., A. B. Rosenfeld, "A two dimensional silicon detectors array for quality assurance in stereotactic radiotherapy: MagicPlate-512." *Med. Phys.*, vol. 41, no. 9, p. 091707, Sept. 2014.

A. Espinoza, M. Petasecca, I. Fuduli, A. Howie, J. Bucci, S. Corde, M. Jackson, M. L. F. Lerch, and A. B. Rosenfeld, "The evaluation of a 2D diode array in 'magic phantom' for use in high dose rate brachytherapy pretreatment quality assurance.," *Med. Phys.*, vol. 42, no. 2, p. 663-673, Feb. 2015.

M. Petasecca, M. K. Newall, J. T. Booth, M. Duncan, A. H. Aldosari, I. Fuduli, **A. Espinoza**, C. Porumb, S, Guatelli, P. Metcalfe, E. Colvill, D. Cammarano, M. Carolan, B. Oborn, M. L. F. Lerch, V. Perevertaylo, P. J. Keall and A B. Rosenfeld, "MagicPlate-512: A 2D silicon detector array for quality assurance of stereotactic motion adaptive radiotherapy", *Med. Phys.*, vol. 42, no. 6, p. 2992, Jun. 2015.

A. Espinoza, M. Petasecca, D. Cutajar, I. Fuduli, A. Howie, J. Bucci, S. Corde, M. Jackson, M. Zaider, M. L. F. Lerch, and A. B. Rosenfeld, "Pretreatment verification of high dose rate brachytherapy plans using the "magic phantom" system.," *Biomedical Physics & Engineering Express.*, vol. 1, no. 2, 025201, Jul. 2015.

List of Conference Presentations

Anthony Espinoza, M. Petasecca, B. Beeksma, D. Cutajar, S. Corde, S. Downes, M. Jackson, J. Bucci and A. Rosenfeld, "A quality assurance system for high dose rate brachytherapy", Australasian Brachytherapy Group, 21st Annual Meeting, Canberra, March 2012.

Anthony Espinoza, M. Petasecca, B. Beeksma, D. Cutajar, S. Corde, S. Downes, M. Jackson, J. Bucci and A. Rosenfeld, "A quality assurance system for high dose rate brachytherapy", IEEE NSS/MIC, Anaheim, United States, November 2012.

Anthony Espinoza, M. Petasecca, B. Beeksma, D. Cutajar, S. Corde, S. Downes, M. Jackson, J. Bucci and A. Rosenfeld, "A quality assurance system for high dose rate brachytherapy", Engineers in Physics and Medicine, Gold Coast, December 2012.

Anthony Espinoza, D. Cutajar, S.Guatelli, M. Petasecca, M.L.F Lerch and A. Rosenfeld, "A Monte Carlo simulation study of a novel QA system for HDR Brachytherapy", Monte Carlo Workshop, University of Wollongong, Wollongong, April 2013.

Anthony Espinoza, M. Petasecca, D. Cutajar, S. Corde, A. Howie, M. Jackson, J.

Bucci and A. Rosenfeld, "BrachyPix: A quality assurance system for high dose rate brachytherapy", Australasian Brachytherapy Group, 23st Annual Meeting, Adelaide, February 2014.

Anthony Espinoza, M. Petasecca, I. Fuduli, S. Corde, A. Howie, J. Bucci, M. Jackson, M.L.F. Lerch and A. Rosenfeld, "An investigation into the transit motion of a stepping HDR source using a 2D silicon diode array", Australasian College of Physical Scientists & Engineers in Medicine Medical Physics, Sydney, December 2014.

Anthony Espinoza, M. Petasecca, I. Fuduli, A. Howie, S. Corde, J. Bucci, M. Jackson, M.L.F. Lerch and A. Rosenfeld, ""Magic phantom" - a quality assurance system for high dose rate brachytherapy", European Society for Radiotherapy & Oncology 3rd ESTRO Forum, Barcelona, Spain, April 2015.

Chapter 1

Introduction

Prostate cancer is the second largest cause of cancer-related death developed by men in Australia after lung cancer. It is estimated that 1 in 8 men in Australia will develop prostate cancer by the age of 75, with the risk of being diagnosed by the age of 85 closer to 1 in 5 [1, 2]. Prostate cancer can be curable when detected early, and appropriate treatment can be recommended in consideration of the patient's age and case severity. The treatment options for prostate cancer in Australia are typically surgical removal of the whole prostate or radiation therapy [3].

High Dose Rate (HDR) Brachytherapy is a form of internal radiation therapy that can be used to treat many types of cancers, and is widely used for the treatment of prostate cancer. It can be used to effectively target the tumour with minimal dose to adjacent organs, such as the bladder and rectum, because the dose decreases very rapidly with increased distance from the source. In HDR brachytherapy, thin close-ended catheters are temporarily inserted into the prostate under ultrasound image guidance. A single high-intensity source, typically ^{192}Ir, at the end of a flexible steel cable is connected to a mechanical delivery device known as the remote afterloader, which is controlled outside the treatment room. The remote afterloader transports

the source through each catheter, one after another, to preplanned positions inside the tumour for a the time duration needed to achieve the total prescribed dose. By having millimetre precision on the inserted source position, HDR brachytherapy provides the best opportunity to shape and control the final dose delivered to the tumour.

Dose escalation in HDR brachytherapy essentially increases tumour control [4] but requires strict quality assurance (QA) guidelines due to the extremely high risk of overdosing normal tissue. While HDR brachytherapy is generally a safe treatment, there have been many recorded incidents of incorrect treatments [5–7]. The majority of these were due to human errors, such as the inaccurate entry of source strength and prescription dose into the afterloader control, improper catheter selection, the incorrect step size selected, and the wrong transfer tubes and catheters connected [8].

While the likelihood of the remote afterloader itself malfunctioning and incorrectly administering the treatment is considered low, deviations from the treatment in dwell times and dwell positions can result in variations in absorbed dose. While it is unknown what final effect these variations may have on the patient, it has been shown that multiple interstitial catheter applicators, such as in prostate treatments, would have the highest susceptibility to these deviations [9]. The incidence of these errors could be reduced by the introduction of additional pretreatment redundancy checks between the treatment planning and delivery process [10].

One of the main goals of a quality assurance program for HDR brachytherapy is to ensure that patient treatments are consistently administered correctly by the remote afterloader. An accurate treatment delivery means that the source is driven to the planned position, inside the correct applicator, and for the correct amount of time, ensuring the calculated absorbed dose matches the prescription set by the radiation

oncologist [11, 12].

The success of the treatment is dependent on the remote afterloader positional and timing accuracy, and the verification of this is a fundamental part of an effective verification program [13,14]. Ideally, performing a confirmation of the planned delivery on each plan prior to patient treatment would ensure that there are no deviations from the source dwell positions and times at the time of treatment. For a pretreatment plan delivery verification system to be feasible in a clinical setting, it should be quick to perform and require minimal personnel.

The ultimate goal in HDR brachytherapy quality assurance is the ability to assess the source delivery and delivered dose while the patient is being treated in real time, referred to as *in-vivo* verification. Previous studies have had limited successes in this area due to the large uncertainties and difficulty of achieving an accurate measurement.

As HDR brachytherapy treatments become increasingly complex, the need to develop delivery verification methods, such as those found in other radiation modalities, is essential to ensure the optimal treatment of patients [15]. As new technologies and techniques emerge, there is now an opportunity to develop robust quality assurance systems for this challenging problem.

1.1 Project aim

The aim of this project is address the current lack of treatment verification in HDR brachytherapy. This aim is divided into the following objectives:

- Review the current attempts in the literature to develop a quality assurance system for HDR brachytherapy;

- Design a prototype system that can be used for both pretreatment and *in-vivo* verification;
- Assess the feasibility of the prototype system and develop its use for source position determination;
- Explore its use in the verification of treatment plan delivery;
- Investigate the system's potential use in *in-vivo* verification by testing its ability to perform source tracking at large distances between the detector and source.

1.2 Thesis Structure

This thesis consists of 11 chapters that will endeavour to accomplish the aforementioned project aim and the specific objectives. At the time of thesis completion, three publications have resulted from this project:

- A. Espinoza, B. Beeksma, M. Petasecca, I. Fuduli, C. Porumb, D. Cutajar, S. Corde, M. Jackson, M. L. F. Lerch, and A. B. Rosenfeld, "The feasibility study and characterization of a two-dimensional diode array in "magic phantom" for high dose rate brachytherapy quality assurance.," Medical Physics, vol. 40, p. 111702, Nov. 2013. [16]

- A. Espinoza, M. Petasecca, I. Fuduli, A. Howie, J. Bucci, S. Corde, M. Jackson, M. L. F. Lerch, and A. B. Rosenfeld, "The evaluation of a 2D diode array in "magic phantom" for use in high dose rate brachytherapy pretreatment quality assurance," Medical Physics, vol. 42, no. 2, pp. 663-673, Feb. 2015. [17]

- A. Espinoza, M. Petasecca, D. Cutajar, I. Fuduli, A. Howie, J. Bucci, S. Corde, M. Jackson, M. Zaider, M. L. F. Lerch, and A. B. Rosenfeld, "Pretreatment verification of high dose rate brachytherapy plans using the "magic phantom" system," Biomedical Physics & Engineering Express, vol. 1, no. 2, 025201, Jul. 2015.

Results published in these papers are found in different chapters of this thesis.

Following this introduction, Chapter 2 begins by providing a background into the use of HDR brachytherapy, specifically in the field of prostate cancer. It focuses on what quality assurance practices are needed for this treatment modality and reviews devel-

opmental approaches found in the literature. As silicon detectors have been chosen as the basis for this quality assurance system, this chapter will also give a summary on the theory of semiconductors and their use in radiation detection. A condensed version of the review of developmental approaches was published in Espinoza et al. (2013) [16].

Chapter 3 gives a description of the instrumentation used in this project. It begins by describing the "Magic Plate" detector and the prototype phantom, the "Magic Phantom", designed for pretreatment verification that has been used. The principle of operation of the electronic readout, the AFE data acquisition system, is briefly explained. A software graphical user interface was developed in C++ for the communication to the readout electronics during measurement, and features a complete analysis tool kit for post-processing. The software has the ability to read DICOM files used in the planning of high dose rate brachytherapy and can also perform dose calculations based upon the TG-43U1 protocol. Description of used instrumentation was published in Espinoza et al. (2015) [17].

The first evaluation of the "Magic Plate" detector for use within HDR brachytherapy verification is found in Chapter 4. It characterises the system in terms of electronic noise, range of expected response and angular dependence. Besides identifying the possible limitations of the system, this characterisation gives the fundamental information needed to perform a three-dimensional (3D) source localisation calculation. Results from the angular dependence study were published in Espinoza et al. (2013) [16].

Chapter 5 outlines the fast iterative approach for source localisation in 3D, and the dwell position and time determination using the "Magic Plate" detector. The following chapter, Chapter 6, is the experimental evaluation of these methods, primarily focused

on their use in pretreatment verification. Description of the source tracking algorithm was published in Espinoza et al. (2013) [16]. The method for dwell position and timing determination was reported in Espinoza et al. (2015) [17].

This focus on pretreatment verification continues in the following two chapters, Chapters 8 and 9. A method for the comparison between the measured dwell position and times, and those from the treatment plan was developed and tested in Chapter 8. It features the ability to identify when treatments have been executed differently to the plan, such as when dwell positions have been introduced or removed during treatment, and dwell times have varied. The concept and results of the comparison between measured dwell positions/times to the plan were presented in Espinoza et al. (2015) [17].

Chapter 9 further develops the concept of the "Magic Plate" as a pretreatment delivery verification tool, by proposing that the times needed to perform verification can be shortened by reducing the planned prescription dose. This approach was then applied to the verification of real patient treatment plans. This work has been reported by Espinoza et al. [18].

Chapter 7 demonstrates the performance of the high speed tracking of the "Magic Plate" system, to characterise the motion of the HDR source as it moves between dwell positions. The dose delivered during this motion, known as transit dose, is generally overlooked in treatment planning. By combining the high temporal resolution of the source tracking information and the TG-43U1 protocol for dose calculations, a proof of concept for transit dose determination was shown.

The final chapter featuring experimental work, Chapter 10, discusses the feasibility of the "Magic Plate" for source tracking during patient treatment. The concept of how it is expected to be achieved is introduced, with some preliminary source tracking results reported. It considers how inhomogeneities in the body could affect this method, with measurements performed in phantom with substitute materials.

Chapter 11 concludes this thesis by providing a summary of the outcomes of each chapter, and provides recommendations for future improvements to the system.

Chapter 2

Literature review

This chapter aims to provide a background on HDR brachytherapy, specifically for the treatment of prostate cancer. It gives an overview of the prostate's anatomical location, the incidence of cancer among males in Australia, and common treatments, including the use of HDR brachytherapy. It will then examine possible mistakes or mistreatments that can arise during the delivery of brachytherapy treatment, and review current and proposed methods of quality assurance.

2.1 The prostate

The prostate is an organ that is part of the male reproductive system and is located immediately below the bladder, in front of the bowel, surrounding the urethra, as seen in Figure 2.1. Its main function is to secrete fluids that protect and enrich sperm. A healthy prostate is about the size of a walnut.

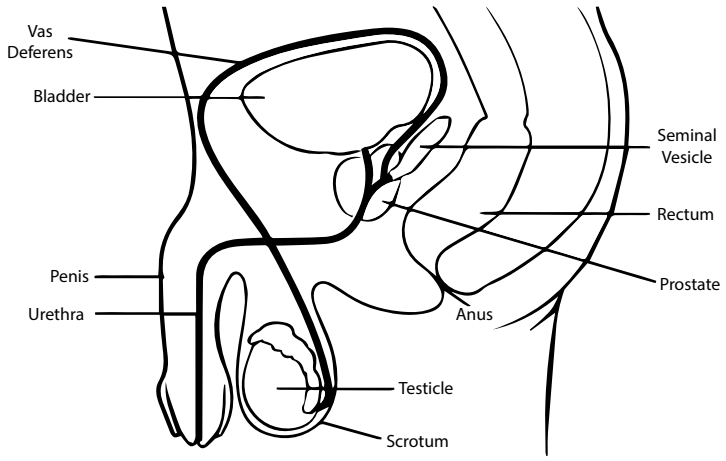

Figure 2.1: A sagittal view of the prostate relative to the male reproductive anatomy.

Prostate cancer

Prostate cancer is a disease where cells in the prostate gland become abnormal and grow uncontrollably to form tumours. Cancerous cells in the prostate are generally not deadly on their own, but are capable of metastasising; spreading to other paths of the body via the blood or lymph creating new tumours. Benign tumours do not spread but may interfere with nearby organs and structures, causing secondary problems or discomfort.

In 2011, 3,294 Australians died due to prostate cancer, making it the fourth largest cause of death for males. From 2010 to 2020, the projected number of deaths from prostate cancer is expected to increase to more than 3900 per year [1]. Prostate cancer is listed as one of the most commonly diagnosed cancers in Australia, with 21,808 new cases of prostate cancer diagnosed in 2009 alone. It is projected that the incidence rate will increase to 25,000 new cases per year in 2020. In 2008, the incidence rate in Australia was found to be higher than in all other countries [19].

The causes of prostate cancer are not clear, but it is known that age is an important

factor. It is estimated that by age 85, 1 in 5 Australian males will be diagnosed with prostate cancer [2]. Other considerations for determining the likelihood of increased risk include family history of prostate cancer, ethnicity, lifestyle and environmental factors.

Patients with localised prostate cancer i.e. cancer which has not yet metastasised, have the following options for management, depending on the severity of their case. For low severity patients, no initial treatment can be recommended with active surveillance typically performed by a general practitioner (GP). Other patients can be recommended the surgical removal of the entire prostate, known as a radical prostatectomy, or external beam radiotherapy (EBRT) and interstitial radiotherapy (brachytherapy). Brachytherapy, also known as sealed source or internal radiotherapy, accounted for 62% of radiotherapy procedures in prostate cancer-related hospitalisations between 2011 and 2012 [1].

2.2 High dose rate brachytherapy

Brachytherapy is a radiation therapy treatment where a radiation source is placed close to or inside the tumour to be irradiated. Radiation is emitted from the source in all directions, and the intensity decreases following the inverse square law and, coupled with attenuation in the material, results in steep dose gradients from the source. This treatment modality allows for a highly conformal dose to be delivered to the tumour whilst sparing surrounding healthy tissue.

High dose rate (HDR) brachytherapy is the temporal insertion of a single high activity gamma source, typically Iridium-192 (^{192}Ir), that is used to deliver the prescribed

dose within minutes. Catheters or applicators are surgically inserted directly into the prostate gland under transrectal ultrasound guidance. Once all applicators have been inserted, the patient is re-imaged and the final treatment plan is created to achieve the prescribed dose coverage.

The advantages of the use of HDR brachytherapy can be summarised as follows [10, 20–22]:

- The introduction of the radioactive source directly into the tumour allows for a highly localised radiation dose than can be typically achieved with EBRT. This gives a higher tumour control, which is generally well tolerated.
- The radiation dose attenuates approximately following the inverse square law. Surrounding healthy tissue receive low dose and side effects can be minimised.
- The overall duration of the treatment is short. Besides ease of treatment for the patient, this can also prevent proliferation of the tumour tissue.
- The total dose distribution can be highly conformed to the tumour shape, based upon the planned dwell positions and times.
- The use of remote afterloaders to control the position of the HDR source allows for much less exposure to medical personnel.
- The patient is not radioactive after receiving the treatment, as opposed to those receiving permanently implanted radiation seeds.
- Research has shown a radiobiological advantage for prostate cancer when using HDR brachytherapy compared to using EBRT.

There are, however, some disadvantages:

- As each treatment gives a large dose, there are increased risks associated with incorrect delivery or planning.
- The risk of accidental radiation exposure to patients and operators should the source fail to retract.
- The increased need for accurate dosimetric, anatomic and geometric information for planning and delivery.

2.3 Treatment planning and delivery

HDR brachytherapy treatment is recommended to patients by the radiation oncologist based upon the risk category of the case, age of the patient and localisation of the cancer growth. Prior to the procedure, the patient is placed under an anaesthetic, such as spinal, epidural or general, and using transrectal ultrasound (TRUS) imaging, the shape and size of the prostate gland is determined. Catheters are inserted into the prostate, via the perineum, under the guidance of ultrasound imaging - which can be used for intra-operative treatment planning. If this is not the case, a post-implant CT scan of the patient is used to determine the position of the catheters inside of the prostate and becomes the basis of the treatment plan.

The prostate volume, organs at risk (OAR), planning target volume (PTV) and the positions of the catheters are defined using a dedicated workstation, known as the treatment planning system (TPS). For this thesis Nucletron ONCENTRA® TPS version 4.5 (Nucletron, an Elekta company, Elekta AB, Stockholm, Sweden) was used to perform the treatment planning. The system then determines the placement and dwell times of the HDR source in each catheter that would effectively shape the dose

distribution to the prostate volume.

The catheters inside the patient are connected to the HDR treatment delivery device, known as the remote afterloader. The afterloader is used to control the placement of the ^{192}Ir source through each catheter. The ^{192}Ir source is connected to a cable wound around a drum inside the HDR afterloader. While the afterloader is not in operation, the source is housed inside a shielded lead safe in the afterloader. During treatment, the drum is rotated by stepping motors to push the source on the steel cables through a specific channel that connects to the catheter. By varying the source positions and dwell times, an integral dose distribution can be formed that conforms to the target volume of the clinical plan [23]. For patients receiving high dose rate brachytherapy as a monotherapy, the following doses have been recommended: 34 – 38 Gy in 4 fractions, 31-33 Gy in 3 fractions or 26 Gy in 2 fractions [24].

Two of the more common HDR remote afterloaders were used for the experimental components of this thesis. These were the Nucletron microSelectron® mHDR-v.2. afterloader, and the newer Nucletron Flexitron® HDR afterloader, shown in Figure 2.2, both produced by Nucletron (Nucletron, an Elekta company, Elekta AB, Stockholm, Sweden). The Nucletron microSelectron® mHDR-v.2. afterloader allows up to 30 catheters to be connected for a single treatment plan, with a selectable step size of 2.5, 5 or 10 mm, with a stated positional accuracy of ± 1 mm at each dwell position. The Nucletron Flexitron® HDR afterloader supports up to 40 catheters, with a minimum step size of 1 mm. The stated accuracy of the positioning of this device is ± 0.5 mm at each dwell position. A minimum dwell time of 0.1 s can be selected for both afterloaders.

Figure 2.2: The Nucletron microSelectron® mHDR-v.2. afterloader and the Nucletron Flexitron® HDR afterloader, produced by Nucletron (Nucletron, an Elekta company, Elekta AB, Stockholm, Sweden).

Both HDR afterloaders utilise ^{192}Ir as the radiation source, but have different capsule designs, resulting in differences to the dose distributions in water. These distributions are determined experimentally or using Monte Carlo particle transport simulations to provide the parameters for treatment planning models used in the TG-43U1 protocol. Each HDR source is modelled following their design specification to create a source specific set of TG-43U1 parameters.

The HDR afterloader theory of operation

Figure 2.3 shows a schematic of the mechanical components inside of the HDR afterloader [25]. Inside the afterloader are two separate motor and control systems, one to drive the HDR source and the other to drive the check cable. The check cable contains a welded tip made of a solid cylindrical piece of metal, shaped similar to that of the

^{192}Ir source capsule. The check cable tip does not contain any radioactive material and is used to test each transfer tube and catheter for blockages and shorter than expected catheter lengths.

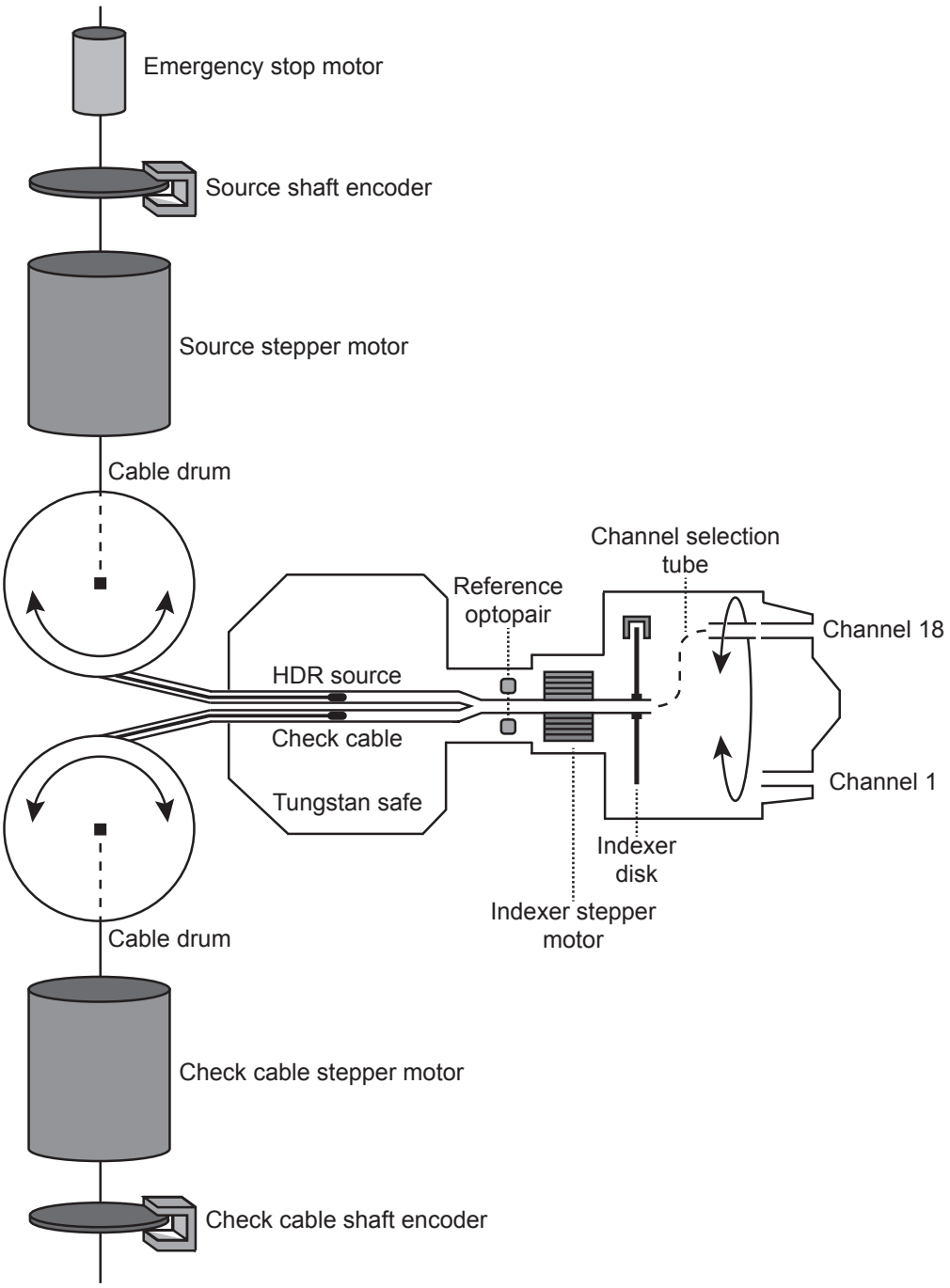

Figure 2.3: Sketch of the mechanics of the Nucletron microSelectron® mHDR-v.2. afterloader [25].

The source capsule and check cable tip are located in the afterloader's tungstan safe when not in use and the opposite end of the each cable is wound around a cable drum. Both the source and check cable are driven by independent stepper motors that are coupled to each cable drum, and are controlled by the system microprocessor. The source and check cable tip can be positioned inside of the applicator and retracted, based upon the angular rotation of the cable drum. A shaft encoder of each motor is used to verify the drum rotation, and conveys the information to the microprocessor by a series of pulses.

There are two channels inside of the safe for the source and check cable. These join into a single channel that extends to the indexer stepper motor shaft and into the selected afterloader channel, via the channel selection tube. The indexer stepper motor, controlled by the microprocessor, is used to rotate the channel selection tube to required afterloader channel. A separate encoder based upon the rotation of the indexer disk with the stepper motor is used to provide the microprocessor with the channel selected information.

The microprocessor positions the source and check cable tip, one at a time, by counting the movement steps of the stepper motor, starting from a reference point. The reference point is determined by an optopair system, which detects when the source or check cable has passed between the optopair light and sensor. The system then checks that the number of steps required to drive the cables back to the reference point corresponds to the number of steps driven out, with slight variation allowed to account for friction inside of the transfer tube and applicators.

There is an emergency stop motor that can be used to retract the source cable in the event of unacceptable differences in steps or a failure to return the source to the

safe. This motor is powered by a DC power supply with a backup battery, allowing it to operate independently from the mains power. The emergency motor is able to withdraw the source with a larger force than the stepper motor by a factor of five, increasing the chance of retracting the source.

The afterloader system features a primary timer which is used to count down from the total dwell times for all programmed dwell positions in the treatment. The secondary timer keeps a running total of all dwell times, plus source transit time to and from the safe for the movement inside of a single channel. The secondary timer must not exceed or be significantly less than the sum of the planned dwell times per channel, plus twice the source transit time within a certain tolerance. A failure of timing occurs when the maximum difference exceeds 1% or 0.1 s, causing automatic source retraction.

Both timers are managed by the afterloader system and has a minimum time unit of 0.1 s, but is accurate to 0.01 s [26]. The minimum dwell time than can be set or resolved is thus 0.1 s, which can potentially lead to rounding errors in timing.

2.4 The ^{192}Ir source

The most commonly used radioactive isotope for HDR brachytherapy is ^{192}Ir. It is produced by neutron bombardment of the stable ^{191}Ir and results in a minimal production of unwanted isotopes. Due to its high specific activity and relative ease of production, sources with very large activities can be manufactured.

Photon	Mean Energy (keV)	Intensity (gamma/ 100 decay)
X L	9.440	3.92
X Kα2	65.122	2.62
X Kα1	66.831	4.44
X Kβ3	75.368	0.531
X Kβ2	75.749	1.021
X Kβ1	77.831	0.364
γ	136.39	0.199
γ	176.98	0.0043
γ	280.27	0.008
γ	295.957	28.71
γ	308.455	29.70
γ	316.506	82.86
γ	416.468	0.67
γ	468.068	47.84
γ	485.301	0.0047
γ	588.581	4.522
γ	593.63	0.042
γ	599.41	0.0039
γ	604.411	8.216
γ	612.462	5.34
γ	765.8	0.0013
γ	884.537	0.292
γ	1061.49	0.0531
γ	1089.96	0.0012
γ	1378.5	0.0014

Table 2.1: The ^{192}Ir gamma spectra obtained from the NuDat database [27].

^{192}Ir has a half-life of 73.827 days, and for HDR brachytherapy treatment, institutions typically receive a new source with an air kerma strength of 41 mGy.m^2.h^{-1} and replace their ^{192}Ir source 3 – 4 times a year when it has decayed to 14 – 16 mGy.m^2.h^{-1}. ^{192}Ir decays by β^- emission to ^{192}Pt (95.13%) and through electron capture to ^{192}Os (4.87%). On average, 2.21 photons are emitted by both decay processes resulting in an average energy of the emitted photons of 354 keV.

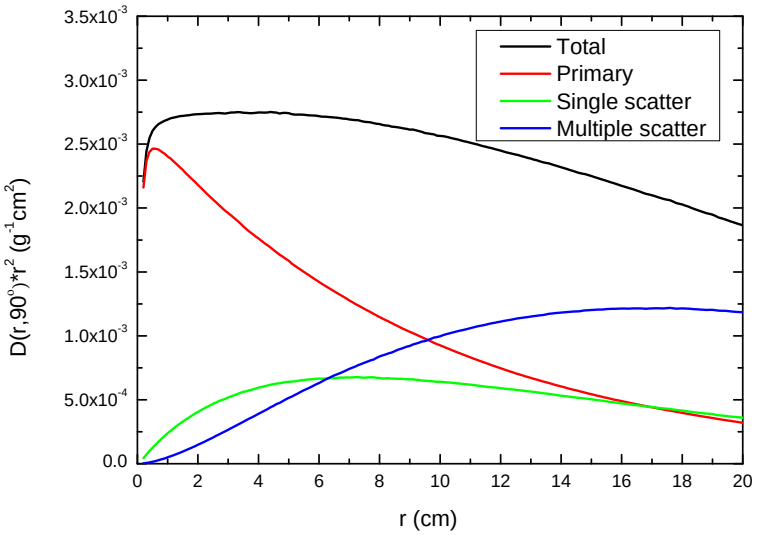

Figure 2.4: Components of ^{192}Ir dose as a function of distance. Reproduced from data obtained by Taylor and Rogers [28] for the Nucletron microSelectron® mHDR-v.2. afterloader source.

Simulations performed by Meli et al. [29] show that in a water volume the average photon energy decreases with increasing distance from the source, to 337, 258 and 221 keV at depths of 1, 5 and 10 cm, respectively. The contribution of energy deposited for the ^{192}Ir Nucletron microSelectron® mHDR-v.2. afterloader source obtained by Taylor and Rogers [28], reproduced in Figure 2.4, shows that with increasing depth there is a decrease in the dose due to primary photons emitted by the source, but a larger contribution due to single and multiple scattering. This softening of the spectra can be problematic for measurement devices and dosimeters that exhibit an energy

dependence.

2.5 The TG-43 protocol

The Radiation Therapy Committee of the American Association of Physicists in Medicine (AAPM) formed Task Group 43 and its subsequent update (TG43-U1) to recommend a dosimetry protocol for dose calculations in water and data sets for the values of dosimetry parameters for interstitial brachytherapy [30, 31]. From this arose source strength specifications, calibration standards and dose calculation definitions and equations, which form the basis of many TPS dose calculations from a single source. The geometry used for point dose calculations is seen in Figure 2.5, where r is the distance (cm) from the centre of the active source to the point of interest; r_0 is the reference distance, specified to 1 cm in this protocol; θ is the polar angle that specifies the point-of-interest $P(r, \theta)$, relative to the source longitudinal axis; and the θ_0 is the reference angle, specified to be 90°.

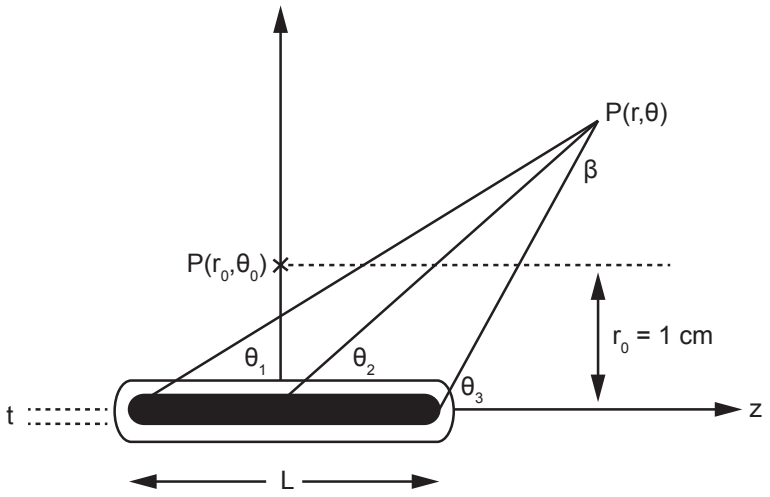

Figure 2.5: Point dose calculation using TG-43U1.

The two-dimensional dose-rate equation is described as

$$\dot{D}(r,\theta) = S_k \cdot \Lambda \cdot \frac{G_L(r_0,\theta)}{G_L(r_0,\theta_0)} \cdot g_L(r) \cdot F(r,\theta) \tag{2.1}$$

with each function having parameters that have been calculated using Monte Carlo simulation methods or by dose in water measurements.

Air Kerma Strength, S_K

The air kerma strength is defined as

$$S_K = \dot{K}_\delta(d) \cdot d^2 \tag{2.2}$$

and is the air kerma rate, $\dot{K}_\delta(d)$ in a vacuum, and due to photons of energy greater than δ, at distance d, multiplied by the square of distance, d^2. The distance, d, is typically taken at 1 m on the transverse plane, so that it is much larger in comparison to the source size to eliminate geometry effects. Corrections must be made for the effects of the attenuation and scatter in air and photon scatter from nearby media such as walls, floors and ceilings. The unit of air kerma strength is denoted by U, where 1 U = 1 μGy.m^2.h^{-1}.

Dose-rate Constant, Λ

The dose-rate constant in water is defined as

$$\Lambda = \frac{\dot{D}(r_0,\theta_0)}{S_K} \tag{2.3}$$

and is the ratio of dose rate at the reference position, $P(r_0,\theta_0)$ and S_k. This quantity relates the air kerma strength of a source to the dose rate at a reference point in a

water phantom. It is radionuclide and source model dependent, and has the units of $cGy.h^{-1}.U^{-1}$.

Geometry Factor, G(r)

The geometry factor is used to improve the accuracy of the dose rates which can be estimated by interpolation from data determined at discrete points. This factor provides an inverse square-law correction based upon the approximate spatial distribution of radioactivity in the source. For point source approximations, the geometry factor is

$$G_P(r,\theta) = \frac{1}{r^2} \tag{2.4}$$

For line source approximations, the geometry factor is calculated for two conditions

$$G_L(r,\theta) = \begin{cases} \dfrac{\beta}{L \cdot r \cdot \sin\theta} & \text{if } \theta \neq 0^\circ \\ (r^2 - L^2/4)^{-1} & \text{if } \theta = 0^\circ \end{cases} \tag{2.5}$$

where θ is angle of the source with respect to the point of calculation, L is the length of the source and β is the angle subtended by both ends of the source to the point of calculation.

Radial Dose Function, g(r)

The radial dose function, g(r), accounts for the dose fall-off on the transverse plane due to the photon attenuation and scattering through the medium. It is calculated by

$$g(r) = \frac{\dot{D}(r,\theta_0)G(r_0),\theta_0}{\dot{D}(r_0,\theta_0 G(r,\theta_0)} \tag{2.6}$$

and can be determined for both the point and line source approximations.

Anisotropy Function, F(r,θ)

The two dimensional anisotropy function, F(r,θ), is defined as

$$F(r,\theta) = \frac{\dot{D}(r,\theta)G_L(r,\theta_0)}{\dot{D}(r,\theta_0)G_L(r,\theta)} \tag{2.7}$$

This is used to take into account the differences in dose rate due to the activity distribution in the source, and photon attenuation in the source itself and its encapsulation. Along the transverse plane of the source, the anisotropy factor is defined as 1.

Summary of the TG-43U1 protocol

The TG-43U1 protocol is currently the worldwide standard for photon-emiting brachytherapy dose calculations, and is widely adopted for HDR brachytherapy ^{192}Ir dose planning. This model is typically based upon Monte Carlo simulations and is strictly valid only for a homogeneous water phantom, of the size and shape used to obtain the model parameters [32]. While fast to implement within the clinic, the issues of tissue and applicator heterogeneities, and the finite patient dimensions are all ignored [33].

This has led to the development of model-based dose-calculation algorithms (MBDCAs) where radiation transport could be modelled in non-water mediums, realising more physically accurate determinations of the dose delivered to the patient. A description of guidelines for MBDCAs is found in the AAPM Report of the Task Group 186 [32]. Throughout this thesis, the use of the TG-43U1 protocol for dose calculations has been considered, from the TPS and based upon measurements of source position. The TG-43 parameters for the Nucletron microSelectron® mHDR-v.2. source and Nucletron Flexitron® HDR Flexisource were obtained from Taylor and Rogers [28].

2.6 The need for quality assurance in HDR brachytherapy

HDR brachytherapy involves minimal fractionations, short treatment times and large doses administered within seconds. It is therefore essential that treatments are delivered with high accuracy, as errors could result in severe complications [5, 34]. While HDR brachytherapy is generally regarded as a safe treatment modality, there have been many events recorded that have led to patient mistreatments. More than 500 HDR accidents, including one death, have been reported along the entire chain of procedures from source packing to delivery of dose [5].

The majority of these mistreatments were due to human errors, such as the inaccurate entry of source strength and prescription dose into the treatment planning and afterloader console, and improper catheter selection. Other common errors were the use of wrong step sizes in the treatment planning or the afterloader control program, wrong transfer tubes connected to the remote afterloader, and the incorrect lengths of tubes and catheter [8]. While the likelihood of the remote afterloader malfunctioning and incorrectly administering the treatment is considered low, deviations from the plan in dwell positions and times can result in variations in delivered dose. It has been shown that the use of multiple interstitial catheter applicators, such as in prostate treatments, would have the highest susceptibility to these deviations [9].

As HDR brachytherapy planning becomes increasingly complex, it is important to develop treatment delivery verification methods to ensure optimum treatment of patients [15]. One of the fundamental goals of an effective quality assurance program for HDR brachytherapy is to ensure that treatments are consistently administered

correctly by the remote afterloader, as the success of the treatment is dependent on positional and timing accuracy [13, 14].

As recommended by the AAPM Radiation Therapy Task Group No.59, institutions should make the minimisation of the likelihood of treatment errors a high priority in the HDR working environment and procedure flow [10]. A quality assurance program should exploit redundancy, and review the entire proposed delivery process to isolate any actions vulnerable to errors. The incidence of these errors could be reduced by the introduction of additional pretreatment quality assurance checks between the treatment planning and delivery process.

An accurate treatment delivery means that the source is driven to the planned position, in the correct applicator, for the correct amount of time, ensuring the calculated absorbed dose matches the prescription set by the radiation oncologist [11,12]. An ideal system for HDR brachytherapy treatment verification should be able to provide the real-time identification of the dwell positions, measure the dwell and transit times, and compare these parameters with the prescribed treatment plan both before and during treatment. The AAPM ratified that to guarantee a "good" quality assurance program, the medical physicist should be able to accurately measure the source position, timing, transit velocity and the delivered dose distribution [11]. A sound QA program will thus ensure the correct operational procedure and will reveal and prevent possible mistakes, allowing for the safe execution of a treatment in regards to patients and staff.

2.7 Current methods of quality assurance

While there are guidelines detailing the quality assurance process for the entire HDR brachytherapy procedure work flow and safety systems [10, 35, 36], there is an absence of a comprehensive treatment delivery verification system within the clinical environment. Delivery verification of the source position and dwell timer accuracy of the HDR afterloader is typically performed in the clinical environment using rudimentary devices.

Source position accuracy

The verification of the positional accuracy requires that the planned sequence of dwell positions is delivered to the correct position in the correct applicator [11]. According to the Australasian College of Physical Scientists and Engineers in Medicine (ACPSEM) recommendations [35], the source positional accuracy test must be performed daily. This can be carried out by exposing the source position onto radiographic film with markings or with a specialised source position check ruler, seen in Figure 2.6. The source position can be verified by focussing the treatment suite camera on the source position check ruler during a QA run. For most QA protocols the typical tolerance range is 1 mm, where action is to be taken when the inaccuracy is larger than 2 mm. This accuracy has been found to be affected by curved applicators and transfer tubes [37, 38].

Figure 2.6: The source position check ruler.

Dwell time accuracy

A treatment delivery system achieves temporal accuracy if each planned dwell time remains at its intended position for the length of time specified by the treatment plan [11]. The remote afterloader has an electronic timer that is typically verified using a stopwatch, and performed in combination with the source position catheter ruler test. For most QA protocols the typical tolerance range is 1%, where action is to be taken when the inaccuracy is larger than 2%. The influence of the source transit time is recommended to be taken into account when performing the dwell time accuracy, as some afterloaders reduce the actual dwell time of the source to compensate for this. Another potential issue is the "rounding error" that is introduced when exporting the treatment plan to the afterloader control unit, and even dwell times less than 0.1 s can be rounded down to 0.

2.8 Pretreatment and *in-vivo* verification

In the literature there are several studies that investigate different HDR brachytherapy quality assurance approaches. The goal of the majority of these studies was to develop a method of localising the source dwell positions and measure timing patterns. The following review is arranged chronologically, except when discussing a series of related investigations.

Early pretreatment verification of the source position was performed by Evans et al. [39]. The method presented was to irradiate film using the HDR source and to superimpose an x-ray image of dummy cable markers. A HDR treatment catheter was attached to x-ray film using tape and the afterloader was programmed to dwell

the source across the catheter with equal dwell times and a 20 mm step size. The catheter was then detached from the afterloader, and a dummy cable was inserted into the catheter, still attached to the film. This dummy cable had markers at 10 mm intervals, which when imaged by a diagnostic x-ray, were used to verify the spacing and relative position of the HDR source.

The feasibility of treatment monitoring using x-ray fluoroscopy and an anti-scatter grid was investigated by Sheikh-Bagheri and Munro [40]. EGS4 Monte Carlo was used to simulate the interactions of the ^{192}Ir and diagnostic x-rays photons inside a phantom, anti-scatter grid and fluoroscopy detector. They concluded that, in principle, this method could be used to monitor the delivery of the HDR source, but was considered difficult to implement in the clinical environment due to constraints on the physical size of the equipment needed.

A real-time in-treatment source position monitoring system using pinhole imaging was investigated by Duan et al. [41]. The technique, typically used in nuclear medicine, coupled a pinhole collimator with a radiographic screen-film and x-ray fluoroscope. The system used a dual-pinhole placed away from the phantom and reconstructed the dwell positions in three dimensions using a triangulation algorithm. The authors reported an average difference of 0.72 $\pm$ 0.05 mm between the reconstructed and planned positions. The fluoroscopy machine allowed for recording of the measurement of the image onto a standard VCR video-tape for post-treatment verification. While able to reconstruct the source position in post-processing of film, this method relied on the user to notice any significant deviations in position via the fluoroscope screen during actual treatment.

Nakano et al. [42] proposed a proof of principle using a minimum of three detectors

for HDR three-dimensional source localisation during treatment. Commercial diamond detectors were investigated for their use in HDR by measuring their directional and temperature dependence and characterising their response over varying distances from the HDR source. The intended method was expected to localise the source position with an accuracy of better than 2 mm over a source to detector distance of 1 to 12 cm.

This method was experimentally validated shortly after by Nakano et al. [43] by placing a single diamond detector at 12 positions on an anthropomorphic phantom that was irradiated by a single HDR catheter. The source position was calculated by an iterative method based upon a least square fit, which took into account detector responses compromised by tissue inhomogeneity. As the accuracy of the localisation was highly dependent on the knowledge of the catheter and detector positions on the phantom, it was necessary to perform a CT scan to provide a frame of reference to the system. The author remarks that measurements of dwell time could be feasible, depending upon the measurement sampling frequency of the system used.

A method was proposed by Liu et al. [44] to use a mobile C-arm fluoroscopy machine to image the check cable at the final dwell positions, prior to treating the patient. Verifying by visual inspection, the authors remarked that the method is useful for observing gross errors in dwell positions larger than 1 cm. This method images only the check cable position at final dwell positions, giving no information about the actual source positions during treatment.

A pretreatment check of the HDR source using film and a multi-slit phantom was proposed by Kohr and Siebert [45]. By placing the HDR implant tubes directly on top of the multi-slit phantom, dwell positions were determined to an accuracy of 0.45

mm.

Three types of film were evaluated to determine the dwell position accuracy of the HDR afterloader by Evans et al. [23]. The method used was to create a co-registered image of the source autoradiograph, superimposed with a diagnostic x-ray of dummy sources within the same applicator.

The idea of using of a flat panel detector for tracking the HDR source was described by Song et al. [46]. The flat panel was coupled with an array of ball bearings, and used their individual shadows to determine the source coordinates. The device was capable of determining the position of the source with a mean difference of 0.7 mm with a standard deviation of 1.5 mm. By using new devices with faster image acquisition, and the development of an automated ball bearing shadow recognition software, source tracking could be possible using this proof of concept.

Lambert was one of the first to investigate the use of plastic scintillator detectors (PSD) coupled to optical fibres in HDR treatment verification [47]. The PSD system was characterised in terms of depth dose response, angular and energy dependence and the generation of Cerenkov and fibre fluorescence. The device tested was found to be feasible for real time treatment verification and could be easily inserted into urinary catheters.

The use of PSD for HDR pretreatment verification was tested by Kojima [48]. A single HDR catheter was inserted into a hole centred inside of a $50\times50\times150$ mm^3 block of organic plastic scintillator. The scintillation luminescence was digitally recorded using a charge-coupled device camera system at a rate of 30 frames per second and with high image resolution. The source position was determined from the image scintillation

brightness distributions, with a precision of less than ± 1 mm. Source dwell and transit times could also be determined with a timing resolution of 1/30 s.

Anderson et al. explored the use of carbon-doped aluminium oxide (Al_2O_3:C) crystals for luminescence dosimetry in the application of in-body HDR brachytherapy verification [49]. The highly sensitive crystal enabled a compact packaging design, that when coupled to optical fibres, could be made to fit inside of standard brachytherapy applicators. The Al_2O_3:C crystal produced radioluminescent light spontaneously under irradiation and could be used for real time dose rate monitoring. Also, by optically stimulating the Al_2O_3:C crystal using a 532 nm 20 mW green laser, the accumulated dose for the full treatment could be obtained while still inside the patient.

Batič et al. expanded the idea of pinhole imaging, using silicon pixelated pad detectors instead of film [50]. Two catheters were fixed in a support structure with the detection system at a fixed distance away in air. It offered the ability to reconstruct the source position with a precision of about 5 mm from a source-to-pinhole distance in air of 40 cm. However, this precision is comparable to the distance between two dwelling positions of the HDR source during treatment and was expected to arise from the inaccurate alignment of the detectors with the pinholes. Although the readout of these detectors allowed for reconstruction of source position in 1 s, giving the possibility of tracking, there was no indication if the detection system was capable of measuring the dwell time patterns of the source.

Rickey et al. [14] developed a quality check tool for HDR brachytherapy by combining the use of radiochromic film and photodiodes and determining the dwell positions and times in a fixed treatment tube. Readout of the four photodiode's response occurred with a timing resolution of 1 ms. Dwell position were reconstructed with an accuracy of

0.5 mm by manual optical inspection and down to 0.2 mm by a digital post-processing of the film. The authors state that this method allowed for the verification of the position and dwell times of a single catheter in about 6 minutes.

PSD for *in-vivo* dosimetry and real-time monitoring of HDR treatments was investigated by Therriault-Proulx et al. [51] and verified in a water phantom. Eleven catheters were used for delivery of the HDR source, and an additional two were used to house the PSD to mimic dosimetry at the rectum wall and inside the urethra. The measured doses and dose rates were compared to the values expected from the treatment planning system and were able to determine position offsets of 5 mm. The hardware limited the measurement to a maximum frequency of 10 Hz, and only dose rates for dwell times greater than 5 s could be analysed.

The investigation into the use of Al_2O_3:C crystals for HDR *in-vivo* dosimetry was continued by Kertzscher et al. [52]. By developing a statistical error criterion based upon the agreement of the integral dose continuously measured and that simulated by the treatment plan, source displacement errors of 5 mm and greater could be detected. It was found that the statistical confidence in the comparisons between measured and planned dose rates was dependent on the accuracy of the determined dosimeter position.

Kertzscher et al. later addressed this shortcoming with a newer error adaptive detection algorithm that did not depend on an absolute prior detector position reconstruction [53]. The method compared dose rates for individual dwell positions measured by the dosimeter with that simulated for multiple dosimeter positions. When a significant difference was found between the measured dose rate and that simulated for a single dosimeter position, the dose rates from the other simulated positions would be com-

pared. If agreement was found with a new dosimeter position, then this was updated for further use; if the disagreement was significant then the algorithm deems that a treatment error was detected. This method was found to increase the sensitivity to treatment errors, and could potentially be adapted to multiple dosimeters for increased redundancy.

The use of commercial ion chamber arrays, designed for external beam radiotherapy, was investigated by Manikandan et al. [54] for HDR source position verification by placing the catheters directly on top of the device. The I'matriXX (IBA Dosimetry GmbH, Germany) verified treatment dwell positions with a maximum error of 1.8 mm for step sizes larger than 2 cm. It found that due to the large width of each ion chamber of approximately 5.8 mm, the device displayed a volume averaging effect and step sizes below 1 cm could not be resolved.

A novel in-body silicon pixellated detector was proposed for HDR brachytherapy by Safavi-Naeini et al. [55] and for low dose rate (LDR) brachytherapy by Petasecca et al. [56]. The concept device, named BrachyView, used the high spatial resolution Medipix2 detector [57] coupled to a multi-pinhole tungsten collimator designed to be inserted into the rectum, replacing the TRUS probe at the time of treatment. Both applications used the images projected through each pinhole onto the detector to determine source position, and for HDR treatments was shown to not cause dose enhancement to the patient [58]. Monte Carlo simulations of the HDR ^{192}Ir source and various BrachyView collimator designs reported by Safavi-Naeini showed that the maximum error in localisation would be 1.5 mm. Experimental verification of this proof of concept has been researched and has been accepted for publication [59].

The use of an electric portal imaging device (EPID) for in-treatment monitoring was

proposed by Smith et al. [60]. The source position was determined in three dimensions from analysis of the shape of the measured radiation distribution and absolute response. The system was able to determine the source x and y coordinates with an accuracy of 0.5 mm for source to detector distance of up to 150 mm. The determination of the source to detector distance was found to be a approximately ± 0.1 mm at 50 mm distance, and up to ± 2 mm at 150 mm.

Wang et al. and Pittet et al. proposed the use of GaN scintillating probes for in phantom pretreatment verification [38, 61]. The position of the HDR source inside a single catheter was determined from the comparison of the measured response of two probes and TG-43 dose rate calculations. The differences between the measured and planned positions were found to be lower than 1 mm, with dwell time differences found to be within 0.1 s, the same as the temporal resolution of the acquisition system used.

Jursinic devised a way to perform pretreatment quality assurance using a single p-type semiconductor diode readout with an electrometer [62]. The diode was fixed into Styrofoam, close to the boundary of a 6 mm Plexiglas slab. A single straight catheter and ring applicator were tested by placing them on top of the Plexiglas, aligning the catheter over the diode and the ring centred at the diode. The source position was determined with an accuracy equal to or less than ± 0.3 mm for the ring applicator and straight catheter. Checks of the temporal accuracy of the HDR afterloader were performed and found to have an accuracy of 0.3% using this device.

Two commercial devices have been developed by Mick Radio-Nuclear Instruments for HDR QA. The PermaDoc GC Phantom allows for the insertion of a single HDR catheter into the device, where the source exposes its position, as well as centimetre markers, onto gafchromic film. This solution verifies one catheter at a time and

would require digital post processing to determine an accurate position. The MultiDoc Phantom, developed by Mick Radio-Nuclear Instruments, allows for up to 21 catheters inserted into a phantom, where the source can be seen through the catheter, above the phantom. Next to each catheter insert are positional markings in 1 mm increments, and the source dwelling and timing is captured by a high resolution video camera above the phantom. While capable of source position and timing of up to 21 catheters, the system relies heavily on the user to perform verification by watching and analysing the video recording.

2.9 Measurements of the HDR source transit time

Transit dose is defined as the additional dose delivered while the source is in transit, as seen in Figure 2.7. Currently, only the dwelling components of the treatment plan are used to calculate the total dose by the treatment planning software. However, as the HDR afterloader moves the source at a finite speed and the ^{192}Ir source is continuously decaying, there is a dose delivered to the patient not taken into account by the TPS. Direct measurements performed by Bastin et al. using thermoluminescence dosimetry showed that the transit dose could exceed a few hundred cGy for some treatment scenarios [63]. By not factoring in this additional dose when using high activity sources and short dwell times, significant error can be introduced in dose calculations.

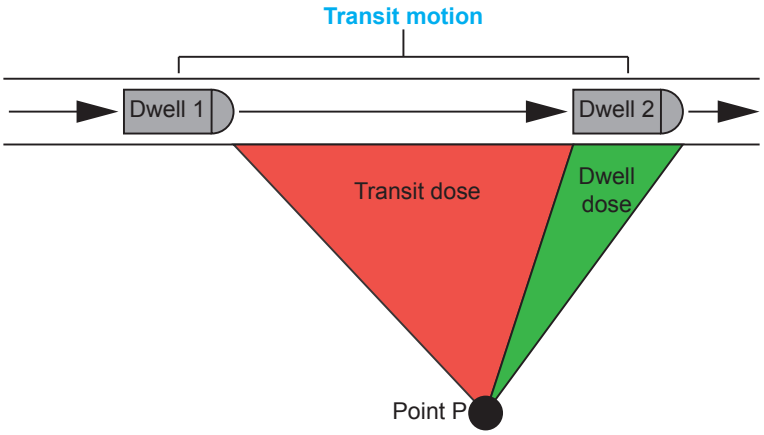

Figure 2.7: The transit motion and dose delivered to an arbitrary point P.

In the literature, methods of calculating the transit dose is generally based upon a determination of the average source speed during transit, or by assuming a constant acceleration phase, a constant maximum speed and a constant deceleration. Nucletron, the manufacturer of the tested afterloaders, claims that the maximum speed of the source is 50 cm/s, and uses this value to perform compensations during delivery. The average source speeds reported in the literature vary substantially, and a summary can be found in Table 2.2.

Interdwell	Average source speed (cm/s)					
distance (mm)	[a]Bastin	[b]Houdek	[c]Sahoo	[d]Wong	[e]Fonseca	[f]Espinoza
2.5	23	22.7	—	5.4 ± 2.3	32.8 ± 2.7	12.8 ± 0.3
5	25.5	27.1	33.3 ± 11	7.2 ± 1.6	45.8 ± 2.6	17.5 ± 0.3
10	—	30.3	50 ± 50	23.3 ± 7.3	34.9 ± 0.9	24.7 ± 0.3
20	—	32.3	80 ± 32	—	—	31.8 ± 1
30	—	32.7	60 ± 30	—	—	33.3 ± 0.9
50	—	33.1	43.5 ± 11.3	—	32 ± 0.2	38.6 ± 0.4

Table 2.2: Summary of the average source speeds based upon measured transit times reported in the literature for varied interdwell distances. All values were obtained using a Nucletron afterloader (Nucletron, an Elekta company, Elekta AB, Stockholm, Sweden). Not all uncertainties were reported. [a]Bastin et al. [63], [b]Houdek et al. [64], [c]Sahoo [65], [d]Wong et al. [66], [e]Fonseca et al. [67] and [f]Espinoza et al. [16].

Houdek el al developed a mathematical formalisation of the dose received at a point by the source in transit [64]. An estimation of the transit time was performed using an oscilloscope to measure the pulse generator of the stepping motor of the afterloader. Although the transit dose component was not measured, calculations were performed to determine the effect of the transit dose on a plan using the measured source speeds.

Measurements of the transit times were performed by Sahoo [65] using an ionisation chamber and a precision electrometer to measure the charge generated during the movement of the HDR source. The average source speed was determined over a range of step sizes, from 5 mm to 100 mm. However, due to the error in charge measurement, time error in the afterloader and the transit time correction by the afterloader, up to 100% uncertainty was recorded for some average speeds.

Wong et al. used a video camera to film the movement of the source in a flexible

transparent catheter placed next to digital stopwatch with a timing resolution of 0.01 s [66]. A maximum average transit speed was determined to be 52.9 ± 1.5 cm/s for the travelled distance of 99.5 cm, however, by assuming a constant acceleration and deceleration phase at one-fifteenth the distance for each, the average source speed was computed to be 46.7 cm/s.

Using an optical fibre system to detect the radiation generated by the moving HDR source, Minamisawa et al. were able to calculate the instantaneous and average source speed [68]. By placing two optical fibres at set distances apart, and close to the HDR catheter, the Cerenkov light induced by the moving HDR source was used to assess the transit time across that distance. The optical fibres were connected to a photomultiplier tube that converted the light to an electrical signal and was directly measured by an oscilloscope. By fixing the optical fibres spacing to 1 cm, the deceleration profile of the HDR source was determined, as well as the average speeds over various interdwell distances. The authors concluded that the source undergoes constant acceleration and deceleration, of approximately 113 cm/s^2.

The transit dose of an HDR unit was quantified by Fonseca et al. [69], based upon calculations of the instantaneous source speed and a Monte Carlo (MCNP5) simulated transit dose profile. The instantaneous source speed, measured by the optical fibre based system reported by Minamisawa et al. [68], was used to give weighting to the simulated transit dose and allow for an accurate calculation of transit dose values. The results were verified experimentally using radiochromic film, and showed that the transit component can be significant, reaching up to a few hundred cGy per application. Fonseca et al. later determined the total transit dose to the patient using this method for two gynaecological and two prostate cases, each having a different number of catheters and locations [70].

Fonseca et al. then used a high speed video camera to measure the source motion through the position check ruler [67]. The video camera was able to film at 960 fps, with a verified timing resolution of 1.04 ± 0.01 ms, and the source position was analysed frame-by-frame using MATLAB 8.0 (MathWorks, Inc., Natick, MA). It was seen that source motion was changing speed periodically, as it moved from dwell position to dwell position. The author concluded that the accelerating and decelerating were unable to be seen in the aforementioned studies due to the timing resolutions used.

The average source speed was investigated by the author as part of this research, using a single silicon diode detector and fast electrometer [16]. The sensor was readout by a single channel fast electrometer named X-Tream, which is designed as a dosimetry system for microbeam radiation therapy QA [71], and is characterised by its high dynamic range ($\sim 10^5$) and high sampling rate (1 MHz). Using high timing resolution of the system, the transit time was analysed by considering the time needed for the source response to become constant after stepping. Information about the source position was not known as the system used only one detector.

2.10 Silicon detectors for quality assurance

Silicon detectors have been predominantly used for nuclear spectroscopy since the 1960s and, with the development of manufacturing technology, have found application in the dosimetry of clinical radiation treatments [72–74]. Silicon has characteristics that are very attractive for use as a dosimeter, as they can be used to measure dose or dose rate in real time, as a substitute to ionisation chambers.

The average energy for creating an electron-hole pair in silicon is 3.6 eV, approxi-

mately 10 times smaller than that for gases used in ionisation chambers. Coupled with a higher density of 2.33 g/cm^3, the result is a radiation sensitivity approximately 18,000 times higher than an ionisation chamber of the same volume. As a result, the measurement volume of the detector can be small and well defined, leading to a good spatial resolution [75, 76]. Silicon detectors have other favourable features such as the ability to operate at room temperature, are mechanically stable and need a low or no bias voltage.

However, there are two main limitations when considering silicon as a material for radiation detectors. Due to the increased interaction cross section of the photoelectric effect in silicon relative to water in the keV energy range, illustrated in Figure 2.8 a), silicon exhibits a greater sensitivity to low energy photons, which must be taken into account when performing dosimetry in this energy range.

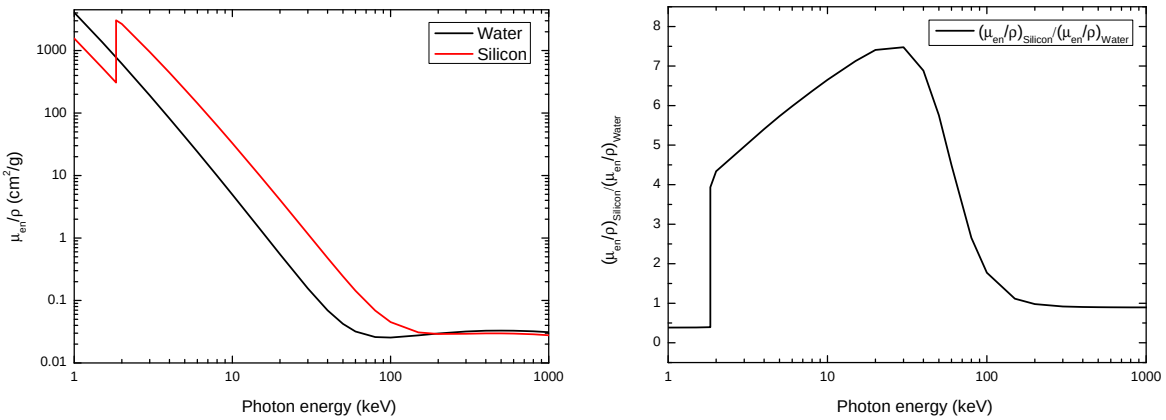

(a) μ_{en}/ρ for Water and Silicon

(b) μ_{en}/ρ ratio for Water and Silicon

Figure 2.8: Comparison of μ_{en}/ρ for Water and Silicon. Data obtain from NIST database [77].

Figure 2.8 b) shows the ratio of the mass energy-absorption coefficients, μ_{en}/ρ, of silicon to water over the range of 1 - 600 keV, with the data obtained from the U.S. National Institute of Standards and Technology (NIST) database of x-ray mass at-

tenuation coefficients [77]. The mass energy-absorption coefficients is an important quantity for the determination of energy deposition by photons, and the ratio can be used to calculate dose in different mediums. It is important to note that between the 1 - 100 keV photon energy range, there is an approximately 7.5× increase in sensitivity, and that over energy ranges of 150 keV, the difference is less pronounced and silicon is said to be water equivalent. This over sensitivity of a silicon detector can be mitigated by the choice of application in specific photon energy ranges, by the packing of the detector and by the use of low energy photon shielding materials.

The second limitation is that damage to the detector that occurs when dose is accumulated by the detector, resulting in a decreased sensitivity, increased noise and a decrease in the carrier mobility and its lifetime [78]. The radiation damage is known to increase the current when the diode is reverse biased, known as the *leakage current*, and is due to radiation induced defects within the bulk silicon and the silicon oxide interfaces. By operating the detector in *passive mode*, this leakage current can be reduced, and the reduction in sensitivity can be mitigated by detector design [79].

Silicon diode detector theory

The physics of the p-n semiconductors is fundamental to the use of a silicon diode as a radiation detector [80]. P-type and n-type semiconductors are created by the controlled addition of impurities from either group III or group V elements to high purity semiconductor crystals, known as intrinsic semiconductors, in a process known as doping. N-type silicon is made by introducing a donor atom into a crystal, usually phosphorus or arsenic, while an acceptor atom is introduced, such as boron, to obtain p-type silicon. For n-type silicon, the majority carriers are electrons and the minority carriers are holes, while for p-type, the majority are holes and the minority

are electrons. The energy level structures for the intrinsic, p-type and n-type silicon are shown in Figure 2.9.

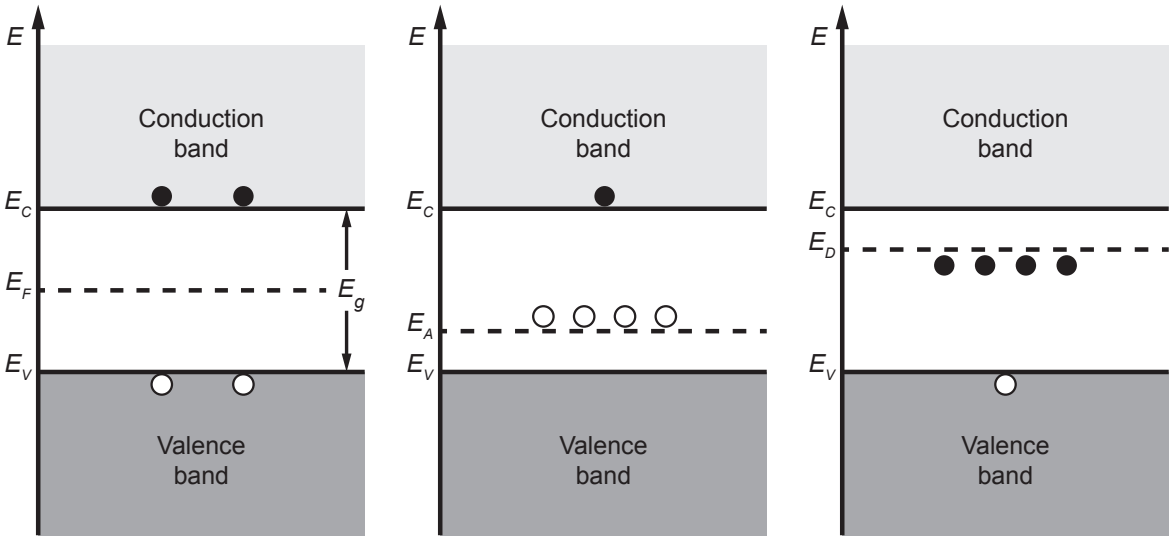

(a) intrinsic (b) p-type (c) n-type

Figure 2.9: The electron energy band diagram for a) intrinsic, b) p-type and c) n-type silicon. Electrons and holes are displayed as black and white circles, respectively.

In each of the three illustrations, the valence and conduction bands can be seen, with their respective energies, E_v and E_c. The valence band represents the electrons bound to the highest energy orbitals of the atoms in the crystal, while the conduction band represents the possible energy states of electrons that are free to migrate throughout the crystal and contribute to electrical conduction. Electrons that are excited thermally or otherwise can overcome the energy gap between the valence and conduction bands, E_g, leaving a hole in the valence band. The Fermi level, E_F, is between the valence and conduction bands for the intrinsic semiconductor, and is the top electron energy state for the collection of energy levels at absolute zero temperature.

Acceptor atoms have one less electron in the outer shell and changes the energy level of p-type silicon by introducing acceptor states, E_A, which shifts the Fermi level closer

to the valence band. This allows for extra holes to be in the acceptor states that can be filled by excited electrons from the valence band, leaving mobile holes, which adds to electrical conduction. Conversely, donor atoms have one additional electron in the outer shell and changes the energy level structure of n-type silicon by introducing donor states, E_D, which shifts the Fermi level closer to the conduction band. These extra electrons fill the donor states, and can be easily excited into the conduction band. By combining the p-type and n-type semiconductor materials, semiconductor devices can be created. The most basic combination of these materials is the p-n diode.

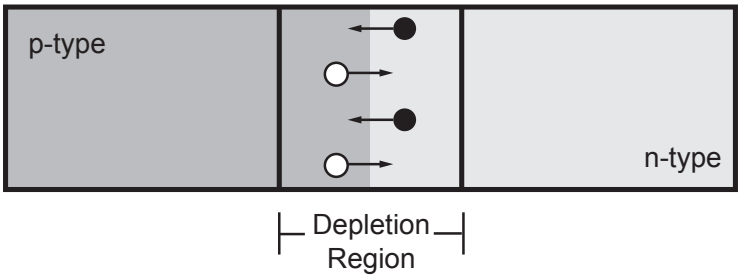

Figure 2.10: The movement of electrons and holes to form the p-n junction depletion region.

The p-n junction is defined as the boundary between the p-type and n-type semiconductor material. At the junction boundary, there exists a region that is almost free of movable charge carriers, known as the *depletion region*. This is formed by the diffusion of electrons from the n-type towards the p-type region, leaving positively charged ions at the n-type material, and the movement of holes from the p-type to the n-type, leaving negatively charged ions, seen in Figure 2.10. The separation of positively and negatively charged ions generates a strong electric field across the depletion region, and prevents the further diffusion of electrons and holes.

When an ionising particle passes through the diode, energy is deposited through the creation of electron-hole pairs along the particle's path, seen in Figure 2.11. If the

particle track is through the p-n junction, the electron-hole pairs are separated and swept by the electric field in the depletion region. The electrons are accelerated towards the n-type junction of the detector, while the holes move towards the p-type.

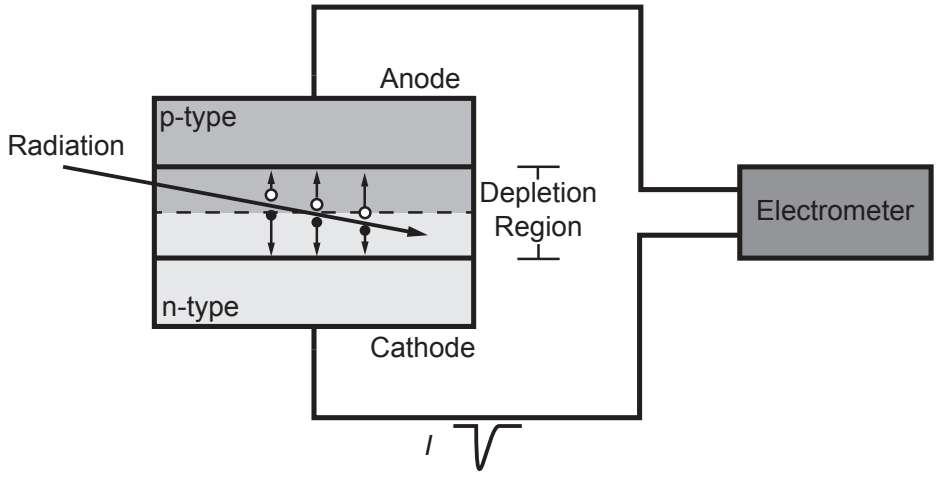

Figure 2.11: Electron-hole pairs created along a radiation particle track inside of a p-n diode.

The two main modes for the operation of radiation detectors are *pulse mode* and *current mode* [72]. Pulse mode operation, also known as *spectroscopy* mode, is when the radiation detector system is designed to record each individual quantum of radiation that interacts with the detector. When considering high event rates, like in HDR brachytherapy, it could be impractical to operate the detector in this mode, as individual radiation interactions may not be distinguished. By designing the readout electronics for use in current mode, the average current induced over many radiation interactions can be recorded and used to determine the dose rate. The resulting radiation induced current can be measured by an electrometer, where the current and the total charge are proportional to the dose rate and total absorbed dose in silicon, respectively.

2.11 Conclusion

Prostate cancer has one of the highest occurrence rates for males in Australia, with a projected 25,000 cases being diagnosed each year by 2020. High dose rate brachytherapy, typically used in combination with other methods, is one of the more common options to treat this disease. The short treatment involves remotely controlling the temporary placement of the small, highly active radiation source directly into the tumour, until the large prescribed dose distribution is achieved.

Accurate treatment delivery relies on the exact execution of the patient plan. This means that the remote afterloader should move the HDR source with high precision in its positioning and timing.

Whilst methods are being developed to verify the quality of a treatment delivery, they can use bulky and expensive equipment, and not provide a complete picture of the delivery. There is currently no comprehensive method to verify the afterloader delivery of the plan, both pretreatment and *in-vivo*.

Silicon detector technology has the potential to fill this gap in verification systems. Due to its desirable qualities, such as the ability to perform measurements in real-time, its high temporal response and strong radiation response, they have been selected to be used for the development of a quality assurance system in this work.

Chapter 3

Description of the proposed instrumentation

The previous chapter reviewed the current technology used in high dose rate brachytherapy reported in the literature, and concluded with silicon diode detectors being a very attractive candidate for the development of a HDR brachytherapy quality assurance system. This chapter goes on to describe the technology proposed for the verification of treatment delivery, describing from the single detector element to the array of elements, the prototype phantom design, electronics system and graphical user interface that has been designed and implemented.

3.1 The "Magic Plate"

The Centre for Medical Radiation Physics (CMRP) at the University of Wollongong has designed a two-dimensional (2D) detector array, named "Magic Plate" (MP) [81]. It features 121 p-type silicon epitaxial diodes embedded in a 0.6 mm Kapton carrier in an 11×11 array, Figure 3.1. Each epitaxial diode has been connected to the MP

flexible carrier, which consists of a thin polyamide supporting substrate with a thin, chemically deposited aluminium layer tab bonded to the detector's pads and to the kapton carrier's copper tracks [82].

The MP uses two SCSI-2 connectors, with 68 channels each connector, to interface with the readout electronics. This makes the MP modular, and can be it interchanged with different versions of the front-end data acquisition systems. To minimise current generated in the detector and the kapton carrier's tracks, the entire MP was covered with 70 μm of aluminium tape, which was then connected via wire to the AFE DAQ system electrical ground. This was done to shield the detector from interferences from external electromagnetic fields.

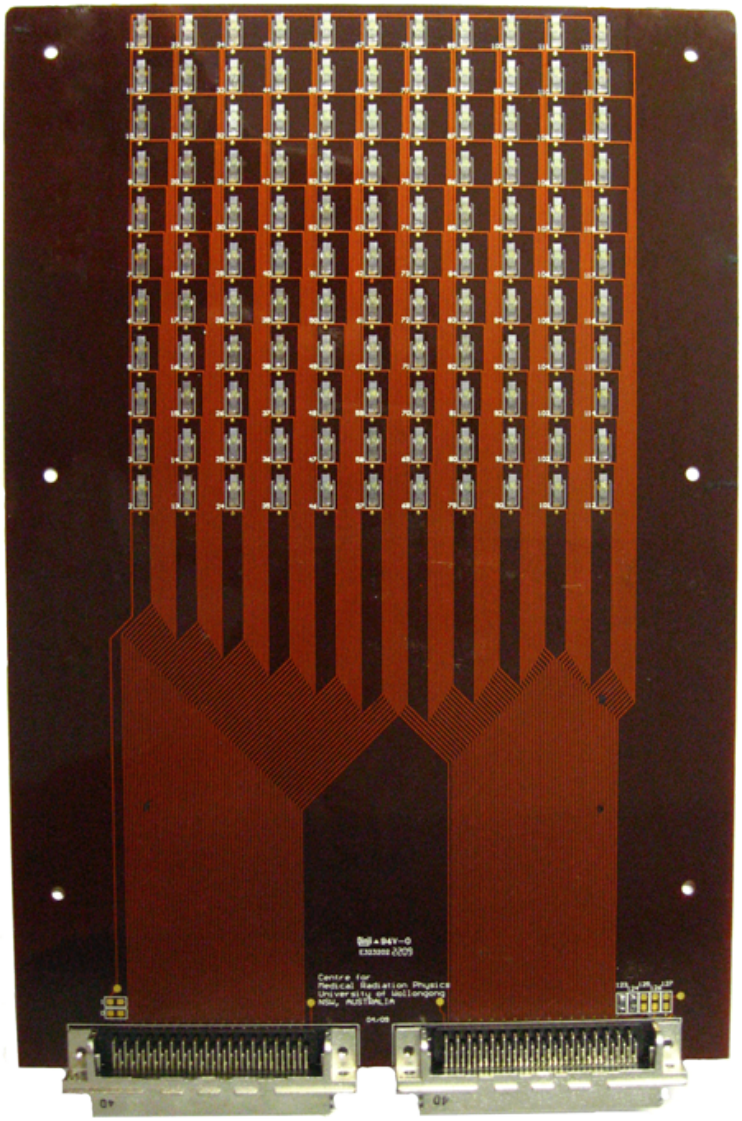

Figure 3.1: The "Magic Plate" detector.

The silicon diodes are designed and developed at the CMRP and fabricated at the foundry SPA-BIT (Ukraine). Each detector is manufactured on a 50 μm thick p-type (100 ohm·cm) silicon epitaxial layer, grown onto a 375 um thick (0.001 omh·cm) silicon substrate. The sensitive area of the diode is 0.6×0.6 mm^2 and is defined by an boron ion-implanted junction.

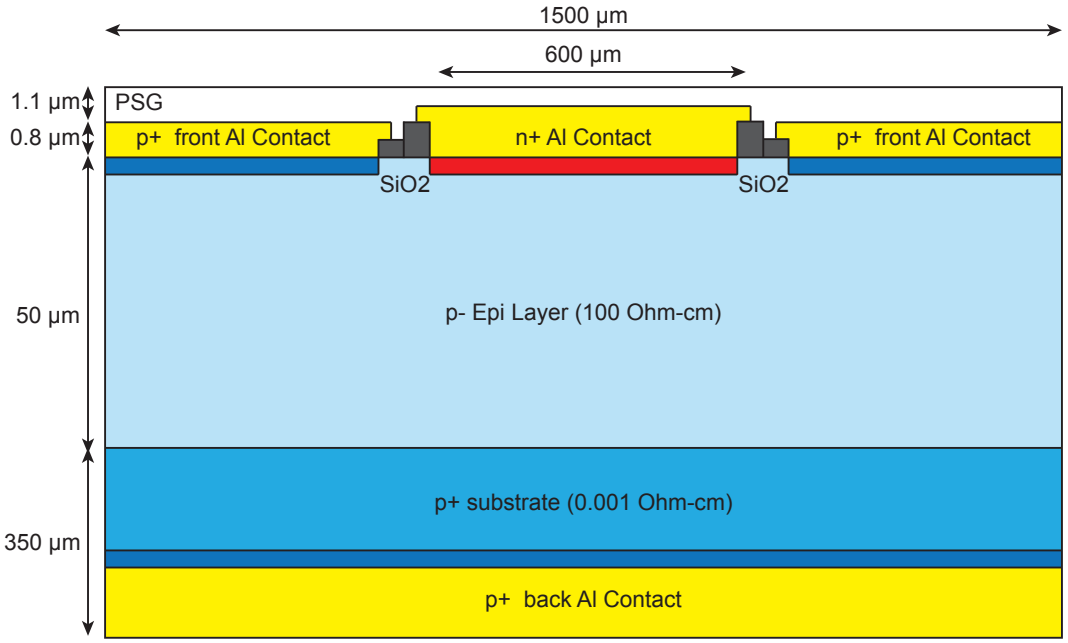

Figure 3.2: The epitaxial diode. Illustration not to scale.

By manufacturing a detector on a p-type substrate and with active region dimensions smaller than the minority carrier diffusion length, it is expected that the sensitivity will remain largely stable and independent of accumulated dose. Simulations of the epitaxial diode using Sentaurus TCAD (Synopsys, Bulgaria) have shown that the depletion layer thickness remains independent of the accumulated dose due to photon damage [83]. It was shown that there was an increase in the sensitive area of the detector with increased accumulated dose, resulting in a larger sensitivity of the detector, which plateaued at 40 kGy dose in water. To minimise the leakage current generated, each MP detector is configured to be in *passive mode*, that is 0 V bias exists between the p+ and n+ junctions.

The MP detector and electronics response was normalised to be constant across all channels when inside a uniform radiation field. This was performed using a 20×20 cm^2 photon field from a 6 MV linear accelerator (LINAC) at a source-to-surface distance

of 100 cm in a 30×30×30 cm^3 Solid Water® (SW) phantom. The MP was placed at a depth of 10 cm, where the photon field has a flat dose profile, verified regularly using ion chamber measurements as part of the LINAC's quality checks. Reproducibility of the diodes response over a period of 64 days were found to be approximately 2.1% [81].

A characterisation of the "Magic Plate" was performed to assess the energy dependence, dose rate dependence and dose linearity [81]. The energy dependence was characterised using an orthovoltage therapy machine with nominal energies of 75 – 250 kV, and 6 and 10 MV photons. It was found that the "Magic Plate" displayed a significant energy dependence, with a maximum of 7× at the lowest equivalent photon energy of approximately 31 keV when compared to the 6 MV response. It is expected that this energy dependence, coupled with the low energy ^{192}Ir spectrum, will make it extremely difficult to perform dosimetry with this system.

The dose rate response can be derived from the dose per pulse characterisation, where a range of dose per pulses were achieved by varying the source-to-surface distance, isolating the effect of the changes of the 6 MV beam spectrum on the measurement. The "Magic Plate" showed a flat dose rate response over an equivalent dose rate of 3 – 130 Gy/h, with lower dose rates not possible to be evaluated due to limitations in the sensitivity of the older generation data acquisition system used. It is expected that the "Magic Plate" should not have a dose rate dependence when used in HDR brachytherapy testing. The dose linearity was found to be linear for the measured dose range of 5 – 1000 cGy ($r^2 = 1$).

3.2 The "Magic Phantom" prototype

For pretreatment plan verification, a prototype phantom was designed to house the MP detector array and up to 20 HDR treatment plastic catheters. The prototype casing, named "Magic Phantom" (MPh), is made of Polymethylmethacrylate (PMMA) slabs. This was selected due to the availability of material and optical transparency, which assisted the of aligning the detector and catheters in the phantom. An illustration of the "Magic Phantom" is seen in Figure 3.3. Solid Water® slabs are placed both above and below the "Magic Phantom" to make a total phantom size of 30×30×30 cm^3. A characterisation of the total amount of backscatter material needed is performed in Chapter 4.

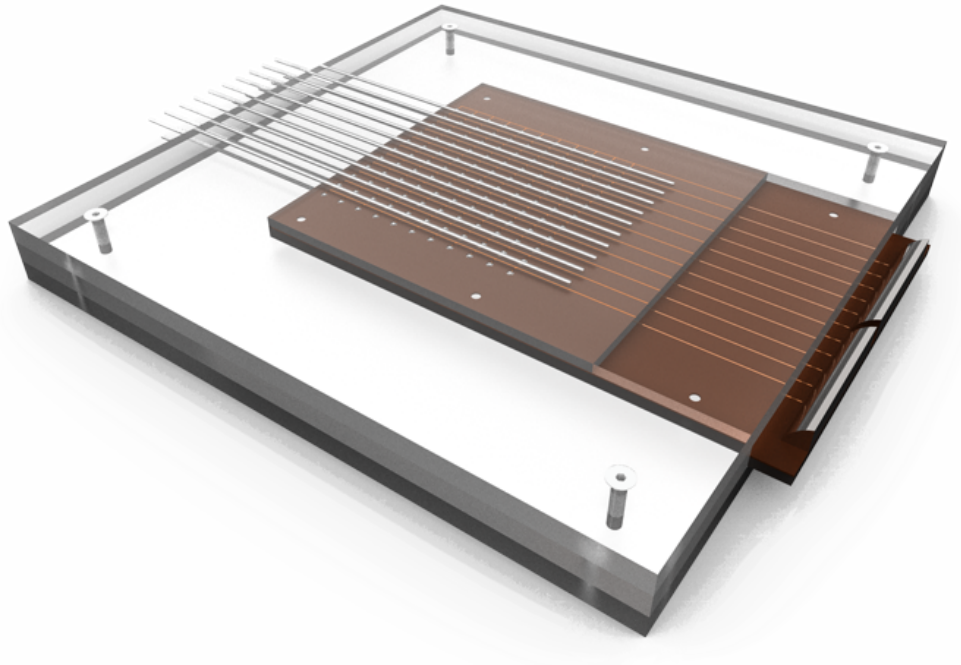

Figure 3.3: Sketch of the "Magic Plate" inside the "Magic Phantom".

The phantom is made up of three slabs of PMMA, each 30×30×1 cm^3, with the

MP 10×10 cm^2 detector field of view (FOV) positioned in the centre of the "Magic Phantom". The top and bottom layers have ten 15×2×2 mm^3 channels machined into the boundary of the centre slab to allow for the insertion of up to 20 HDR plastic catheters. These trenches are aligned so that the bottom row of catheters is positioned directly below the columns of the detector array and the above row of catheters is positioned in between the detector columns, as seen in Figure 3.4.

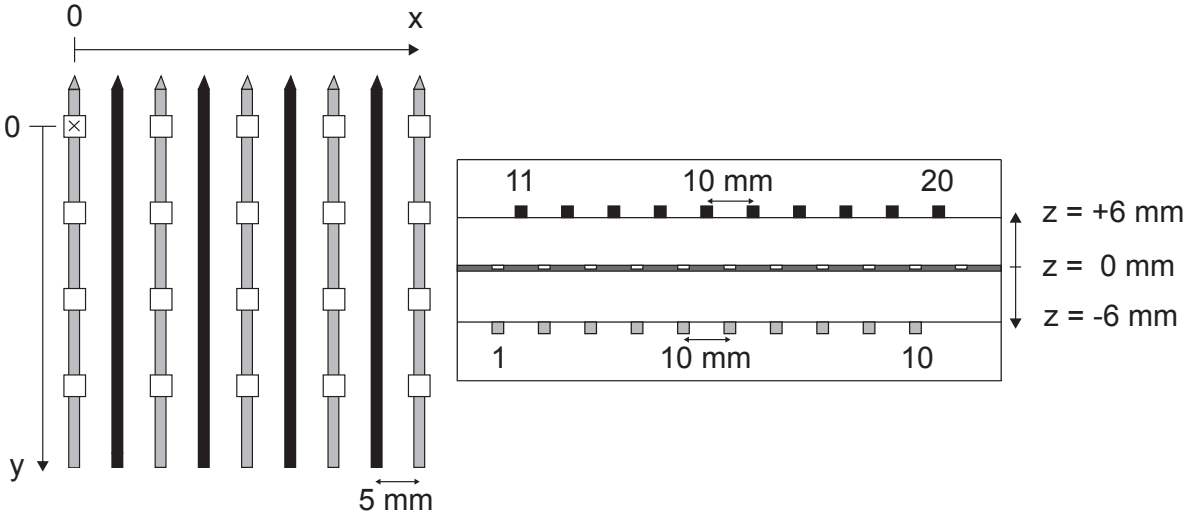

Figure 3.4: Illustration of catheter channels with respect to the "Magic Plate".

White squares represent diode positions relative to catheters, with the two rows of catheters above (black) and below (grey). The left figure shows a top view of the catheters inserted into the MPh with respect to the detectors position, and the x and y-coordinate origin on a corner detector, as indicated by a cross. The right figure shows the side view of the MPh with the catheters numbered 1 to 20. Twenty plastic 5F ProGuide Sharp catheters (Nucletron, an Elekta company, Elekta AB, Stockholm, Sweden) of equal length were inserted into the MPh and individually connected to the remote afterloader using 1 m transfer tubes, as seen in Figure 3.5.

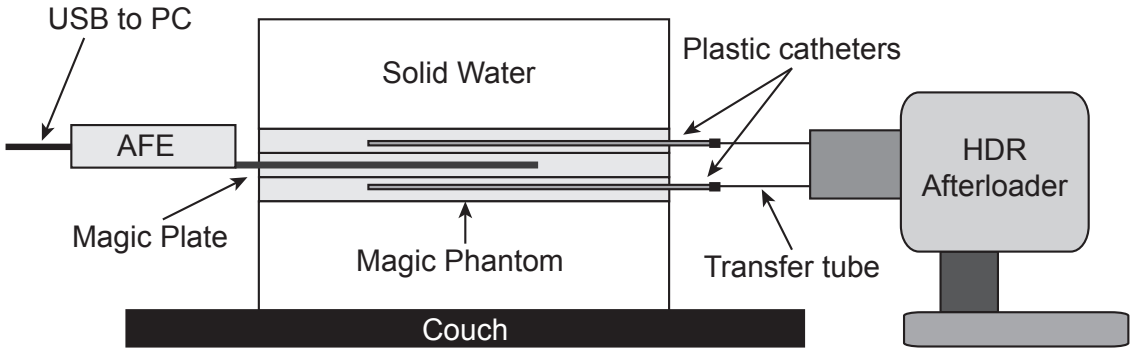

Figure 3.5: Diagram of the MPh system when used in pretreatment verification mode.

3.3 The AFE DAQ system

The analog front end (AFE) data acquisition (DAQ) system [84,85] uses the commercial electrometer AFE0064 manufactured by Texas Instruments (Texas Instruments, Dallas, United States of America). The AFE0064 was originally developed to readout flat panels for portable imaging devices, but has been adapted by the CMRP to be the electrometer for the in-house developed DAQ system. It features 64 individual integrator circuits for each channel, with a selectable global sensitivity range of charge. The charge full scale can range from 0.13 pC up to 9.6 pC in eight steps. A simplified schematic of a single channel, seen in Figure 3.6, is useful for understanding the basic principle of operation of the AFE0064 chip.

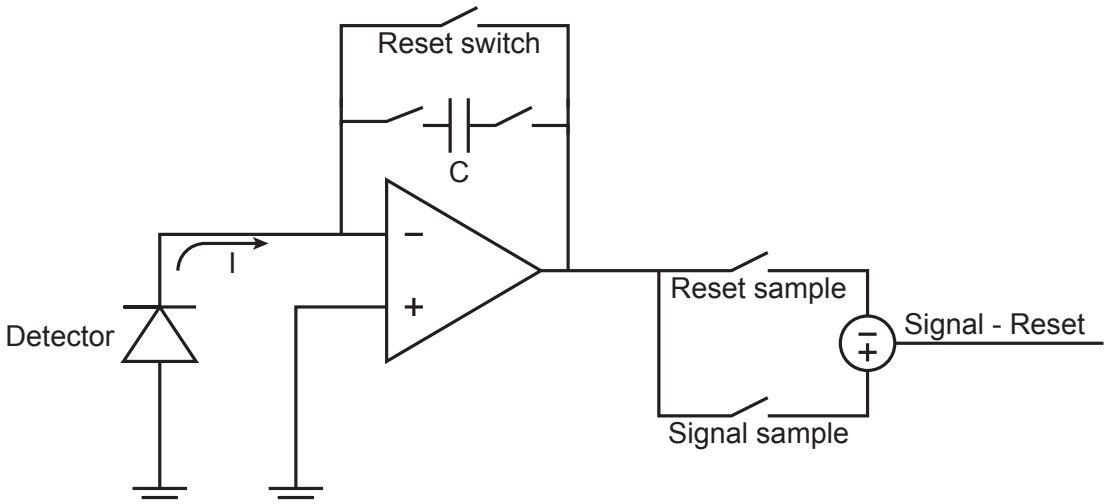

Figure 3.6: Integrator schematic for each AFE channel.

Each channel has a reset switch, which reverts the integrator output to the *reset-level*. During the acquisition phase the reset switch is opened, and the current generated from the detector, due to radiation and the leakage current, charges the capacitor on the feedback loop of the amplifier. This produces an output voltage (V) on the amplifier which is proportional to the total amount of charge collected (C) and the size of the capacitor (C), ($Q = CV$). The output voltage is measured at the end of the acquisition phase; this measurement is called the *signal sample*. The reset phase is then initiated by closing the reset switch. At the end of this phase, the output voltage is measured again; this measurement gives the *reset sample*. Once both *signal* and *reset* samples have been obtained for each channel, the difference between them is sampled by a 16 bit analogue-to-digital converter (ADC) in a differential format.

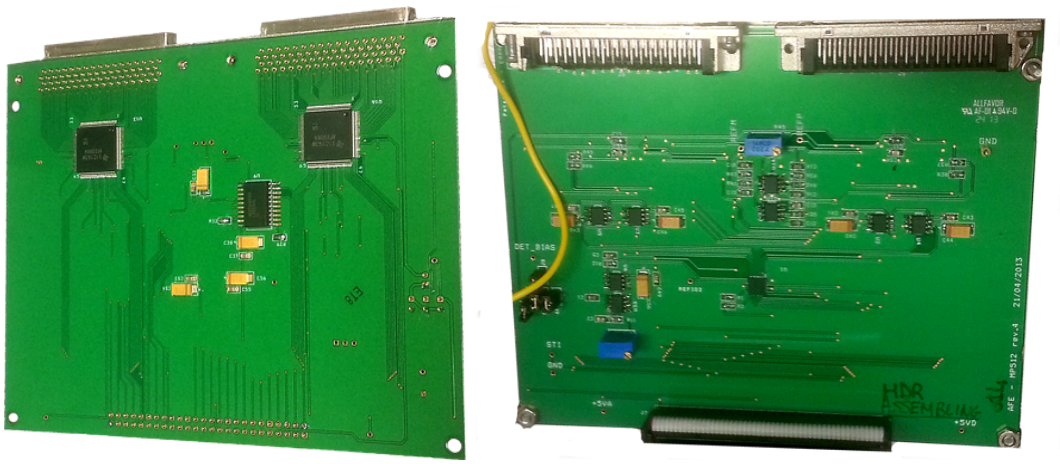

Figure 3.7: The AFE Readout chips.

The range of sensitivity of the AFE0064 is selected by the user and the differential output is set to be between ± 1.4 V, regardless of the chosen range. The output of the ADC is expressed as a percentage of the full scale of the measurable charge for that selected range. The ADC data is then digitally transferred to the Field Programmable Gate Array (FPGA) which stores the information and handles data transfer to the PC. This system has a dead time of approximately 70 μs per measurement, to allow for data-transfer and the resetting of the integration capacitors.

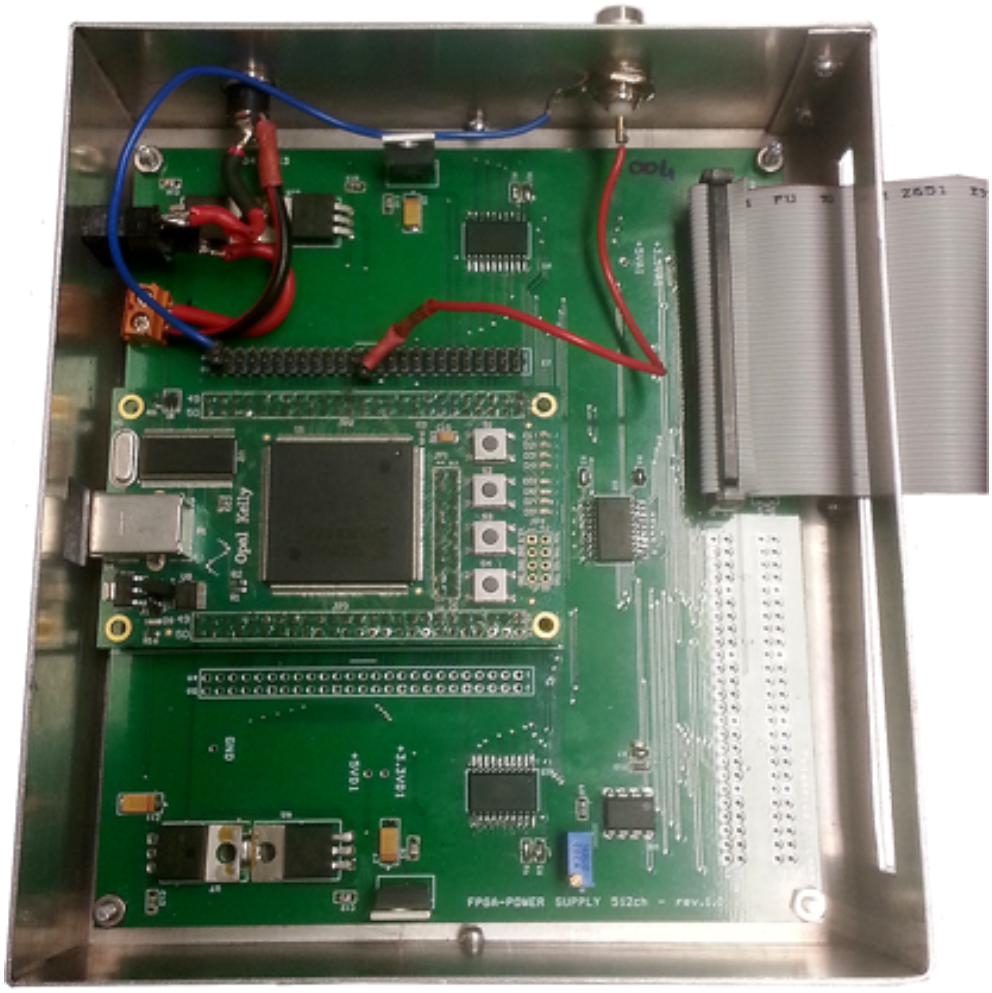

Figure 3.8: The FPGA master board

The FPGA is used to handle the communication between the electronics and the PC, master the timing of the AFE0064 boards and control the acquisitions

reset phases. Communication between the FPGA and PC happens over the standard Universal Serial Bus (USB) link. Once the measurement parameters and commands are set by the user and transmitted to the FPGA, the AFE0064 begins the measurement and integrates all input channels simultaneously.

3.4 BrachyPix – the "Magic Plate" software toolkit

The graphical user interface (GUI), "BrachyPix", was designed for the purpose of this research. It has been compiled under the C++ developing suite Qt rev5.3.1 and is used to manage the communication with the AFE system during acquisition and perform real time and post-processing analysis. The interface is used to perform the HDR source tracking algorithm and an automated determination of the dwell positions and times, as described in Chapter 5.

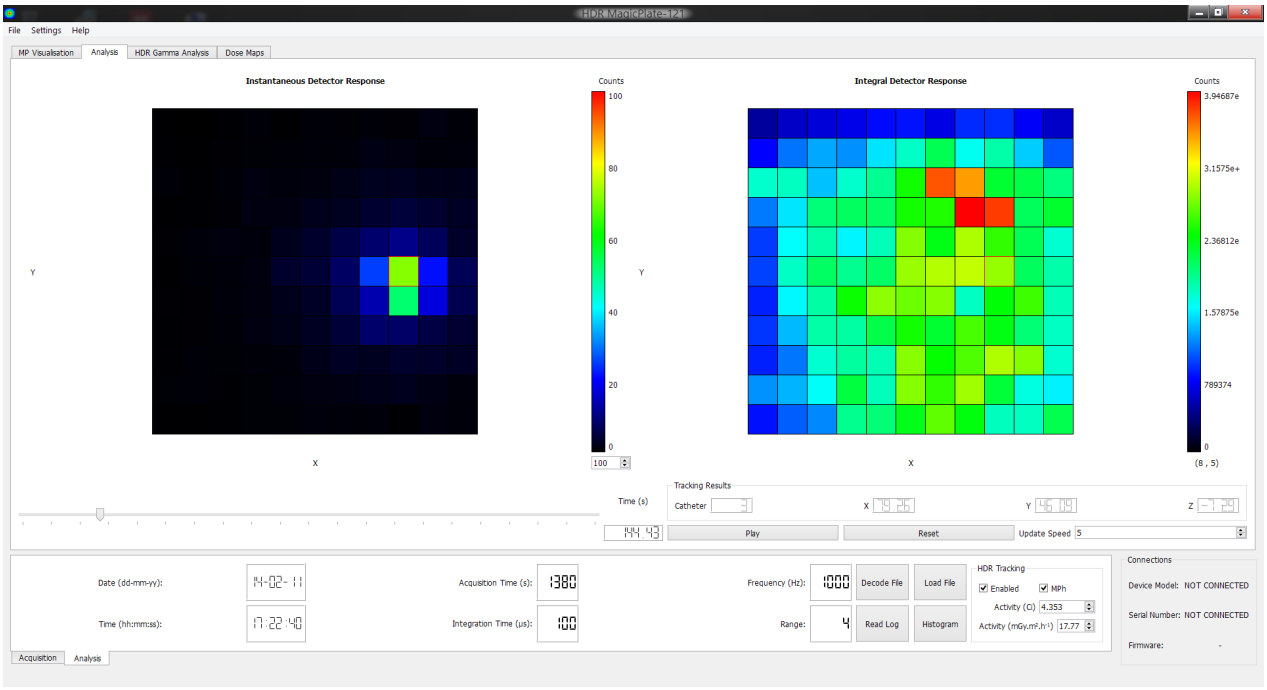

Figure 3.9: BrachyPix – frame-by-frame and integral response.

When the AFE DAQ system is connected, BrachyPix opens the communication to the FPGA over the USB 2.0 connection. When the connection is established, an instruction set is communicated to the FPGA to program the chip. The user is able to adjust the measurement parameters, such as: integration time, the total acquisition time, the AFE sensitivity range and the frequency of measurement. When measurement is

initialised through Brachy*Pix*, these parameters are sent to the AFE, with the start signal, to begin the acquisition.

Raw data is downloaded from the FPGA memory stack, with a maximum data transfer speed of 48 Mb/s, and is saved to a file on the computer storage. During measurement, the GUI decodes a single packet of the raw data to update the 2D detector response colour map, and calculate the source position at 100 frames per second. The system is capable of running at a minimum integration time of 14 μs and up to a stable maximum acquisition frequency of 10 kHz. The maximum integration time has been found to be 9920 μs, with an associated minimum acquisition frequency of 100 Hz.

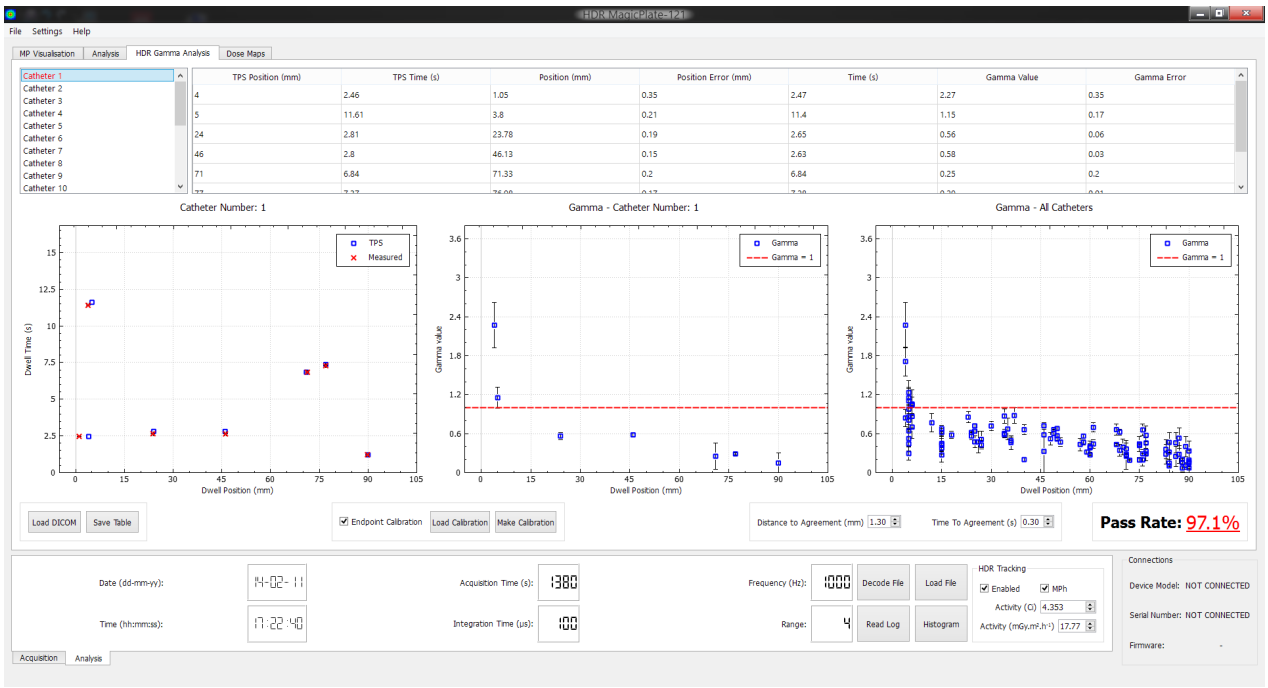

Figure 3.10: Brachy*Pix* – TPS and MPh catheter gamma analysis

The integration time, frequency and range are selected based upon the test performed. Typically, for pretreatment plan verification, performed in Chapters 8 and 9, the system is set to run at 100-200 μs integration time and at 1 kHz acquisition frequency.

As each measurement sample generates 769 bytes of data, a 15 minute acquisition will generate a file of approximately 660 MB, without using data compression. For the *in-vivo* feasibility testing (Chapter 10), the integration time was set to 9920 μs and 100 Hz to improve the signal-to-noise ratio, at a cost to decreasing the timing resolution. Measurements with high temporal resolution, performed at 5 – 10 kHz, can be used to determine the source motion profile (Chapter 7), but result in larger data sets per measurement. Adjustment of the measurement parameters, based on the experiment performed, can be used to achieve a balance between the timing resolution and total amount of data generated.

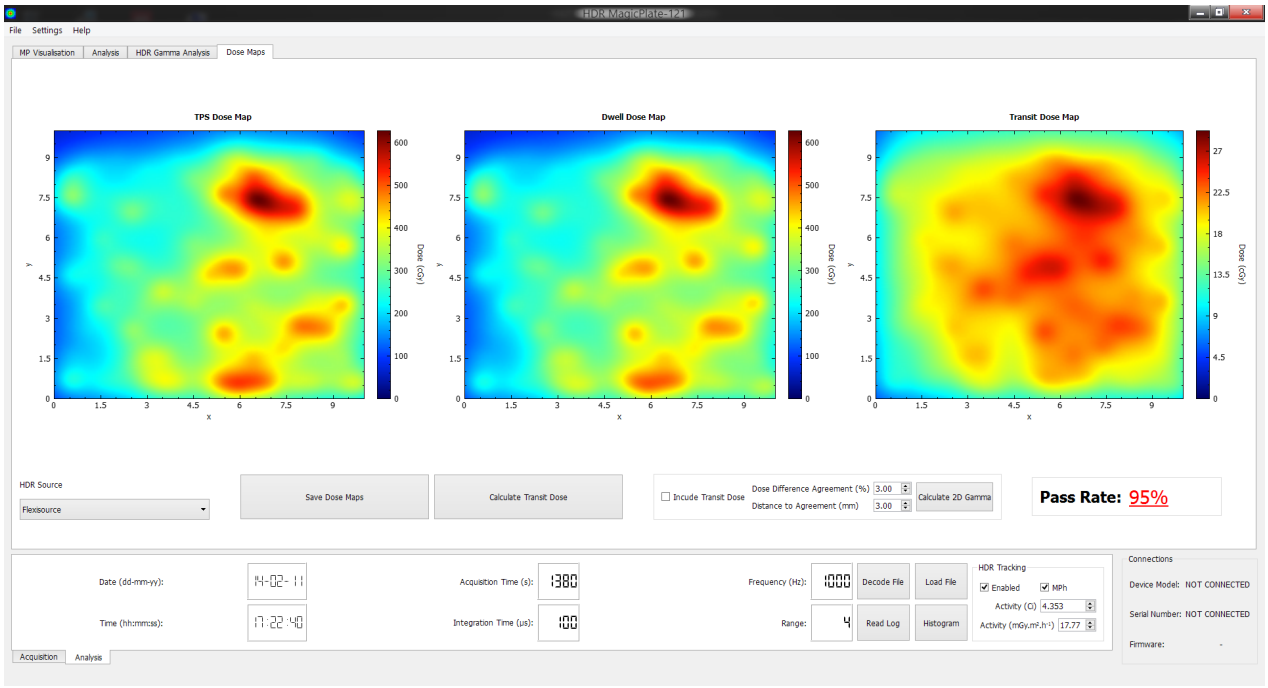

Figure 3.11: Brachy*Pix* – TPS, MPh measured and transit dose maps.

As described later in this thesis, methods for the determination of the source position in each measurement frame and the dwell positions and times were developed and implemented into the Brachy*Pix* post-processing analysis. The GUI features the ability to read DICOM files generated by the TPS, and to extract the planned source dwell

positions and times, relative to the catheter tip and the coordinate system used. The comparison between measured and planned dwell positions and times is displayed within the GUI, Figures 3.10 and 3.11.

Brachy*Pix* also features a dose calculation engine based upon the TG-43U1 protocol. It uses ^{192}Ir source parameters for both the Flexisource and microSelectron v.2., calculated using Monte Carlo methods by Granero et al. [86] and Taylor et al. [28]. Dose points calculated by the TPS and saved to the DICOM file were used for comparison of the values calculated by Brachy*Pix*.

3.5 Gafchromic EBT3 film

Gafchromic EBT3 film (Ashland ISP Advanced Materials, USA) lot #A07151302 was used to verify the dose calculated by the Nucletron ONCENTRA® TPS and Brachy*Pix* in Chapters 6 and 8. Due to the manufacturers stated dose range of "1 cGy to $>$ 40 Gy", the tested dose range of up to 90 Gy [87] and relatively weak energy dependence for energies as low as 50 keV [88, 89], the use of Gafchromic EBT3 appears well suited for use in ^{192}Ir HDR brachytherapy dosimetry and plan verification.

EBT3 film calibration

The film was calibrated by exposing five 10×10 cm^2 pieces to the HDR ^{192}Ir source. The MPh was disassembled and the top layer with catheter trenches was placed in a 30×30×30 cm^3 Solid Water® stack. A single piece of film was placed at the centre of the stack, and a single catheter was inserted into a trench directly over the centre of the film, at an approximate source-to-film distance of 16 mm. Nucletron ONCENTRA®

TPS was used to calculate the necessary time to deliver the required dose to the film, with the 5 pieces of film irradiated to 100, 200, 400, 600 and 1000 cGy using a single dwell position.

The film was pre-scanned and post-irradiation scanned using a 48-bit RGB transmission film scanner, the EPSON 10000XL, at a resolution of 300 dots per inch (DPI). No colour or sharpness corrections were applied and care was made to orientate and position the film consistently in scanner. Approximately 72 hours had passed between film irradiation and post-scanning to ensure the film response had stabilised. The calibration films were scanned and the image files were measured using IMAGEJ (version 1.47v). Six consecutive scans were performed for each piece of film to stabilise the performance of the scanner, and achieve consistency on the last three used for analysis.

Using IMAGEJ, a macro was created to select a circular region of interest with a diameter of 30 pixels (2.54 mm) that was moved around the image of the irradiation on the film until the minimum pixel value was detected, signifying the largest change in optical density. The net optical density ($netOD$) was determined for a piece of film exposed to a dose D_i as

$$netOD(D_i) = \log_{10}\left(\frac{I_0}{I(D_i)}\right) \tag{3.1}$$

where I_0 is equal to the average mean pixel value of the pre-scans and I is the average mean pixel value of the post-irradiated film. The dose response curves are plotted in

Figure 3.12. Uncertainties of the net optical density were calculated using

$$\sigma_{netOD}(D_i) = \frac{1}{\log_e 10}\sqrt{\left(\frac{\sigma_{I_0}}{I_0}\right)^2 + \left(\frac{\sigma_{I(D_i)}}{I(D_i)}\right)^2} \tag{3.2}$$

where σ_{I_0} and $\sigma_{I(D_i)}$ are the standard deviation of the pixel value of the pre-scan film and post-irradiated film, respectively.

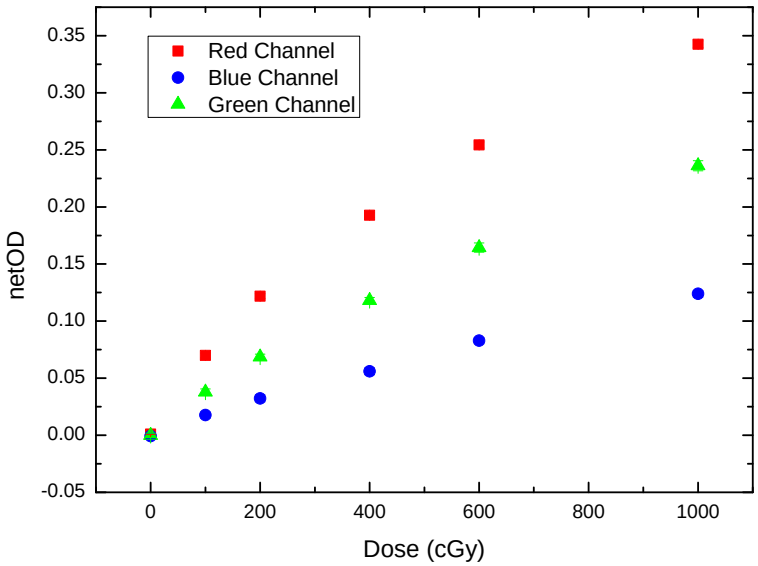

Figure 3.12: Dose response curves for the ^{192}Ir energy spectrum in red, green, blue channels.

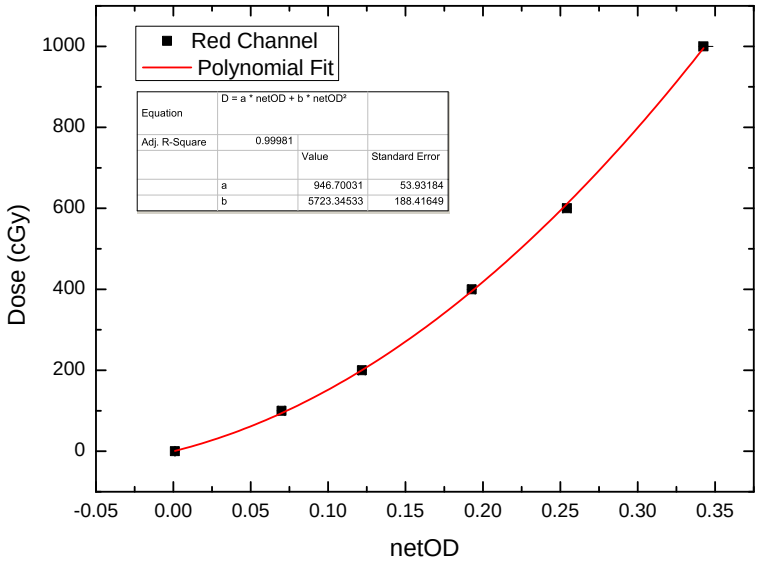

Figure 3.13: Calibration curve for the red channel using a 2nd order polynomial fit.

It is clear that for the ^{192}Ir photon energy range and the dose delivered, the red channel gives the largest change in optical density and, as such, was chosen for the dosimetry calibrations. In Figure 3.13, a 2nd order polynomial was used to fit the net optical density to absorbed dose D (cGy), by

$$D_{fit} = a \times netOD + b \times netOD^2 \tag{3.3}$$

where a = 946.7 ± 53.9 cGy and b = 5723.3 ± 188.4 cGy. The uncertainty in obtaining the dose measured at each point of interest was determined by

$$\sigma_D(\%) = \frac{\sqrt{(netOD \times \sigma_a)^2 + (netOD \times \sigma_b)^2 + (a + 2 \times b \times netOD)^2 \times \sigma_{netOD})^2}}{D_{fit}} \times 100 \tag{3.4}$$

EBT3 dose uncertainty

Sources of uncertainty and their estimated contributions are listed in Table 3.1. The average calibrated dose uncertainty, calculated using the above equation, was 3.5% (1 S.D). The total contribution of the uncertainty based upon the listed sources was 6.1% (1 S.D).

Uncertainty components	Type A (%)	Type B (%)
Source-to-film positioning		
- Calibration (16 mm)		1.3
- Measurement (6 mm)		3.3
Scanner homogeneity		0.2
Scanner reproducibility	0.1	
netOD measurement reproducibility	1.1	
Calibration curve		3.5
TPS dose calculations including S_k Measurements [90]		3.4
Total uncertainty (k=1)	6.1	

Table 3.1: EBT3 film dose calculations sources of uncertainty.

3.6 Discussion and conclusion

This chapter provides a description of the 2D detector, the "Magic Plate"and the pretreatment verification phantom, the "Magic Phantom". The AFE DAQ system that was connected to the MP was used to sample the measured generated integrated charge and relay the data to Brachy*Pix*, the software suite. Brachy*Pix* was designed to provide an interface between the user and the electronics system, allowing the user

to set the required measurement parameters, start and stop the measurement and perform the HDR source tracking, both in real time and in post-processing. EBT3 film was also introduced, with the dose calibration procedure presented, as it appears in further chapters in this thesis. The following chapter details the feasibility tests performed to characterise the use of the MP and AFE systems for use in HDR quality assurance.

Chapter 4

The feasibility of the "Magic Plate" for HDR Quality Assurance

This chapter presents the preliminary study performed to determine the suitability of the MP detector for use in HDR brachytherapy quality assurance[1]. The study assessed the baseline electronic noise measured by MP, the changing response of the MP at various distances from the HDR source and the angular dependence of the MP detectors.

The baseline noise was characterised for changing the integration times in order to investigate their effect during the pretreatment and *in-vivo* measurements. By varying the distance of the MP detector from the HDR source, the relative response of the MP could be compared to calculations made using the The TG-43U1 protocol, to determine the expected response and limitations of measurements for *in-vivo*. The response of the MP detector at different angles to the HDR source was investigated to

[1] Part of this chapter has been published in Medical Physics:
A. Espinoza, B. Beeksma, M. Petasecca, I. Fuduli, C. Porumb, D. Cutajar, S. Corde, M. Jackson, M. L. F. Lerch, and A. B. Rosenfeld, "The feasibility study and characterization of a two-dimensional diode array in "magic phantom" for high dose rate brachytherapy quality assurance.," Medical Physics, vol. 40, p. 111702, Nov. 2013.

learn the suitable orientation of the detector and compensation factors that may need to be applied.

Measurements were performed using the Nucletron microSelectron® mHDR-v.2. afterloader (Nucletron, an Elekta company, Elekta AB, Stockholm, Sweden) at the Prince of Wales Hospital, Sydney.

4.1 Electronic noise of the "Magic Plate" system

The MP will be used to determine the HDR source position, based on the measured charge generated in each detector within a set integration period. The electronic noise of the MP and the AFE DAQ system was characterised to ensure that there would be a minimal influence on measurements with the ^{192}Ir source. Due to the size of the sensitive volume of the MP detector element and the reduced radiation intensity at large distances, it is expected that the integrated current in the MP will be relatively low for *in-vivo* feasibility measurements and approach a similar order of magnitude as the baseline electronic noise.

Methods

The MP detector was placed into the MPh, inside the HDR treatment suite at the Prince of Wales Hospital. The baseline of the MP system per channel was defined as the generated current measured with minimised external radio-frequency influences and from the HDR source itself. Thus, during the measurement, light sources inside the room that were not needed were switched off and the ^{192}Ir source was secured inside the afterloader safe. For each 30 s measurement, the MP integration time was varied

from 14 μs up to 9920 μs. The sampling frequency of each acquisition with integration times between 14 and 920 μs was set to 1 kHz. For integration times greater than 920 μs, 100 Hz was used for the sampling frequency. The induced current in the MP and the AFE DAQ system was analysed to determine the sources of noise in the system.

Results

The average baseline for each AFE channel when connected to the MP is shown in Figure 4.1. Each error bar shows the variation of that channel's response (2 S.D) over 30 s acquisition time. The maximum integrated current was found to be below 12.5 pA for all input channels and integration times. The average integrated current across all MP detectors and AFE channels was found to decrease with increasing integration time, with values of approximately 1.26 $\pm$ 3.19 pA and 1.15 $\pm$ 2.93 pA (2 S.D) for the 100 μs and 9920 μs integration time, respectively.

It can, however, be distinctly seen that channels 0-63, found on the AFE chip 1, had a much larger baseline when compared to Channels 64-112 on the AFE chip 2. Whilst each AFE chip is connected to the same electronic circuit on the readout board, the placement of the individual AFE chips, the DC voltage regulators and the electrical tracks position and orientation, in respect to the external noise source, could influence the variation between the two chips.

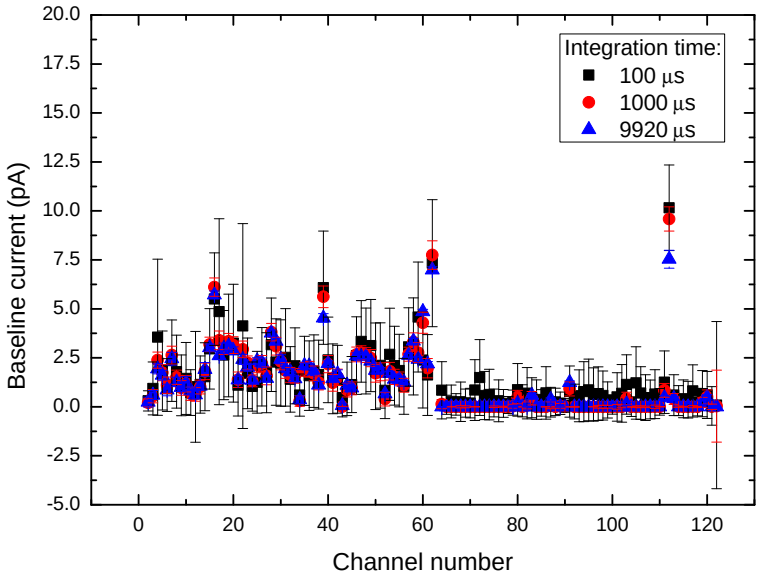

Figure 4.1: Baseline noise generated in the "Magic Plate" and the AFE DAQ system.

The response of a single AFE channel – Channel 61, for the 100 μs integration time and 1 kHz acquisition frequency is shown in Figure 4.2. This channel has a relatively constant response of an average of 7.96 $\pm$ 1.06 pA (2 S.D) over the duration of the measurement. Assuming that the noise level of each MP detector did not vary during measurements while using the ^{192}Ir source, a baseline subtraction was performed to ensure that the integrated current measured was strictly due to the HDR source.

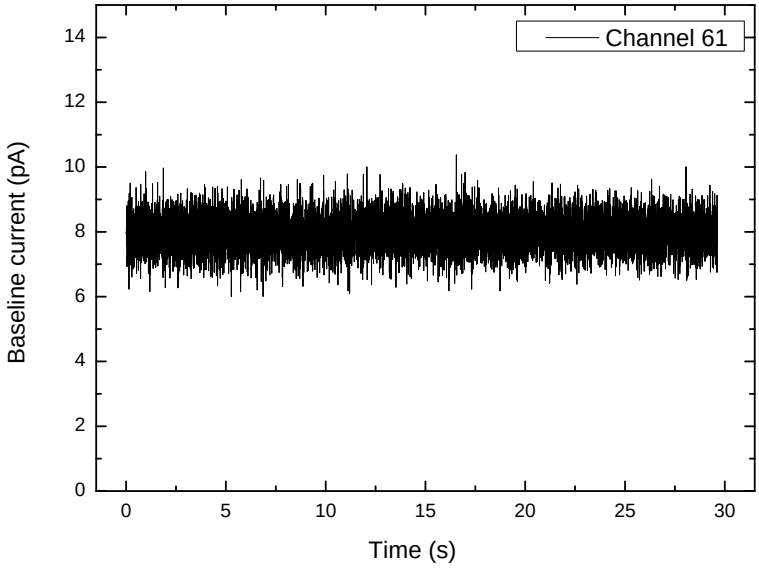

Figure 4.2: Baseline noise generated for Channel 61.

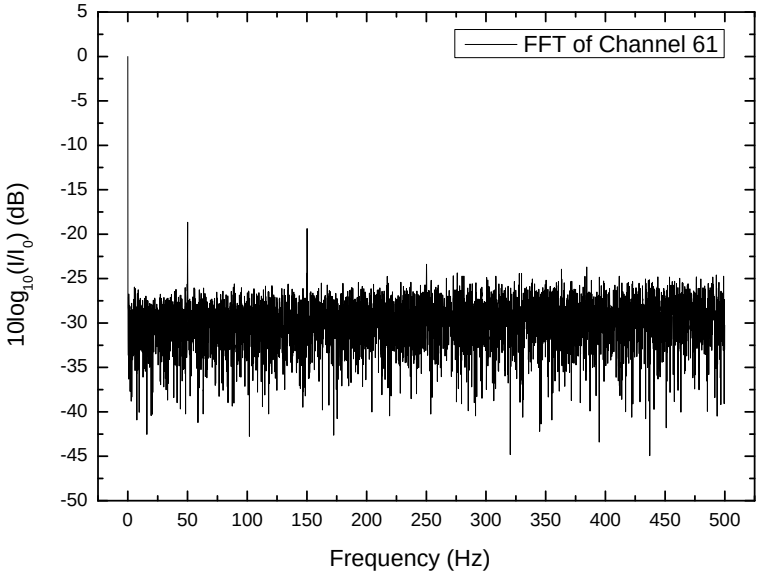

Figure 4.3: Fast Fourier transformation of Channel 61 response.

The sources of the noise were analysed using a Fast Fourier Transformation (FFT) to determine the frequency components of the channel response over time. Figure 4.3 shows that the majority of the spectrum is of a constant amplitude over the frequency range, which could be due to thermal noise from the MP detectors and the AFE DAQ

system. However, there are noticeable peaks at 50 and 150 Hz. This implies that the MP and AFE system are sensitive to the main power lines, which has a frequency of 50 Hz, used to power the system. The 150 Hz is most likely a harmonic of the power lines frequency.

4.2 The effect of backscatter material on the "Magic Plate" response

It is necessary to determine the appropriate level of backscatter material that can be used to simulate an infinite water volume, which is typically assumed by the TPS and the TG-43U1 protocol. It is expected that with increasing backscatter material, the response of the MP will increase.

Methods

The MPh was placed vertically onto a flat piece of dense foam, with equal thickness of SW placed on each side of the phantom, Figure 4.4. This set-up kept the MPh perpendicular to the treatment coach, and attempted to keep the MP away from scattering material that could adversely affect the results. Although there would be scattering of photons inside the treatment room, such as from the treatment devices and the patient coach, this method aimed to minimise these effects.

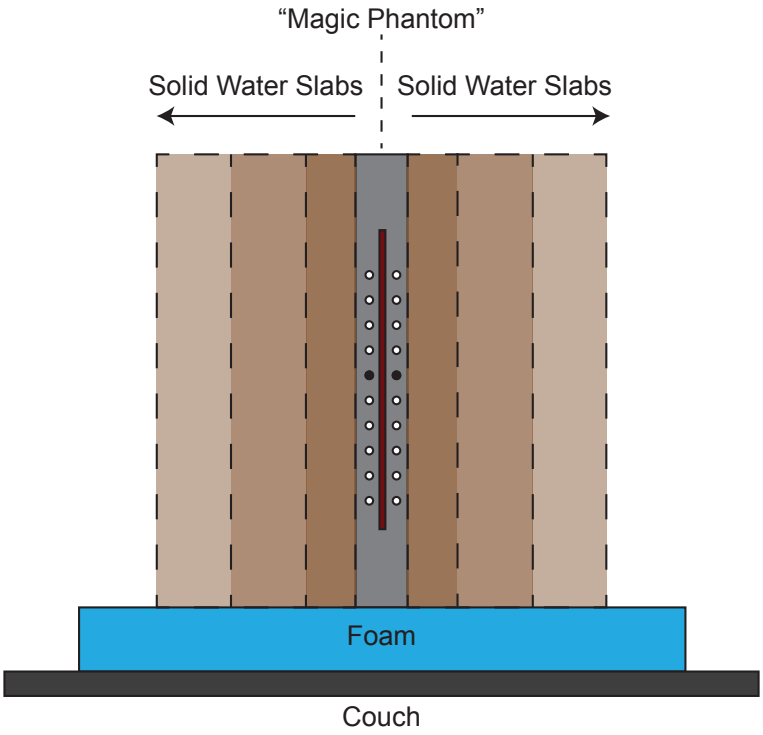

Figure 4.4: Backscatter test experimental set-up.

The MPh was configured so that the top and bottom row of catheters were directly next to each other. The HDR source was then programmed to dwell for 2 s at positions directly above and below the central MP detector. This measurement was performed with SW thickness from 0 – 120 mm on each side of the vertical MPh. The 0 cm backscatter thickness measurement used no SW pieces, but considered only the response due to the MPh itself (3 cm thickness in total).

At the time of measurement, it was not possible to obtain the final additional 3 cm of SW to create a 30×30×30 cm^3 phantom due to constraints in the clinic. The measurement was repeated 3 times per thickness, and the average integral response for the central detector from both dwell positions were calculated and were used to evaluate the change in response.

Results

The increase in the detector response with backscatter thickness, normalised to 0 cm SW, is shown in Figure 4.5. Errors were determined from the 2 S.D of the measured integral response. It was seen that the central detector response continues to increase with SW from 100 ± 0.29% to 103.94 ± 0.43% at the largest amount of backscatter material measured.

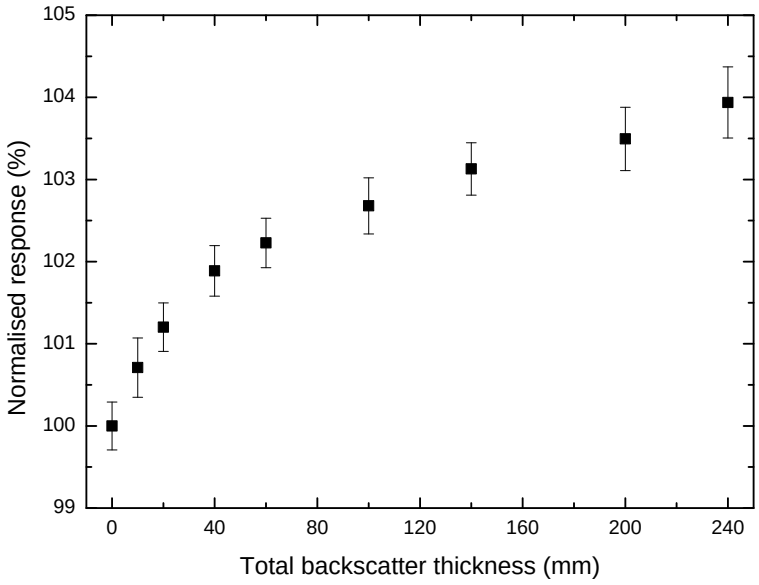

Figure 4.5: The "Magic Plate"detector response with increasing backscatter material.

The increase in detector response is largest between the 0 and 100 mm of SW on both sides of the MPh. The change in response begins to decrease with increasing amounts of backscatter material, and based on the trend it is estimated that backscatter amounts greater than 50 mm each side will result in a less than 1% increase in integral response.

4.3 Source-to-detector distance dose measurements

Accurate measurements of the dose rate at regions in immediate proximity to the source are imperative in HDR brachytherapy. Due to the large dose gradients associated with ^{192}Ir source, a slight change in measurement position leads to a large variation in measured dose rate. Determination of the position of the source using a triangulation algorithm requires an accurate knowledge of the relative source-to-detector distance (SDD) dose response of the MP in a water equivalent phantom. It is not essential that the measurement results match the expected data set, as it is expected that the energy dependence of the MP will cause discrepancies. It is, however, necessary to perform a characterisation so that an estimate of distance can be later calculated from a measured detector response.

Methods

The response of the MP due to the HDR ^{192}Ir source was measured within a 30×30×30 cm^3 SW phantom. The MP was placed above 100 mm of SW, and aligned so that the middle MP detector element was at the centre of the phantom. The HDR plastic catheter was aligned inside the phantom using the top slab of the MPh, ensuring that the catheter crossed over the middle detector of the MP. The SDD was changed from 7 mm to 151 mm by moving the HDR catheter position along the z-axis (Figure 4.6). The HDR source was then programmed to dwell directly perpendicular to the face of the sensitive volume of the middle MP detector, for a dwell time of 30 s.

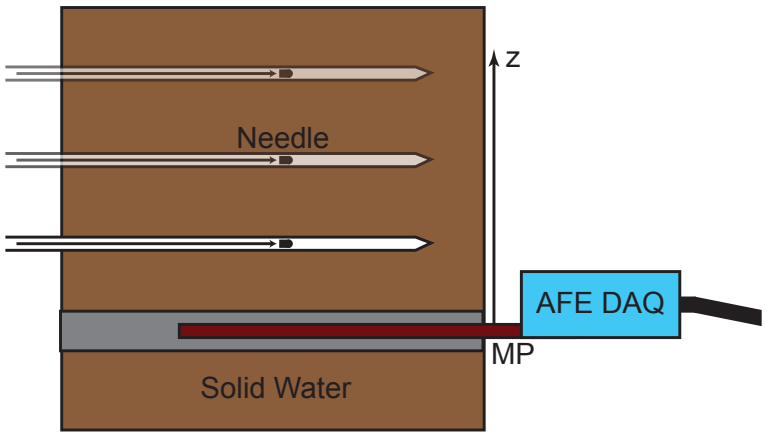

Figure 4.6: Source-to-detector distance dose experimental set-up.

The MP was then set to measure the generated current, before, during and after the source dwell. This allowed for a baseline subtraction to be performed on each channel of this measurement. As there is a low event rate associated with measurements at large SDDs, to obtain a detector response with low fluctuations, the integration time was varied from 100 μs to 9920 μs.

The uncertainty associated with the alignment in the x and y plane was estimated to be as large as $\pm$3.5 mm. It is estimated that the SW thickness used were accurate to 0.05 mm. Based on a the maximum geometrical distance using the $\pm$ 3.5 mm and the accuracy of the SW thickness, a determination of the source-to-detector distance was calculated to a maximum of 0.8 mm at 7 mm, which decreases as the SDD becomes larger.

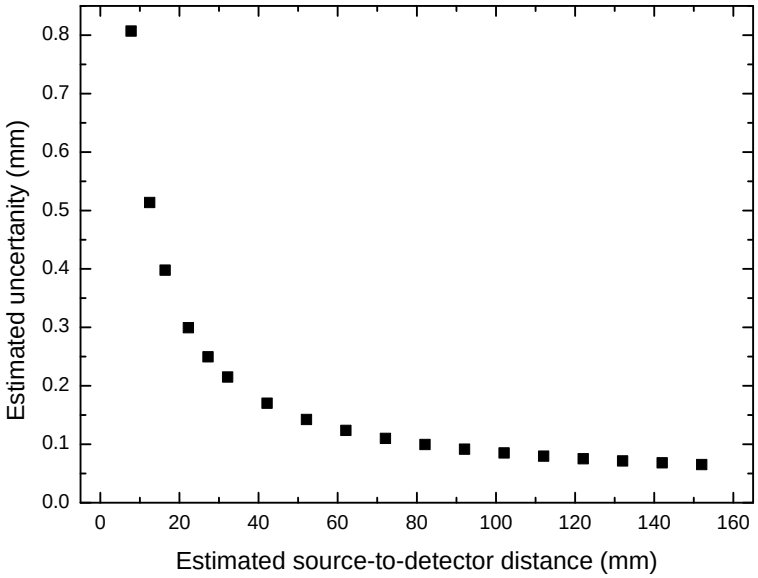

Figure 4.7: The calculated source-to-detector distance uncertainty.

Results

The relative SDD response of the MP to a ^{192}Ir source is shown in Figure 4.8. Shown for comparison is expected response for the Nucletron microSelectron® mHDR-v.2. afterloader source, based off the Monte Carlo obtained data by Taylor and Rogers [28]. The MP response was normalised to 100% at 16 mm SDD. This distance was chosen to minimise the effect of positional uncertainty introduced in aligning the MP and the estimated effect of the energy response of the diode associated with the softening of the ^{192}Ir spectra with increased SDD. The uncertainty in normalised response is based on the integral standard deviation of three measurements taken at each depth. Each uncertainty is then summed in quadrature with the uncertainty at the normalisation point at 16 mm (2 S.D).

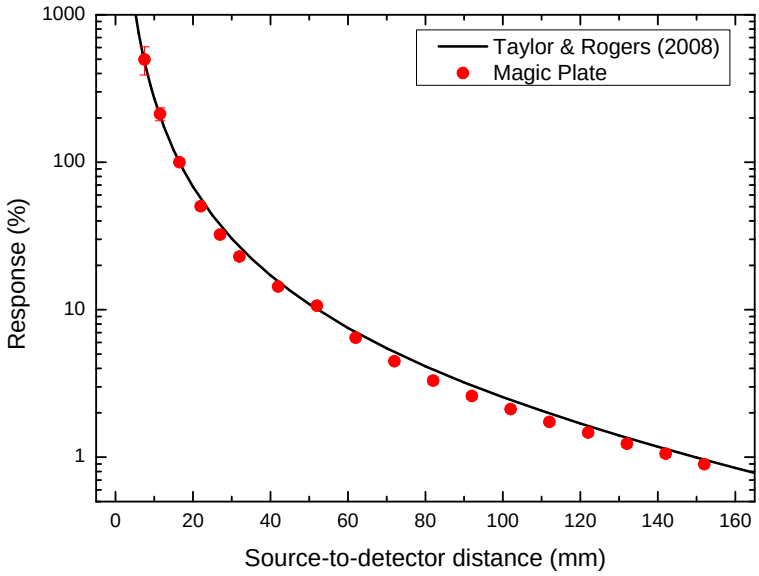

Figure 4.8: Source-to-detector distance dose experimental results.

Based on the TG-43U1 protocol calculation of the radial dose function was performed using the MP SDD dose response, taking into the account the radial distance and the ^{192}Ir source physical dimensions, shown in Figure 4.9. This calculation takes into account the $1/r^2$ dependence and allows for deviations from the theoretical to be seen. The uncertainties (2 S.D) shown in the figure are a combination of the uncertainty in normalised response (Type A) and the uncertainty in determining the SDD (Type B) found in Figure 4.7.

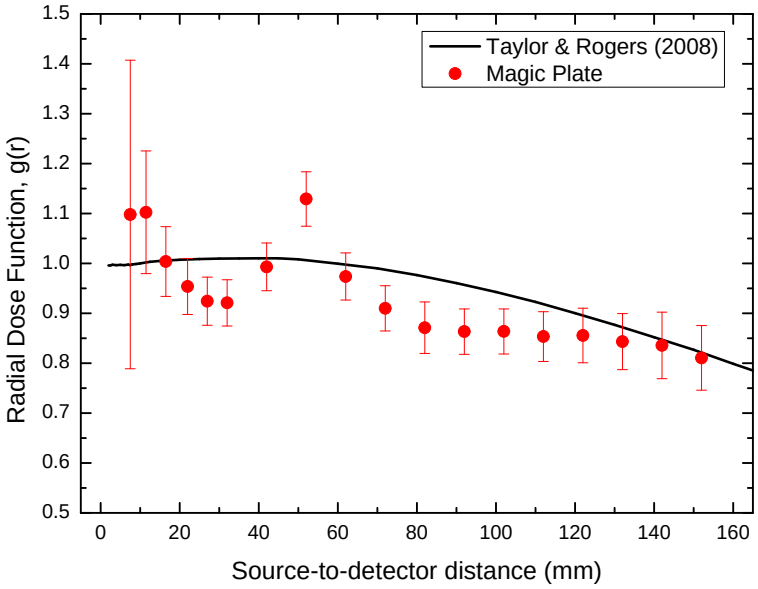

Figure 4.9: Experimentally measured radial dose function.

Due to the lifetime of ^{192}Ir, the HDR source is typically replaced every 3-4 months. The current generated within the MP is therefore expected to be at a maximum when the source has recently been replaced, at approximately 48 mGy.m^2.h^{-1}, and lowest when the source is due to be replaced for the same SDD. When measuring at large SDDs, it is vital that the MP system is capable of obtaining a signal suitable for performing an accurate measurement.

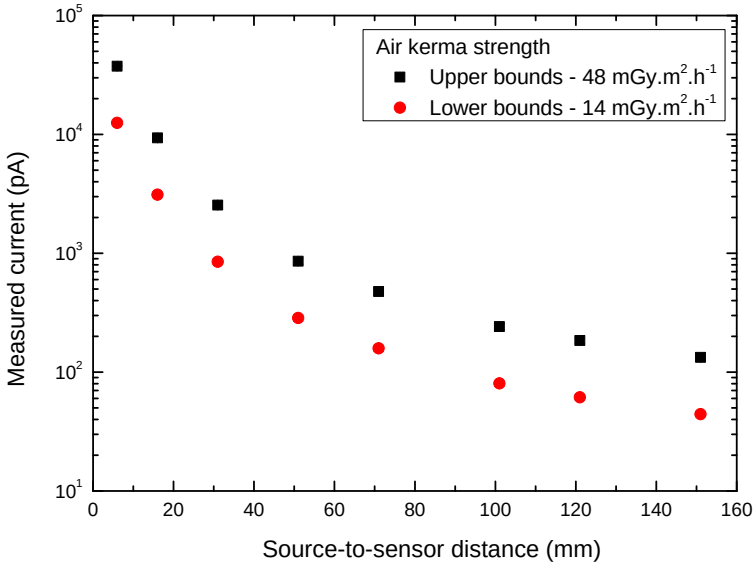

Figure 4.10: The expected upper and lower bounds of current generated in the "Magic Plate".

To derive the expected maximum and minimum generated current with the MP for each SDD, the MP response values for the SDD were divided by the source activity at the time of measurement, and multiplied by either the maximum or minimum source activity to be expected. Figure 4.10 shows the expected current generated for these two cases for varying depths within Solid Water®. The lower bounds is expected to be larger than the maximum baseline current by factor of 25.

4.4 Angular dependence of the "Magic Plate"

The intrinsic asymmetric structure of the epitaxial diode of MP and the energy range of the gamma photons emitted by the ^{192}Ir may result in directional dependence for each detector. To predict the angular response of the epitaxial diodes in the MP for any position of the source, it is necessary to characterise the angular response of the single diode of the array along both the azimuth and polar angles. The MP detectors

were mounted onto the Kapton substrate prior to testing, so it is difficult to assess the angular dependence of each detector without removal. To overcome this, the angular dependence of two epitaxial diodes from the same manufacturing batch were tested that were separately mounted onto a Kapton pigtail.

Due to the highly controlled production process, reproducibility of detectors in the same batch is high. In addition, the CMRP patented technique used to embed the detector into the MP flexible carrier attempts to reduce the possibility of introducing any additional angular dependence, and is also used in the assembly process of the detectors onto the Kapton pigtails.

Methods

To measure the azimuth angular response, the diode was placed in a rotatable cylindrical phantom that was encased in a cubic phantom of 30×30×30 cm^3 SW, to ensure full body scattering conditions. A single HDR catheter was placed at 20 mm SDD, as seen in Figure 4.11. The initial position, $\theta = 0°$, was taken as the orientation of the detector's sensitive volume was "face-up" relative to the source. Using the Nucletron microSelectron® mHDR-v.2. afterloader source, the HDR afterloader was programmed to position the source to the final dwell position at the end of the catheter, dwell for 45 seconds at this position and then retract. The cylindrical insert was rotated in a clockwise direction for a total of 180° rotation with measurements taken at every 30° increment.

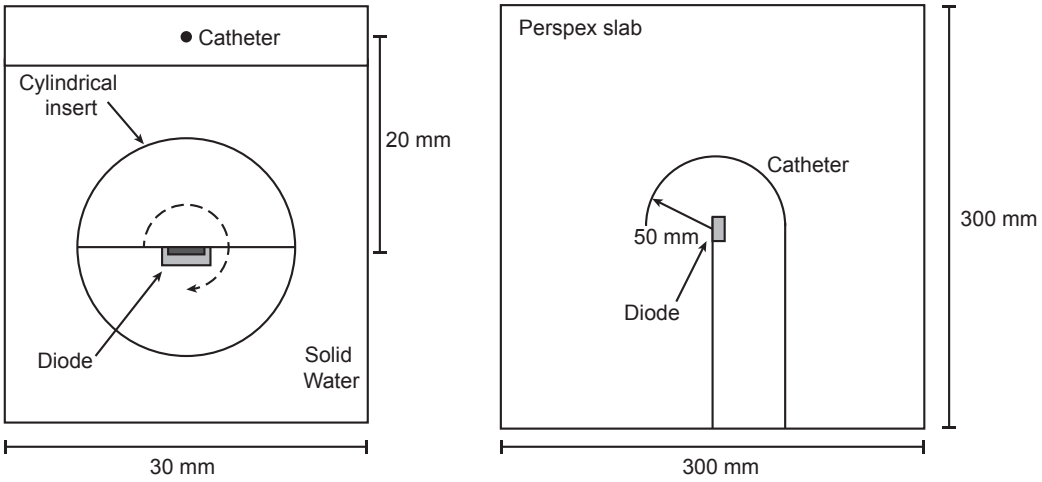

Figure 4.11: Azimuth and Polar measurement set-up.

Polar angular response characterisation required the design of a specific phantom where the HDR source would move on an arc of radius 50 mm, centred at the detector to minimise the effect of any variation in the SDD and the anisotropy effects of the source. A schematic diagram of the phantom is shown in Figure 4.11. The detector was placed side on, into a groove that had been machined into the phantom. In this orientation, when the source was at the final dwell position of the catheter, the detector's sensitive volume faced the perpendicular axis of the source at 0°. By stepping the source in 13 mm increments around the 5 cm arc radius, a step of 15° could be obtained. The source was driven around an arc of 180°.

Results

The directional dependence of the epitaxial diode response is shown in Figure 4.12. Both data sets are normalised to 100% at 0°. The azimuth data was taken using the cylindrical insert as shown in Figure 4.11. The uncertainty in determining the angle for this phantom was ± 2.5° (Type B). The polar data was taken using the phantom shown in Figure 4.11. As the source was driven by the HDR loader to set points

with 1 mm accuracy, the estimated uncertainty is calculated to be 0.6°. The Type A uncertainty in response in both sets is ± 1.6% (2 S.D.), and is primarily due to electronic noise associated with using a single detector on a kapton tail.

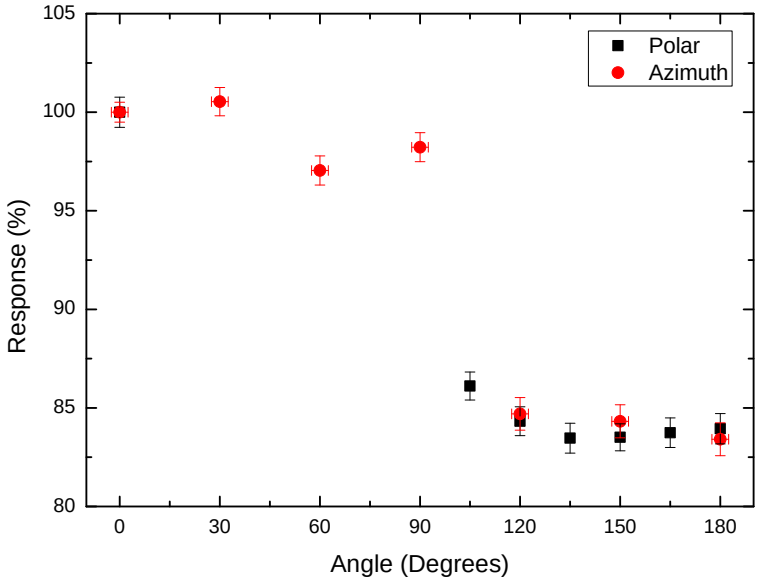

Figure 4.12: The angular response of the epitaxial diode.

Both data sets show a variation in response of the diode of 15% between the top face (0°) and bottom face (180°) of the epitaxial detector, but is uniform in ± 5% of variation for angles range of 0 ± 60°and 180 ± 60°. Data measured in the polar direction between 0 – 110 ° were excluded due to the difficulty in placing the sensitive volume of the detector directly at the centre of the rotation, resulting in aberrant values.

4.5 Discussion and conclusion

The MP detector and the AFE DAQ system have shown to exhibit a low baseline current of an average of 1.62 ± 1.65 pA (2 S.D). Due to the radio-frequency shielding

of the MP, it is expected that the majority of baseline current be due to the connected electronics readout system. The majority of the baseline appears on only one of the AFE chips, and could be due to the connection of that side of the MP to the AFE board, and the connection and placement of the AFE chip on the board. Influence due to mains power seems to have the most impact on the baseline current level of these channels and the AFE DAQ system board and encasing of the electronics could be refined to minimise this in later development versions. For fluctuations not centred at 0, it would be possible to perform a baseline subtraction of the centring value for those MP detectors.

A characterisation of the MP response with varying amount of SW was performed to determine the suitable amount backscatter needed for measurement. It was found that while there was an increase in response with material, the change decreased following an exponential trend. A minimum of 50 mm of SW placed both above and below the MPh was found to be sufficient, with amounts larger than this equating to a less than 1% increase. For consistency of measurement, all MPh pre-treatment testing in this work was performed using a $30\times30\times30$ cm^3 phantom, with all other measurements using at least a 50 mm thickness.

By varying the HDR source-to-detector distance through SW, measurements of the MP response were obtained that can be used to estimate the SDD during the triangulation procedure. It was seen that the MP did not exhibit any over-response and results matched the TG-43U1 protocol data specified for the Nucletron microSelectron® mHDR-v.2. afterloader source. The MP matched the radial dose function data with an average difference of 2.5%, over the depth of 7 – 150 mm, with an maximum difference of 12.4%. However, this result is markedly different to that previously presented by Espinoza et al. [16], where a large over-response was seen for SDD over 15 mm,

with a 40% difference at 70 mm. It is suggested that this over-response could have been due to the sensitivity of this silicon detector to the larger lower energy scatter contribution. This previous study was performed using a MP sample that had been pre-irradiated to 20 kGy equivalent dose in water.

All of the results presented in this work, except for the angular dependence measurements found within this chapter, were performed with a different sample of MP, which has had an estimated pre-irradiation of greater than 40 kGy equivalent dose in water. This second MP also had a 40 μm layer of aluminium surrounding the complete kapton substrate to shield the detector from radio-frequency noise. This possibly filtering of the low energy through the aluminium shielding, could explain the lack of over-response, as relatively higher energy contributions could be deposited. However, this would have to be confirmed through an in-depth investigation, involving experiments and Monte Carlo simulations.

The angular dependence measured found a variation of 15% in the response between the top and bottom face of the epitaxial detector and less than a 5% variation for both faces for $\pm$ 60°. It is suggested that the angular dependence is due to the asymmetry involved in a silicon detector when the depletion layer is close to the front surface [91, 92]. As there is an asymmetrical boundary region surrounding the sensitive volume, where charge collection is not ideal, this results in a lower amount of charge collected per detected event in this part of the detector. The structure of the detector, in conjunction with the energy dependence of the response of silicon for the ^{192}Ir source and attenuation of secondary particles through the passive silicon, is most likely the cause of the observed variation of the response. This could be investigated further using Monte Carlo simulations by reproducing the detector design and sensitive volume, and rotating it in respect to a HDR source. The obtained angular response

will be used to provide a small correction factor for the source position calculation, when the source is not directly above or below the detector.

Chapter 5

The determination of dwell positions and times using the "Magic Plate"

The previous chapter assessed the feasibility of the MP for use in high dose rate brachytherapy. The system was shown to have a low baseline current, a large dynamic range of measurement that allows for both close and far away radiation detection, and a minimal angular dependence around the top and bottom face of each detector.

This chapter describes the method of source position localisation using multiple detector elements, that has been implemented into the analysis software[2]. A description of the method for the calculation of the source dwell positions and times for a measured

[2] Part of this chapter has been published in Medical Physics:

A. Espinoza, B. Beeksma, M. Petasecca, I. Fuduli, C. Porumb, D. Cutajar, S. Corde, M. Jackson, M. L. F. Lerch, and A. B. Rosenfeld, "The feasibility study and characterization of a two-dimensional diode array in "magic phantom" for high dose rate brachytherapy quality assurance.," Medical Physics, vol. 40, p. 111702, Nov. 2013.

A. Espinoza, M. Petasecca, I. Fuduli, A. Howie, J. Bucci, S. Corde, M. Jackson, M. L. F. Lerch, and A. B. Rosenfeld, "The evaluation of a 2D diode array in "magic phantom" for use in high dose rate brachytherapy pretreatment quality assurance," Medical Physics, vol. 42, no. 2, pp. 663-673, 2015

treatment is also presented.

5.1 Source localisation using multiple detectors

A method for determining the position of the HDR source was devised and patented by A. Rozenfeld and M. Zaider [93,94]. Localisation is based upon an iterative procedure where the source position is estimated, and then repeatedly refined based upon the agreement of the predicted geometric distance from the source to the detectors against those measured by the MP detectors. This method is implemented into Brachy*Pix* and is used to calculate the source position with a minimal amount of processing.

The MP is a 2D array of diodes where each detector element is measuring the energy deposited by the gamma photons or secondary electrons emitted by a source with no directional information. However, the radial distance, r, can be estimated by taking into account the diode response, normalised to the activity of the source, as a function of distance and angle. The correlation of the responses of three or more detectors can be used to identify the position of the source in three dimensions using a triangulation method based on estimation and iteration. As three non-collinear detectors are the minimum for localisation of the source, selection of more than three allows for redundancy in estimation of the x, y and z coordinates of the source, and inaccuracy reduction.

Every MP detector can be used for estimating the source position, however only the detector with the highest response and it's immediate neighbours (typically a 3×3 subset) were considered, when used in phantom. This was done to minimise the uncertainty in the calculation due to the lower signal from the detectors at larger

distances from the source, as well as minimise uncertainty due to the non-isotropic response of the detector and source itself. However, a larger number of detectors are selected for use in *in-vivo* measurements, as the MP response is more uniform at larger SDDs due to the flattening of the dose profile. This technique requires the accurate characterisation of the detector response to ^{192}Ir gamma spectrum in terms of relative SDD dose and angular responses, as was performed in Chapter 4.

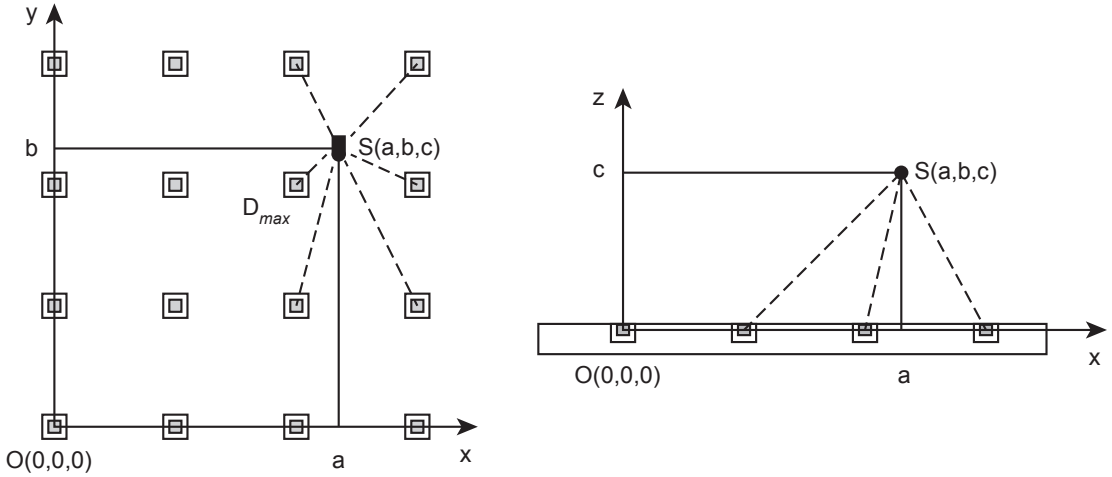

Figure 5.1: The "Magic Plate" coordinate system.

The origin of the coordinate system is set at the bottom left of the MP (Figure 5.1) and is used to provide the coordinates of each detector d_i on the "Magic Plate". The HDR source is located at position $S(a, b, c)$, relative to the coordinate system.

The data acquisition system integrates the current generated in each MP detector during a set integration time. The software tool searches the data set for the detector with the highest response, shown as detector D_{max} in the coordinate system. The detector's index, i, within the array is determined and the responses of the 8 surrounding detectors are retained. When the detector with the highest response is found to be on the edges of MP, a larger number of surrounding detectors are included.

The response of the i-th detector, R_i, is a function of its distance, r_i, from the HDR source. A fitting function based upon the SDD dose response measured in Chapter 4 for angle $\theta = 0°$, is

$$R_i = f(r_i) \times S_K \times \frac{R_0}{S_{K0}} \tag{5.1}$$

where S_K is the source strength at the time of measurement, and R_0 is the average current of the MP at SDD 15 mm, at source strength S_{K0}. The distance between the source and the detector i, can then be calculated by the inverse function

$$r_i = f^{-1}\left(\frac{R_i \times S_{K0}}{S_K \times R_0}\right) \tag{5.2}$$

The calculation of SDD using the inverse function results in an average absolute difference of 0.82 ± 1.10 mm (2 S.D) across the range of SDDs in Figure 4.8. The uncertainty in determining the calculated SDD based on the fitting procedure was on average 1.15 ± 0.73% This estimation of the distance from the source to the detector is calculated based upon the assumption that the detectors do not display an angular dependence. However, once a rough source estimation is performed, the angular correction factors is applied and the algorithm is repeated. Based on the several derived distances, r_i, the source position $S_{es}(a, b, c)$, in the MP frame is estimated. The geometrical distance, d_i, between S_{es} and the coordinate of the i-th detector $D_i(x_i, y_i, z_i)$, is calculated by

$$d_i(a, b, c) = \sqrt{(a - x_i)^2 + (b - y_i)^2 + (c - z_i)^2} \tag{5.3}$$

To determine the true source position, the geometrical distance, d_i, is fitted to the derived distance, r_i, by adjusting the estimated source position. Employing a non-

linear *least squares fit* method to determine the estimated source position, the best fit requires that an estimate of error assessment be at a minimum value [95]. In least squares fitting, the estimate of error assessment can be expressed as the sum of squares of the relative error, χ^2

$$\chi^2(a,b,c) = \sum_{i=1}^{n} \left(\frac{d_i(a_n, b_n, c_n; x_i, y_i, z_i) - r_i}{r_i} \right)^2 \tag{5.4}$$

and assumes that the derived distance, r_i, is correct. As there is an uncertainty associated with determining r_i, if the estimated source position were equal to the true source position, then calculating the square of the sums of the percentage difference of the values of d_i and r_i (Equation 5.4) would result in a minimum value.

A theoretical calculation of χ^2 was performed by estimating the dose rate for each MP diode for a source coordinate of $S(40\text{mm}, 50\text{mm}, 10\text{mm})$ using the TG-43U1 protocol. The dose rate was then converted into radial distance by the inverse function, and a 3D χ^2 map was calculated. The map was calculated by varying the estimated source position, S_{es} from 0-100 mm in all 3 dimensions, with a step of 0.2 mm, and calculating χ^2. The 2D χ^2 map for the estimated source position at $z = 10$ mm is shown in Figure 5.2

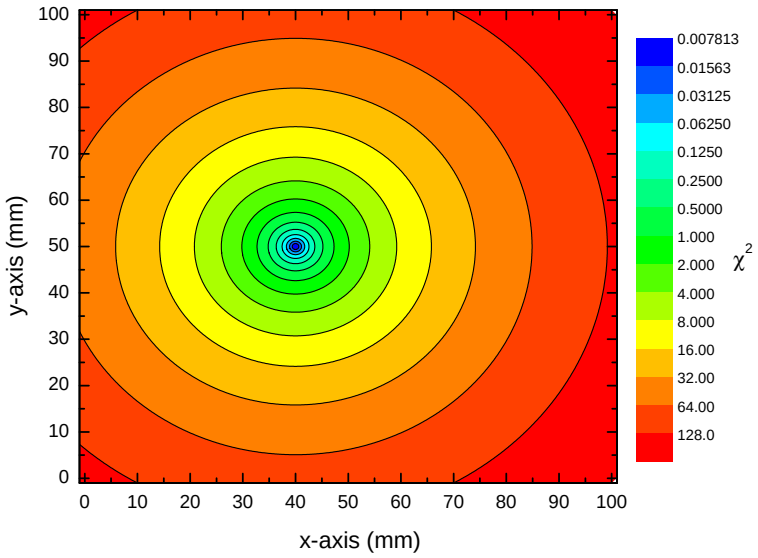

Figure 5.2: χ^2 for z = 10 mm.

It can be seen that for the $z = 10$ mm plane, there is only one global minimum, at $P(40, 50)$. It is to be noted that the scale is in powers of 2, meaning that the is a very large gradient towards this minimum. By taking a line profile along each of the source coordinates (Figure 5.3), it is possible to see that the minimum value of χ^2 for each coordinate matches that the modelled source coordinate.

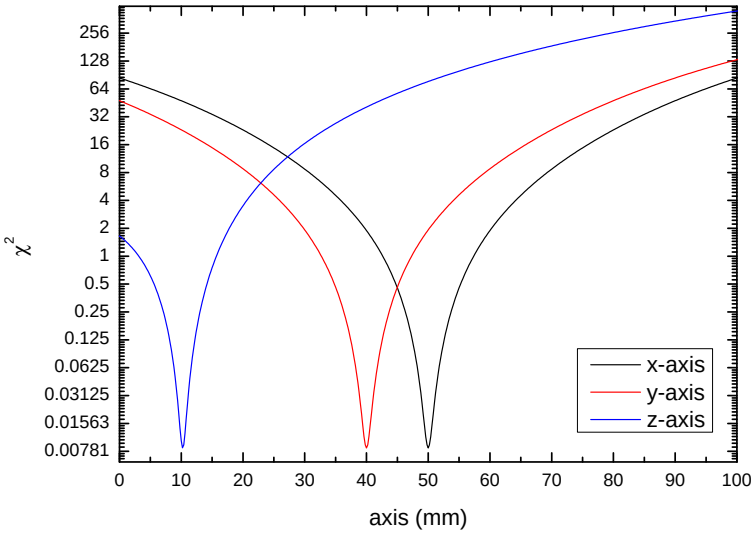

Figure 5.3: χ^2 2D profile.

Minimising the estimate of error

Determining a source position that gives the minimal value to the estimate of error assessment, χ^2, can be performed in multiple ways. One method is to compute by a brute force approach, where each source coordinate is adjusted individually until a minimum value is determined, similar to that used to generate Figure 5.2. For this work, a multi-variable Newton's method approach has been adopted to determine the source position in three dimensions.

Newton's method is used to determine the roots of a function by finding successively better approximations. In this analysis, it is necessary to determine the minimum values of χ^2 for all three dimensions of the estimated source position, and can be expressed as

$$\frac{\partial \chi^2(a,b,c)}{\partial a} = \frac{\partial \chi^2(a,b,c)}{\partial b} = \frac{\partial \chi^2(a,b,c)}{\partial c} = 0 \tag{5.5}$$

Newton's method for the three source coordinates can be expressed for the k-th iteration as

$$\begin{aligned} a^k &= a^{k-1} - \delta a^{k-1} \\ b^k &= b^{k-1} - \delta b^{k-1} \\ c^k &= c^{k-1} - \delta c^{k-1} \end{aligned} \tag{5.6}$$

where δa, δb and δc are the changes made to the source position to produce the improved approximation. These changes can be determined by solving a set of linear

equations, expressed in matrix form as

$$\begin{bmatrix} \frac{\partial^2\chi^2}{\partial a^2} & \frac{\partial^2\chi^2}{\partial a\partial b} & \frac{\partial^2\chi^2}{\partial a\partial c} \\ \frac{\partial^2\chi^2}{\partial b\partial a} & \frac{\partial^2\chi^2}{\partial b^2} & \frac{\partial^2\chi^2}{\partial b\partial c} \\ \frac{\partial^2\chi^2}{\partial c\partial a} & \frac{\partial^2\chi^2}{\partial c\partial b} & \frac{\partial^2\chi^2}{\partial c^2} \end{bmatrix} \begin{bmatrix} \delta a \\ \delta b \\ \delta c \end{bmatrix} = \begin{bmatrix} \frac{\partial\chi}{\partial a} \\ \frac{\partial\chi}{\partial b} \\ \frac{\partial\chi}{\partial c} \end{bmatrix} \tag{5.7}$$

This process is repeated until all δ's are sufficiently small, or until further estimations of the source coordinates fail to reduce χ^2. This approach can converge rapidly to a minimum when close, as all three source coordinates are modified in a single iteration, but requires a suitable initial guess to increase the likelihood of convergence.

The initial guess is determined by the coordinates of the detector with the highest response, $D_{max}(x_{max}, y_{max}, z = 0)$, as the source is assumed to be closest to this position. The sum of the squares is calculated using the first estimation of the source position,

$$S^0_{es}(a^0, b^0, c^0) = S_{es}(x_{max}, y_{max}, r_{max}) \tag{5.8}$$

Once an estimation of the source position is found, a correction factor is applied to the response of each of the MP detectors to take into account the angular dependence of the detectors found in Chapter 4. The source position is then re-estimated using the above method, but uses the initial estimated source position of the previous calculation.

5.2 Dwell position and time calculation

A method for determining the HDR ^{192}Ir source position using the two dimensional detector array MP has been introduced. For every measurement frame where the

detectors' response is above a threshold value, a calculation of the source position is performed. For pretreatment verification using MPh, two rows of 10 catheters are inserted into trenches 6 mm above and below the MP array. The catheter's are spaced at 10 mm, with the above row placed between the columns of the MP detector array, and the below row directly aligned with the detector columns. Using the coordinate system previously described, the catheters are at z = ±6 mm, and at an x-coordinate along the detector rows, with the catheter length along the y-coordinate.

Using the result of the source tracking algorithm, the x-y-z measurement of the source is translated to catheter number and position in the catheter, at each frame of measurement. As the MP DAQ acquires the response of the detectors at a set frequency it is possible to see how the position of the source varies with time.

Figure 5.4 shows the theoretical motion of the HDR source moving along the y-coordinate with a 10 mm step size, and 2 second dwell time. The source starts from outside the catheter, is driven to the position 100 mm in the catheter and then moves towards the tip of the catheter. This theoretical calculation neglects the transit motion of the source from dwell position to dwell position and assumes no fluctuations in the determination of the source position at each point.

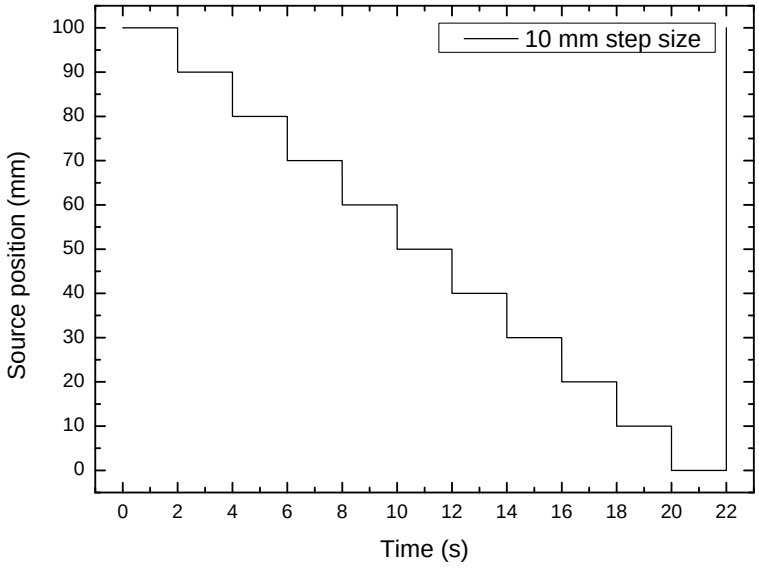

Figure 5.4: Theoretical source tracking - 10 mm step size, 2 second dwell.

From this source tracking calculation, it is possible to generate a position-frequency histogram, Figure 5.5, where each count corresponds to a single calculation of the source at that position. The bin width is set to 0.1 mm and accepts positions from -5 to 105 mm. When the source is at the same position for multiple measurements, i.e. when the source is dwelling, multiple counts at that position form a peak.

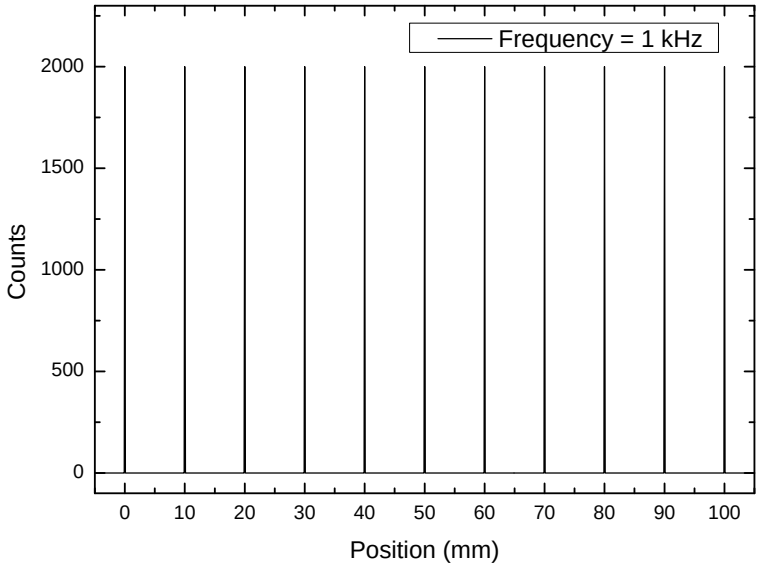

Figure 5.5: Theoretical dwell position-time histogram – 10 mm step size, 2 second dwell.

The number of counts under each peak of the histogram corresponds to the measured dwell time, as the time for each count is dependent on the sampling frequency, F_{meas}, of the system. Each count in bin i is converted to time t_i by

$$t_i = \frac{count_i}{F_{meas}} \tag{5.9}$$

The start and end positions, x_s and x_e respectively, of each peak are determined based upon a threshold of 0.02 s. The dwell time is then calculated by summing up the time in the histogram bin from the peak start and end

$$t_{dwell} = \sum_{i=x_s}^{x_e} t_i \tag{5.10}$$

The dwell position is calculated by the determining the centre of the peak by

$$x_{dwell} = \frac{\sum_{i=x_s}^{x_e} x_i t_i}{t_{dwell}} \tag{5.11}$$

and uncertainty is determined by the centre of the peak and the standard deviation, σ_{dwell}

$$\sigma_{dwell} = \sqrt{\frac{\sum_{i=x_s}^{x_e} x_i^2 t_i}{t_{dwell}} - x_{dwell}^2} \tag{5.12}$$

The error in dwell position is taken by 2 times the standard deviation.

This results in the set of dwell positions and times for that particular catheter number. The set of dwell positions and times are shown in Figure 5.6.

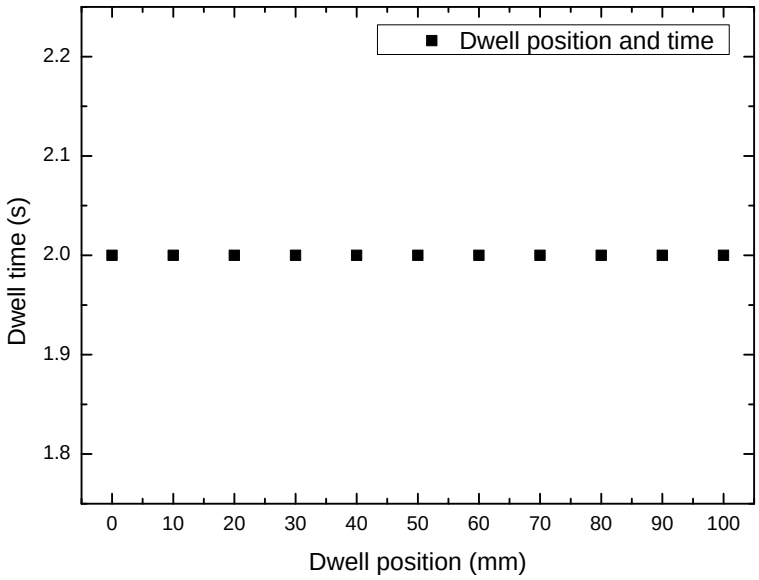

Figure 5.6: Theoretical dwell position and time – 10 mm step size, 2 second dwell.

As this is a theoretical calculation with no variation in the source position determination, there has been no uncertainty in the dwell position. This would not be the case in real measurements.

5.3 Discussion and conclusion

In this chapter, a description of the source tracking algorithm and dwell position and time determination has been presented. The source tracking algorithm shows that by taking the response of three or more detectors, it is feasible to calculate the solution of the source position by using an iterative method for a single measurement frame. By aggregating multiple frames, the dwell positions and times can be determined by the dwell position-time histogram.

This method of source tracking relies an accurate determination of the SDD from the detectors response. The fitting equation used was found to have an average absolute difference of 0.82 $\pm$ 1.10 mm (2 S.D) over the range of 7 – 150 mm, representing a less than 2 mm difference in the SDD. As multiple detectors are used in the source position determination procedure, this should minimise the effect of this difference. The method also assumes that the set of MP detectors are very similar, in terms of geometry, region of charge collection, energy response and angular dependence. This assumption is reasonable due to the well developed fabrication method of the silicon detectors.

There are limitations to this method when individual MP detector responses have a very low signal-to-noise ratio, resulting in a high variation in response. This is compensated for in the method by only considering detector responses with a large enough signal, excluding the detectors with low responses. However, when the HDR source is above or close to the MP field of view (FOV), there are fewer detectors with higher responses, potentially resulting in an incorrect determination of the source coordinate. This FOV effect is investigated in further detail the next chapter.

The MPh has been designed to have each catheter x and y coordinate fixed; the movement of the source is only along the y-coordinate. This simplifies the use of the dwell position-time histogram method to only account for the y-coordinate, instead of in three-dimensions. The methods presented in this chapter have been implemented into Brachy*Pix* software for post-processing analysis, and are verified experimentally in the following chapter.

Chapter 6

Experimental verification of source tracking and dwell position determination

The previous chapter outlined the mathematical description of the MPh source localisation method, and methods for determining dwell positions and times. The work presented in this chapter details the experimental verification of these methods[3]. A single catheter plan was measured by the MPh with all dwell positions and times determined. The calculated dwell positions were then compared to exposed EBT3 film, placed above the MP detector during delivery. The minimum resolvable interdwell distance and dwell time were also assessed.

All plans were delivered using the Nucletron Flexitron® HDR afterloader (Nucletron, an Elekta company, Elekta AB, Stockholm, Sweden) at the St George Cancer Care

[3] Parts of this chapter have been published in Medical Physics:
A. Espinoza, M. Petasecca, I. Fuduli, A. Howie, J. Bucci, S. Corde, M. Jackson, M. L. F. Lerch, and A. B. Rosenfeld, "The evaluation of a 2D diode array in "magic phantom" for use in high dose rate brachytherapy pretreatment quality assurance," Medical Physics, vol. 42, no. 2, pp. 663-673, 2015

Centre, Sydney.

6.1 Source tracking and dwell position and time determination

The source tracking method determines the source position within 3D for each measurement frame. A basic plan was created to move the source inside a single catheter, which was then tracked by the MPh detector. The treatment plan was then loaded into the software for a direct comparison of the determined motion.

Methods

Validation of the source tracking method was performed by programming the afterloader to drive the HDR source, at 5 mm step sizes and with a dwell time of 2 seconds, towards the end of the catheter. The catheter was placed inside the MPh and positioned directly above the middle column of the MP detectors ($x = 50$ mm) with the source stepping across the y-coordinate. The MP was at a SDD of 6 mm below the catheter's plane. The source position was determined for each measurement frame, using the developed methods, and were compared to the treatment plan. This was then repeated for all 20 catheter positions inside of the MPh to determine any potential problems with the tracking procedure.

Results

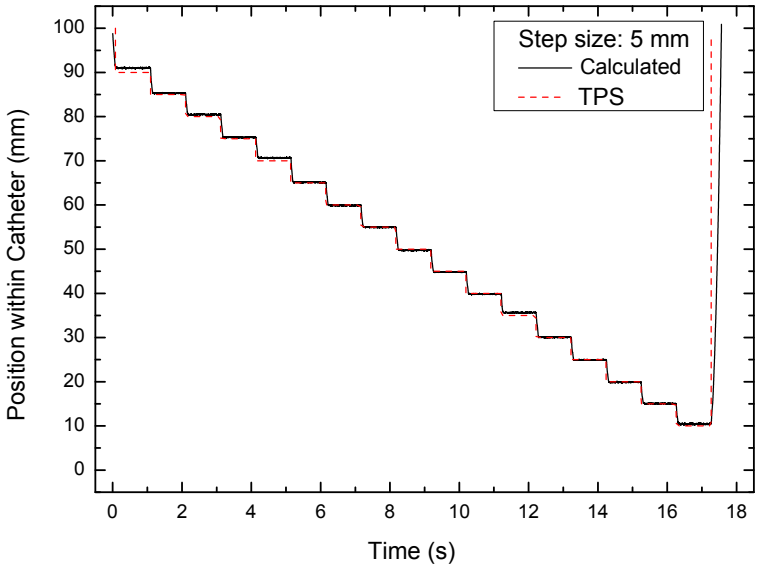

Figure 6.1: Tracking the HDR source inside a single catheter.

Good agreement was found between the positions and dwell times determined by the HDR source tracking algorithm, and those programmed by Nucletron ONCENTRA® TPS, as seen in Figure 6.1. It was found that the source travels from the afterloader, and dwells at the furthest dwell position away from the catheter tip, and then moved progressively closer. It was possible to determine the motion of the source as it moves from dwell position to dwell position, as a timing resolution of 1 ms was used. The transit motion is seen in Figure 6.2, where both graph scales have been adjusted to show 4 dwell positions. As stated in Chapter 2, the TPS neglects the time needed to move the source from dwell position to dwell position.

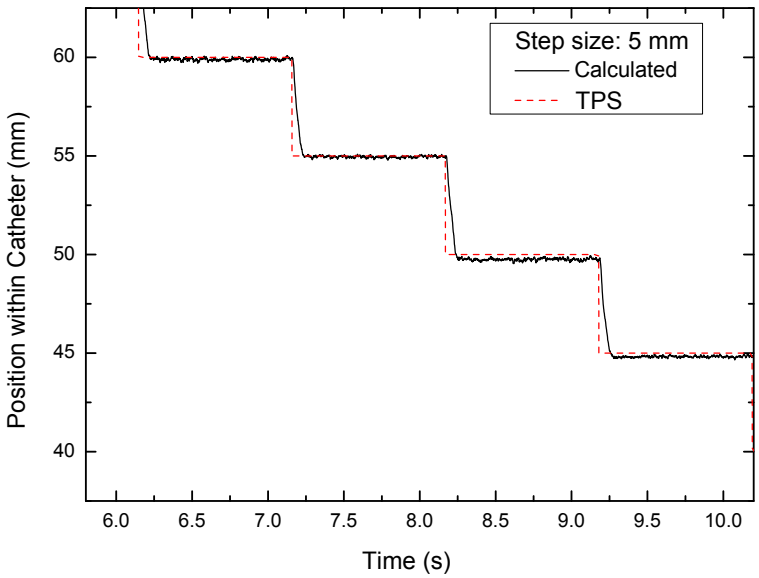

Figure 6.2: Zoom of the tracking of the HDR source.

A position frequency histogram was generated from the source tracking calculations for the single catheter. Each histogram had a bin width of 0.1 mm; the counts of source positions is related to the electronic sampling frequency, with each count equal to 1 ms time at that position. Figure 6.3 shows the histogram for the 5 mm step size plan. Each dwell point was found to be a narrow peak, where the centre position of each peak was equal to the dwell position. The number of counts, converted to time, under each peak is equal to the total dwell time for that dwell position.

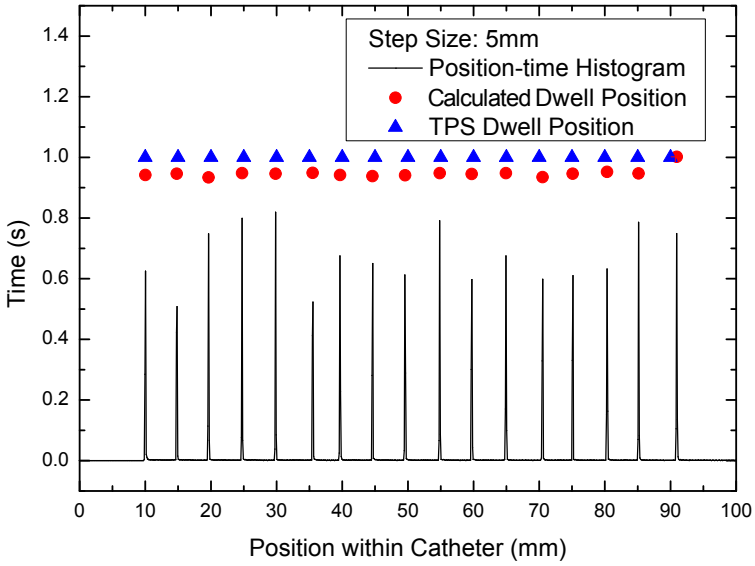

Figure 6.3: Measured dwell position-time histogram for the single catheter plan.

It was found that only the dwell position at 90 mm was calculated to have the correct dwell time, stated by the TPS plan. Each dwell position was planned to have the same dwell time and a constant decrease was observed on the remaining dwell positions. The difference between the planned and calculated dwell times was found to be be 56.45 $\pm$ 13 ms (2 S.D.), and is most likely due to the Nucletron Flexitron® HDR afterloader compensating for the source transit time. It is expected that the this difference would be larger than 10 ms, which is derived assuming that the source moves at the maximum speed of 50 cm/s. Based upon this measured difference, the average source speed across 5 mm for this afterloader is estimated to be 8.86 $\pm$ 1.02 cm/s (2 S.D).

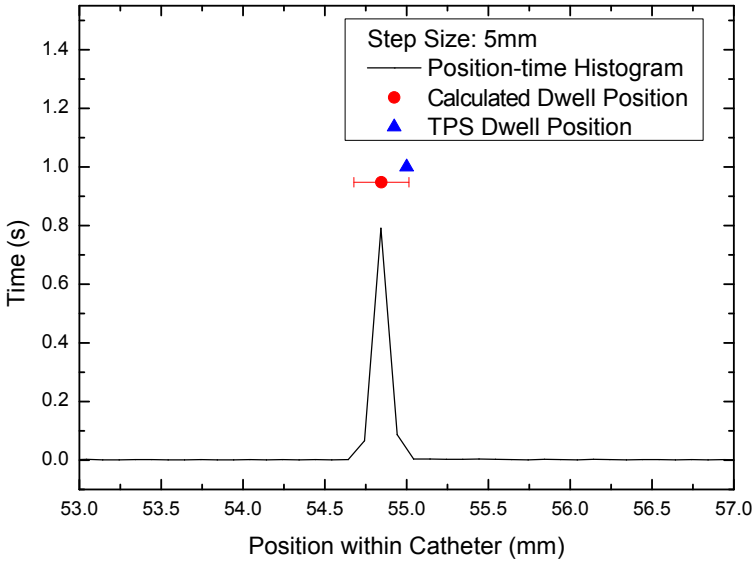

Figure 6.4: Expanded view of the tracking of the HDR source.

By inspecting a single dwell position on the histogram (Figure 6.4), the uncertainty of the calculated dwell position can be seen to cover the peak. The TPS position was found to be within the error of the calculated dwell position, determined from Equation 5.12.

By analysing the results from all 20 catheters, it was found that there existed a difference between the measured dwell position and planned dwell positions, when the source was dwelling close to the edge of the MP FOV. Figure 6.5 a) shows the difference between the measured and planned positions, and b) shows a close up view around the edge of the MP FOV.

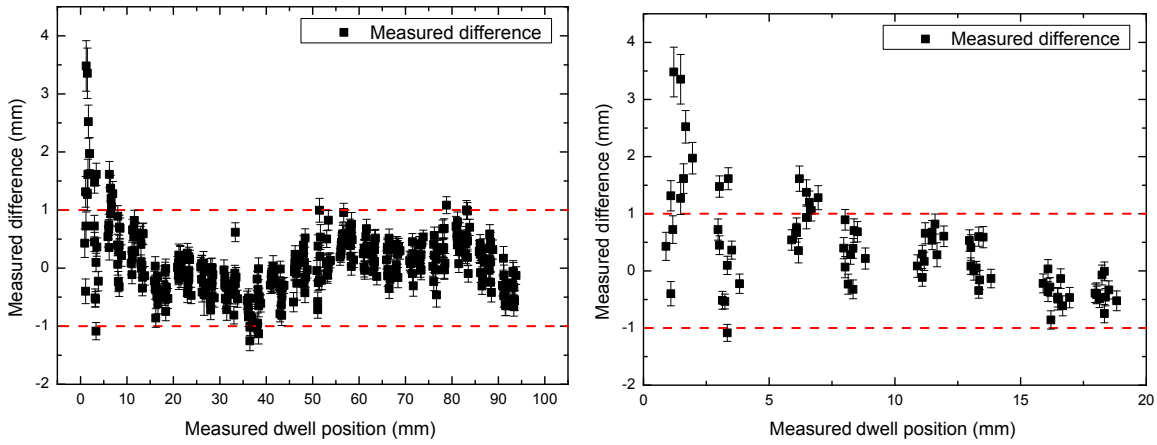

(a) Measured dwell positions over entire range. (b) Measured dwell positions over 0 – 20 mm.

Figure 6.5: Difference between the measured dwell position and planned.

It is clear that when the source is dwelling at positions between 0 - 10 mm the difference becomes larger than ± 1 mm, and up to 3.5 ± 0.5 mm. The average difference across the entire range was found to be 0.08 ± 1.12 mm (2 S.D), but when considering only the range of 10 – 90 mm, the average difference was reduced to 0 ± 0.84 mm (2 S.D) with a lower variation.

6.2 EBT3 film comparison

The position of the source is related to the tip of each catheter, which is registered in the frame of the MPh with coordinate system origin based on a left corner detector. A position calibration test, relative to the MPh origin, was performed by driving the source to multiple positions in a single catheter, and simultaneously measuring with the MP in the MPh and exposing EBT3.

Methods

Two pieces of EBT3 film were registered to the MPh, by fixing them rigidly between the MP and the top catheter plane. The MPh was CT scanned with a single piece of EBT3 film and the MP detector inside the MPh. The catheters were inserted in the MPh prior to the scan, with metal markers placed inside each catheter tip. The CT scan was used to confirm the alignment of the EBT3 film against the MP and to plan the delivery of 6 dwell points separated by 20 mm within the catheter.

The plan was delivered using the Nucletron Flexitron® HDR afterloader. The irradiation of a second piece of film by the HDR source resulted in a circular distribution of the change in colour of the film at each dwell point. The centre of mass of each source image on the film and the dwell positions calculated by the software were compared with the planned dwell positions.

Results

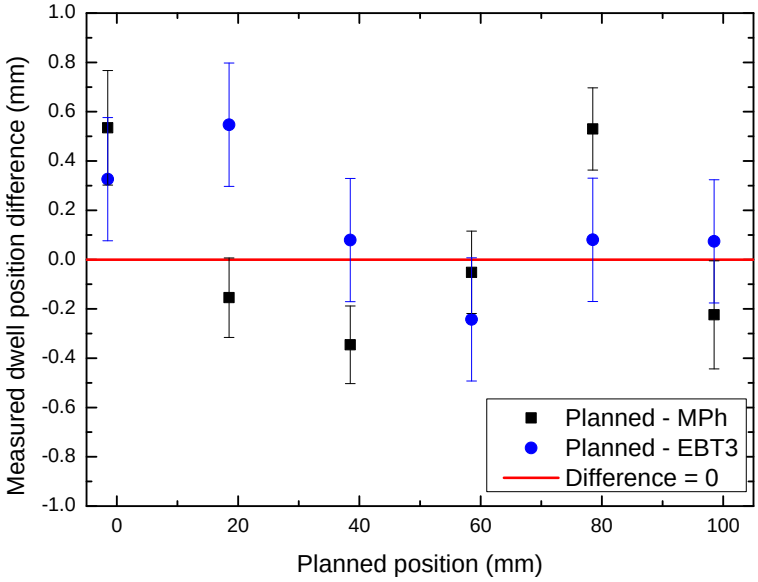

Figure 6.6: The difference between the calculated and planned dwell positions for the MPh calculation and EBT3 film for single catheter measurement.

Figure 6.6 shows the difference along the catheter length between the calculated and planned dwell positions for the position calibration test. The source was driven through a single catheter towards the tip, and the EBT3 film was irradiated while the MPh acquired. Six dwell positions were identified by both the software and from the film analysis, and all differences were less than 0.8 mm. An uncertainty of $\pm$ 0.25 mm (Type B) was estimated due to the coordinate registration of the film to the MPh reference frame.

6.3 Determination of the minimum measurable interdwell distance and dwell time

The Nucletron Flexitron® HDR afterloader can be programmed to drive the HDR source to dwell positions with varying interdwell distances (the distance between two dwell positions) and dwell times, with a minimum of 1 mm and 0.1 s, respectively. To be feasible for plan verification, the MPh system must be able to determine dwell positions and times accurately, over this range of step sizes and dwell times.

Methods

To assess the dwell position resolution of the system, the afterloader was programmed to move the HDR source through a single catheter, with progressively reduced step sizes down to 1 mm. Each dwell position had a programmed dwell time of 3 s and was measured using the MPh system. The transit time of the source from one dwell position to the next was also calculated.

To assess the dwell time resolution of the system, the HDR afterloader was programmed to drive the source to 3 dwell positions within a single catheter for the same amount of time. The measurement was repeated for a range of dwell times from 10 s down to 0.1 s.

Results

As seen in Table 6.1, the dwell positions were determined by the MP, and the system was capable of resolving the dwell positions separated by 1 mm. The last two dwell positions were close to the catheter tip and the edge of the FOV of the MP, and used

fewer detectors to calculate the source position. As the tracking algorithm is based upon the agreement of the detector with the largest response and its neighbours, reduced numbers of detectors can result in a shift in true position.

Each prescribed dwell time, apart from the first dwell position calculated, was found to be reduced from the planned 3 s. This reduction in dwell time agreed with the calculated time taken to move the source to that position and was found to be proportional to the interdwell distance.

Planned Position (mm)	Measured position (mm)	Measured dwell time (s) (± 0.001 s)	Measured transit time (s) (± 0.001 s)
83.6	83.49 ± 0.14	3.015	-
53.6	53.82 ± 0.12	2.792	0.219
33.6	34.23 ± 0.14	2.849	0.172
23.6	23.95 ± 0.18	2.919	0.109
18.6	18.27 ± 0.16	2.946	0.066
14.6	15.06 ± 0.16	2.987	0.040
11.6	11.54 ± 0.16	2.976	0.054
9.6	8.72 ± 0.18	2.989	0.041
8.6	7.35 ± 0.16	2.991	0.027

Table 6.1: The comparison of the planned position in an HDR catheter and the position and time calculated using the MPh.

The minimum measurable dwell time for the MPh system was evaluated by using three dwell positions, at 13.6 mm, 18.6 mm and 28.6 mm from the catheter tip, and varying the planned times. Again, each position was set to have the same dwell time, but varied when calculated, except for Position 1, which was the first the source was

driven to.

In Table 6.2 it can be observed that the minimum dwell time that was calculated was 0.067 ± 0.001 s. For planned dwell times of 0.1 s, Position 2 was expected to have a time of 0.01 - 0.02 s, but could not be detected in the position frequency histogram.

Planned dwell time (s) TPS	Measured dwell time (s) (±0.001 s) Position 1 (28.6 mm)	Position 2 (18.6 mm)	Position 3 (13.6 mm)
10	10.012	9.914	9.955
5	5.015	4.908	4.951
3	3.014	2.898	2.955
2	2.014	1.911	1.951
1	1.013	0.916	0.957
0.5	0.512	0.414	0.458
0.3	0.315	0.213	0.256
0.2	0.212	0.109	0.155
0.1	0.107	Unable to determine	0.067

Table 6.2: Determination of the minimum measurable dwell time.

6.4 Discussion and conclusion

The combination of the source tracking algorithm and the high timing resolution of the AFE DAQ system, made it possible to determine the source position at 1 ms intervals. This allowed for the accurate measurement of the source motion while in

transit and for dwell time determinations to overcome the programmable limitations of the afterloader system.

The MPh system has shown that it can be used to resolve dwell positions spaced apart by 1 mm or larger, but the verification of the accuracy of all dwell times set by the TPS is impossible, as the afterloader itself was found to always modify the actual dwelling time. A relationship exists between the absolute dwell time reduction and the interdwell distance, which is noticeable for all dwell times. This relationship will be explored in further detail in the subsequent chapter. It has, however, been demonstrated that dwell positions programmed to 0.1 s were able to be distinguished, when there was no effect of the afterloader compensating for the transit time. With further development of Brachy*Pix* and integration with the TPS, it would be possible to evaluate the clinical significance of the modified dwell times on the patients plan, allowing for modifications to the treatment plan to achieve clinical goals when necessary.

It was observed that there was a shift in dwell positions determination when the source was close to the edges of the MPh FOV. This shift was found to be as a large as 3.5 $\pm$ 0.5 mm when the source was at 0 mm, with the effect being minimised as the source was between 10 – 90 mm. When ignoring the dwell position differences between 0 – 10 mm, the average difference was between $\pm$ 0.84 mm. This effect is most likely due to the MP detectors not surrounding the HDR source, causing the algorithm to incorrectly determine the source position.

For accurate source dwell position calculations, the TPS plan should be configured to set the last dwell points at least 5 – 10 mm away from the edge of the MPh FOV. While there is a reduction in usable catheter length for this particular design of the MPh, it will be possible to measure the dwell position accurately within a total range

of 80 – 90 mm.

Chapter 7

The source motion and transit dose components

Previous evaluations of the average transit speed using direct measurements have varied between 5.4 to 35 cm/s for a range of step sizes, for a wide range of measurement techniques [64–68]. The average source speed using the single element of the MP detector and the X-Tream electronics system have previously been reported by the author [16]. By sampling the diode response with high temporal resolution of 1 MHz, an estimation of the transit times and average speeds were made.

This chapter presents a more robust method for determining the instantaneous source speed, as opposed to the average, based upon the timing resolution of the AFE DAQ system and the source tracking method. The HDR source motion was evaluated as the source entered the catheter, stepped between dwell positions, and then returned back to the afterloader. The transit dose components were determined for the MP plane by integrating the dose rates calculated using the TG-43U1 protocol, based upon the discrete source position.

Measurements were performed using the Nucletron microSelectron® mHDR-v.2. afterloader (Nucletron, an Elekta company, Elekta AB, Stockholm, Sweden) at the Prince of Wales Hospital, Sydney.

7.1 The HDR source in motion

Dwell times and speed profiles were measured for a Nucletron microSelectron® mHDR-v.2. afterloader using the MP. Due to the fast acquisition sampling frequency of the AFE DAQ system, of up to 10 kHz, it was possible to measure the response of the MP detector while the source was in transit. The measured responses were then used to determine the source position with high temporal resolution.

Methods

A single catheter delivery was programmed in the afterloader console, featuring two dwell positions with varied interdwell distances. The HDR source was set to step to the first dwell position in the catheter, and remain for 2 seconds. The source was then set to move to the subsequent position, where it remains for an additional 2 seconds, before returning to the afterloader. The step size was varied from 2.5 to 100 mm and a sampling frequency of 4 kHz was used, giving a timing resolution of 250 μs per measurement.

Results

The source tracking for the 50 mm step size is seen in Figure 7.1 a). By inspecting the tracking data during the transit component of the motion, in Figure 7.1 b), a distinct

non-constant motion of the source can be observed.

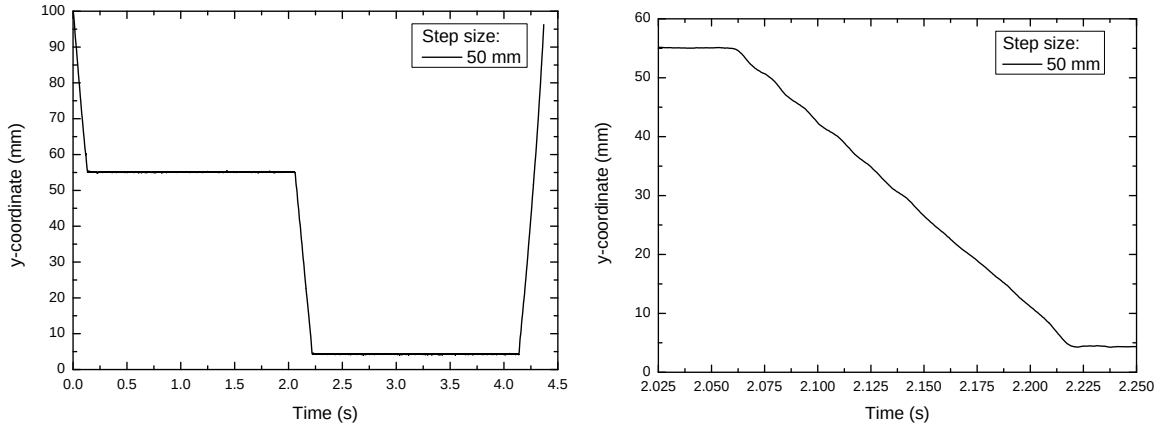

(a) Full motion. (b) Transit component.

Figure 7.1: The source tracking for a 50 mm step size.

By taking the derivative of the source motion along the y-coordinate, with respect to time, it was possible to obtain the instantaneous speed of the HDR source. Figure 7.2 shows this instantaneous speed for the 50 mm step size. This calculation shows that the HDR source increased in speed, and approached the 50 cm/s stated maximum, but then slowed down to ∼25 cm/s. The speed was found to oscillate between the 25 – 50 cm/s range.

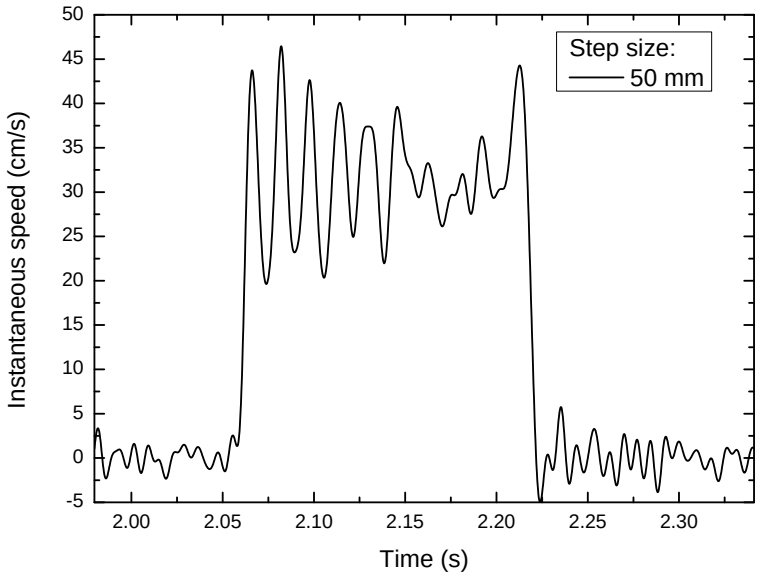

Figure 7.2: The 50 mm step size instantaneous speed.

By overlaying the instantaneous speeds for multiple step sizes, the frequency of the oscillation is seen to be constant. The frequency was determined to be approximately 63.11±9.06 Hz (2 S.D).

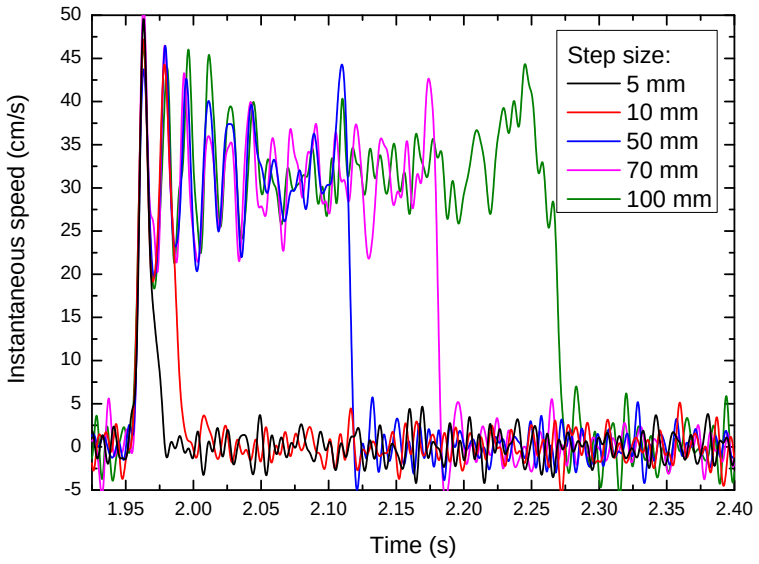

Figure 7.3: The instantaneous speeds for multiple step sizes.

The calculation of the average speed for the measured dwell points are shown in Figure 7.4, alongside published values. Average speeds found within the literature have a large variation, showing the challenging nature of this characterisation. Measurements previously published by the author, Espinoza et al. [16], were performed using a single element of the MP, the Epitaxial diode, and were connected to a single channel data acquisition system with 1 μs sampling frequency, named the X-Tream electronics system. Both experiments were to assess the average speed of the Nucletron microSelectron® mHDR-v.2. afterloader, with the MPh measurements occurring approximately two years after the X-Tream.

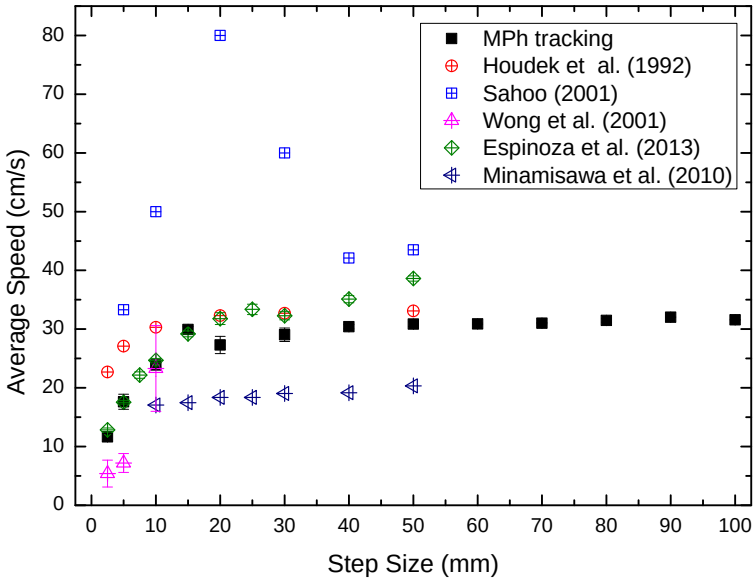

Figure 7.4: The average speed for multiple step sizes compared to the literature.

The X-Tream system sampled the charge generated within the diode at 1 MHz frequency, but these results could only be used to obtain the average speed of the source based on the changes in charge over time. The calculation of the average speed taken from the MPh are in good agreement with those previously taken with X-Tream. Although the discrepancy of absolute value is related to the specific afterloader, this direct measurement technique shows a similar trend of the source velocity with the

step size.

7.2 Transit dose calculations

Brachy*Pix* has an built-in dose calculator based upon the TG-43U1 protocol. By using the measured source position sampled at 4 kHz, the transit dose at certain points could be calculated. Assuming the source motion is discrete at this timing resolution, the dose delivered was the calculated dose rate multiplied by the timing resolution. The 50 mm source tracking calculation was used to generate integral dose maps to compare the effect of the transit dose along the MP plane.

Methods

Two-dimensional 10×10 cm^2 dose maps along the MP plane were generated by calculating the dose to points at 0.5 mm intervals. A source activity of 32 $mGy.m^2.h^{-1}$ was used in the dose rate calculations. Individual integral dose maps were created for the components of the HDR source motion. These include the total dwelling dose based upon the two dwell positions, the entrance and exit dose, and that delivered as the source steps from one dwell position to the next.

Results

Figures 7.5 a-e) show the calculated integral dose maps. The transit motion of the source delivered a maximum of 0.9 cGy for the source activity of 32 $mGy.m^2.h^{-1}$ to the MP plane.

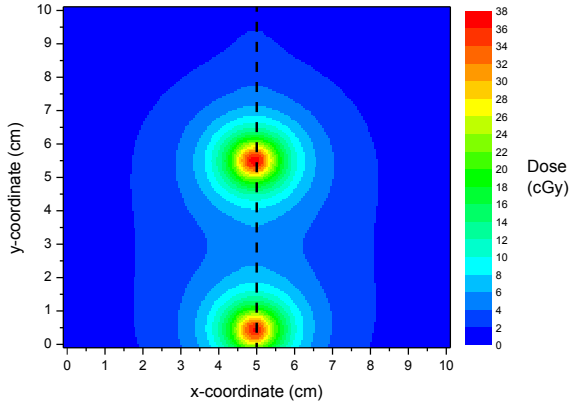

(a) Total dose with central line.

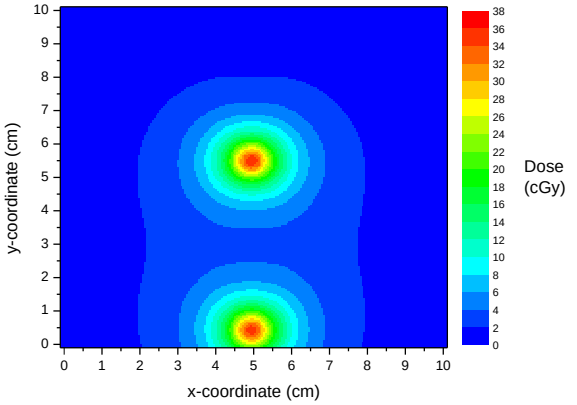

(b) Dwell dose only.

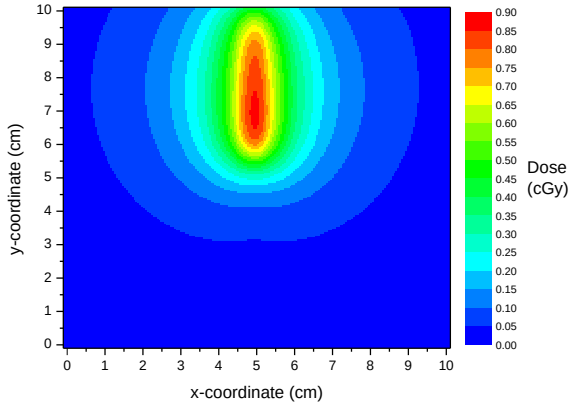

(c) Entrance dose.

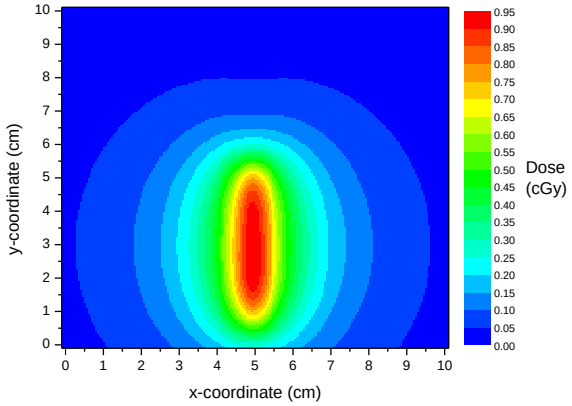

(d) Stepping dose.

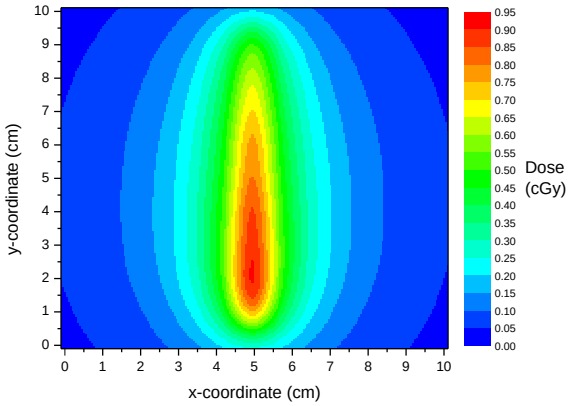

(e) Exit dose.

Figure 7.5: Calculated integral dose maps using Brachy*Pix*.

A line profile was taken along the centre vertical axis of all the calculated dose maps. Figure 7.6 shows the total dose and the individual contributions for the 50 mm step size. It is possible to see that overall, each movement of the source delivers a relatively low amount of dose, when compared to the total dwelling dose.

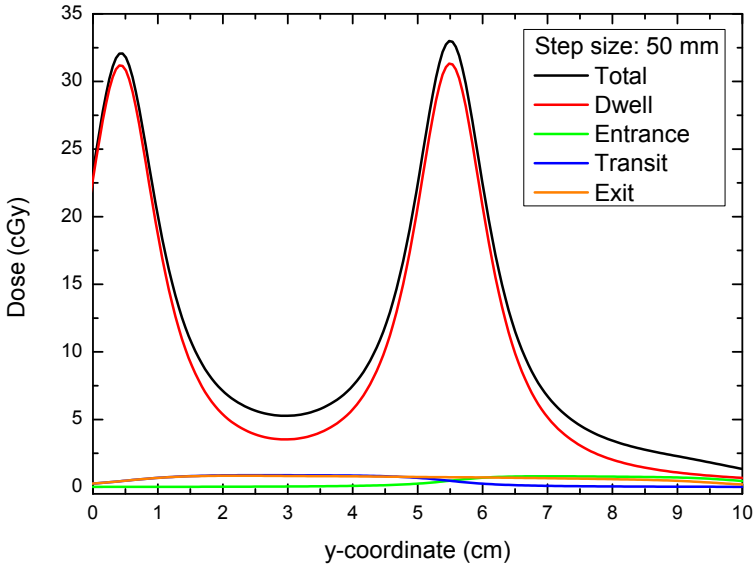

Figure 7.6: The dose profile calculated on the MP detector plane.

The percentage of transit dose to the total dose was determined for the line profile and graphed in Figure 7.7. As to be expected, there is a large contribution of transit dose at positions not in the immediate region of the dwell position, as the dwell dose only would be low for these points. A greater than 50% contribution of transit dose can be seen at the position where the source was entering and leaving the catheter.

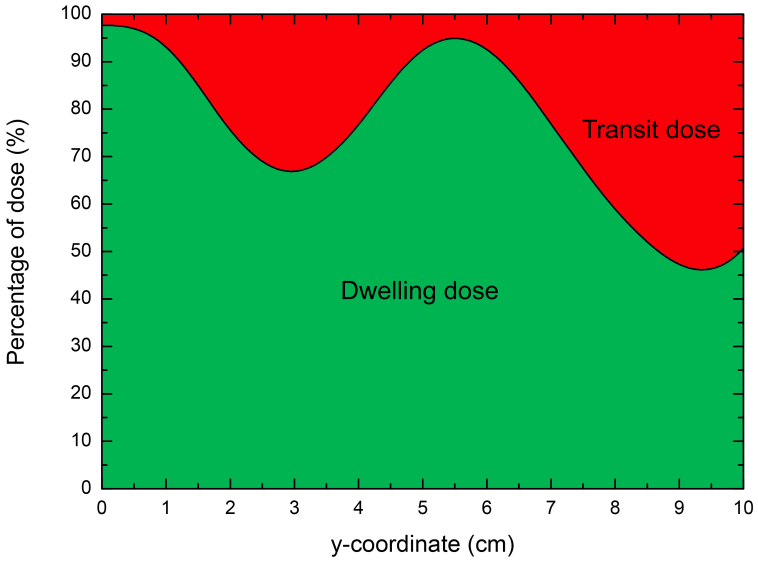

Figure 7.7: The percentage of the dwell dose relative to the total dose.

7.3 Discussion and conclusion

The MP response was sampled at high frequency and was used to determine the motion of the HDR source as it moved from dwell position to next. The tracking information derived has shown that the instantaneous velocity of the source is not 50 cm/s as stated by Nucletron, but increases and decreases over time.

This result was also obtained by Fonseca et al. [67] by using a high speed video camera to track the HDR source motion. On discussion with Nucletron, it has been hypothesised that the tension within the source cable causes it to act like a spring as it moves, while there is also an effect of the friction and slipping of the source along the transfer tube and catheter inner wall, that contribute to this oscillation in source speed.

The position of the source in transit was determined with a high timing resolution and

used to determine the transit dose contribution, as opposed to assuming a constant acceleration or source speed like methods found in the literature. Using the TG-43U1 protocol to determine the dose at a particular point is computationally faster than Monte Carlo simulations, but is less accurate due to its assumptions. For this study, dose was only calculated along the MP plane, but it could be possible to estimate the total dose to be received by critical organs by taking into account the patient anatomy and calculating the transit dose based off the measured source motion.

Chapter 8

Pretreatment plan verification

The preceding chapters described and evaluated a method to determine the HDR brachytherapy source position and calculate the dwell position and timing pattern. The focus of this chapter is the assessment of the execution of treatment plans by the HDR afterloader. Two treatment plans, Plan – 1 and Plan – 2, were generated for this verification test and were delivered to the MPh[4]. Plan – 1 was created to be a non-specific treatment scenario and was developed so that the afterloader would drive the source through each of 20 catheters connected to the MPh, and to dwell at various positions and times.

This plan was then modified by a Medical Physicist, producing Plan – 2, to simulate possible errors in delivery by the remote afterloader. These modifications were not disclosed to the author until after the analysis had been performed to judge the performance of the error detection using a new metric named the position-time gamma index.

[4] The majority of this chapter has been published in Medical Physics:
A. Espinoza, M. Petasecca, I. Fuduli, A. Howie, J. Bucci, S. Corde, M. Jackson, M. L. F. Lerch, and A. B. Rosenfeld, "The evaluation of a 2D diode array in "magic phantom" for use in high dose rate brachytherapy pretreatment quality assurance," Medical Physics, vol. 42, no. 2, pp. 663-673, 2015

All plans were delivered using the Nucletron Flexitron® HDR afterloader (Nucletron, an Elekta company, Elekta AB, Stockholm, Sweden) at the St George Cancer Care Centre, Sydney.

8.1 The position-time gamma index

To quantitatively compare the source position and dwell times in the catheter to the treatment plan, a new metric was introduced based upon the dose-position gamma index. The use of the 2D gamma index in quality assurance was first described by Low et al. [96] and was used to quantitatively compare 2D intensity modulated dose distributions for external beam radiation therapy. It compares the measured and calculated distributions by evaluating, point-by-point, the dose difference and the distance to agreement, the former being sensitive to the homogeneous part of the irradiated area and the latter to high dose gradients. A pass-fail result, illustrated by a gamma value lower or higher than 1 respectively, is found depending on an acceptable pre-defined criteria, typically 3% dose difference and 3 mm distance to agreement.

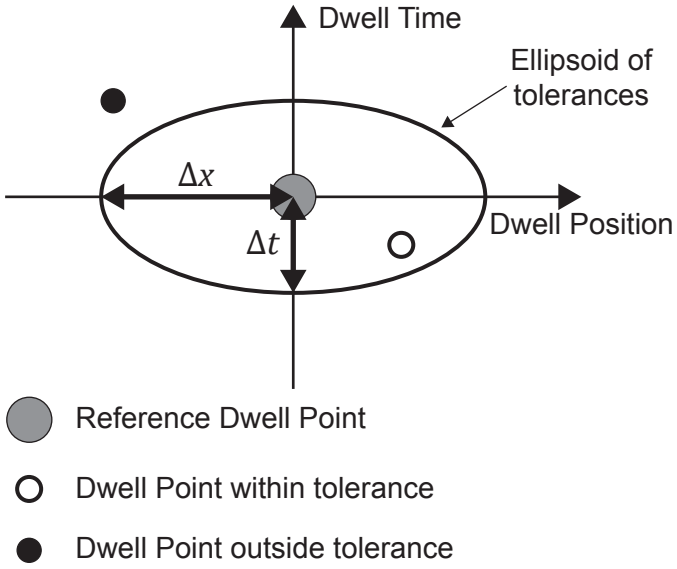

Figure 8.1: Geometric representation of the position-time criteria.

Adopting the formalization of this method and applying it to HDR brachytherapy, it is possible to compare the measured treatment to the plan by evaluating the calculated source dwell and timing patterns. By using an acceptable distance-to-agreement and time-to-agreement criteria values, a pass-fail grade (pass if gamma value is equal to or less than 1) is determined for all calculated dwell positions and times. A graphical representation of the position-time criteria is seen in Figure 8.1.

Symbol	Equation	Description
$A^n(x_{iA}, t_{iA})$	N/A	The i-th dwell position, x_{iA}, and dwell time, t_{iA}, of set A in catheter n.
$B^n(x_{jB}, t_{jB})$	N/A	The j-th dwell position, x_{jB}, and dwell time, t_{jB}, of set B in catheter n.
Δx	N/A	Distance-to-agreement criterion (DTA).
Δt	N/A	Time-to-agreement criterion (TTA).
$\delta_{ij}^n(x_{iA}, x_{jB})$	$\delta_{ij}^n(x_{iA}, x_{jB}) = \lvert x_{iA} - x_{jB} \rvert$	δ_{ij}^n is the spatial difference between the i-th dwell position of set A and the j-th dwell position of set B for catheter n.
$\tau_{ij}^n(t_{iA}, t_{jB})$	$\tau_{ij}^n(t_{iA}, t_{jB}) = \lvert t_{iA} - t_{jB} \rvert$	τ_{ij}^n is the difference between the i-th dwell time of set A and the j-th dwell time of set B for catheter n
$\Gamma_{ij}^n(\delta_{ij}^n, \tau_{ij}^n)$	$\Gamma_{ij}^n(\delta_{ij}^n, \tau_{ij}^n) = \sqrt{\left(\frac{\delta_{ij}^n(x_{iA}, x_{jB})}{\Delta x}\right)^2 + \left(\frac{\tau_{ij}^n(t_{iA}, t_{jB})}{\Delta t}\right)^2}$	Generalized Γ index computed for all dwell positions and times of set A and set B for catheter n.
$\gamma^n(x_{iA})$	$\gamma^n(x_{iA}) = \min\{\Gamma_{ij}^n(\delta_{ij}^n, \tau_{ij}^n)\} \forall \{B^n(x_{jB}, t_{jB})\}$	The γ index - the minimum generalized Γ for the set B, $B^n(x_{jB}, t_{jB})$ dwell positions and dwell times in catheter n.

Table 8.1: Definitions of the HDR position-time gamma index.

The formalization of this method is found in Table 8.1. Two sets, A and B, represent the calculated and TPS dwell position timing pattern in catheter n. The gamma index compares all the dwell positions in set B against those in set A. The gamma index was calculated twice to first compare the treatment calculated (set B) by the MPh against the treatment plan (set A), and then for the treatment plan (set B) against the calculated (set A). This increases the robustness of the method, taking into account cases when sets A and B have unequal numbers of dwell positions due to introduced or missed dwell positions by the afterloader.

The uncertainty in the gamma index value is calculated based upon the propagation of the error of the dwell position determination and the estimated uncertainty in timing,

$$\sigma_{\Gamma^n_{ij}} = \sqrt{\left(\frac{\delta^n_{ij}}{\Gamma^n_{ij}\Delta x}\right)^2 \sigma^2_{x_{iA}} + \left(\frac{\tau^n_{ij}}{\Gamma^n_{ij}\Delta t}\right)^2 \sigma^2_{t_{iA}}} \tag{8.1}$$

where $\sigma_{\Gamma^n_{ij}}$ is the uncertainty in the gamma index and $\sigma_{x_{iA}}$ and $\sigma_{t_{iA}}$ are the uncertainties in the dwell position and time calculation. The uncertainty in dwell position is derived from the position-time histogram described in Chapters 5 and 6. The uncertainty in dwell time is based on the temporal resolution of the measurement, typically 1 ms.

8.2 Verification of the unmodified plan

A non-specific treatment plan, Plan –1, was created using Nucletron ONCENTRA® TPS , delivered using the Nucletron Flexitron® HDR afterloader and tested with the MPh. When comparing the treatment plan against the MPh determined dwell positions and times, it is expected that no errors in afterloader delivery are calculated, and that the entire measure should pass the position-time gamma analysis.

Methods

The MPh was imaged using the Philips Brilliance CT - Big Bore scanner at the St George Cancer Care Centre, Sydney, and the images imported into the Nucletron ONCENTRA® TPS. An Axial Helix protocol was used for the CT scan, with a slice thickness of 1 mm, increment of 0.5 mm. The CT scanner was set to 120 kV_p and 250 mAs to obtain a high image signal to noise ratio. Each small MP detector element could be seen on the 3D image reconstruction, and each detector was selected as a point for dose calculations in the TPS. The source was then programmed to dwell at various positions and times inside each of the 20 catheters to create a non-specific treatment plan, Plan –1, with a maximum dose of 600 cGy to a single detector element. Each catheter had varying dwell positions and times arranged in the plan in an unsystematic fashion.

Plan –1 was delivered using the Nucletron Flexitron® HDR afterloader and measured by the MPh. Each plan was exported as a DICOM file, preserving the source dwell and timing information for each catheter and the calculated absorbed dose at each detector position on the MP. The DICOM file was subsequently read by the custom software suite to compare the calculated dwell positions and times against the plan using the position-time gamma analysis.

Results

Figure 8.2 shows the source tracking calculated position and dwelling time in a position in the catheter verses time for the first catheter, determined by the algorithm described in detail in previous study. The TPS plan for this catheter is graphed for comparison and shows good agreement for positions larger than 5 mm from the coordinate origin

based on the MPh corner detector. While the TPS does not take into account the motion of the source in transit between dwell points, it is possible to measure this due to the high speed of the MPh readout system, and is the subject of Chapter 7.

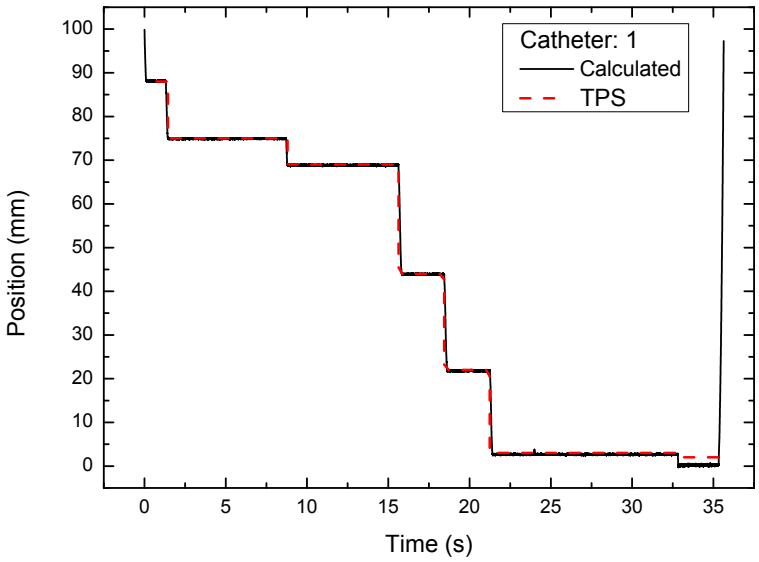

Figure 8.2: Source tracking measurement and TPS plan for Catheter 1. The position calculated was relative to the MPh coordinate system.

The calculated and TPS planned dwell position-time pattern for catheter 1 are presented in Fig 8.3. Uncertainties in the dwell position determination were typically of the order of 0.2 mm (2 S.D) and are unable to be seen on this graph. Good agreement between these dwell patterns were seen for the majority of points, except for those close to 0 mm, due to the edge of FOV effect.

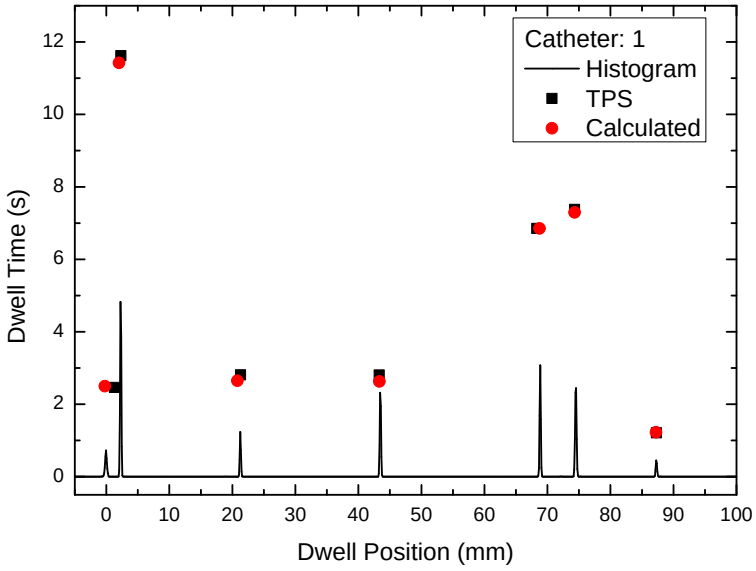

Figure 8.3: Dwell position frequency histogram and comparison of dwell position timing pattern for Catheter 1 with the TPS plan.

The average difference between the calculated dwell position and the TPS plan for 86 dwell positions was 0 ± 0.63 mm (2 S.D), taking into account the larger differences due to the edge FOV effect. When not taking this into account, the average difference was found to be 0 ± 1.30 mm (2 S.D). Seen in Figure 8.4, the dwell time differences were found to be less than 0.25 s, and the majority showed that the MPh calculated less than the expected planned dwell times. It is expected that due to the highly accurate

internal clock of the electronics used, the error in timing is approximately 1 ns.

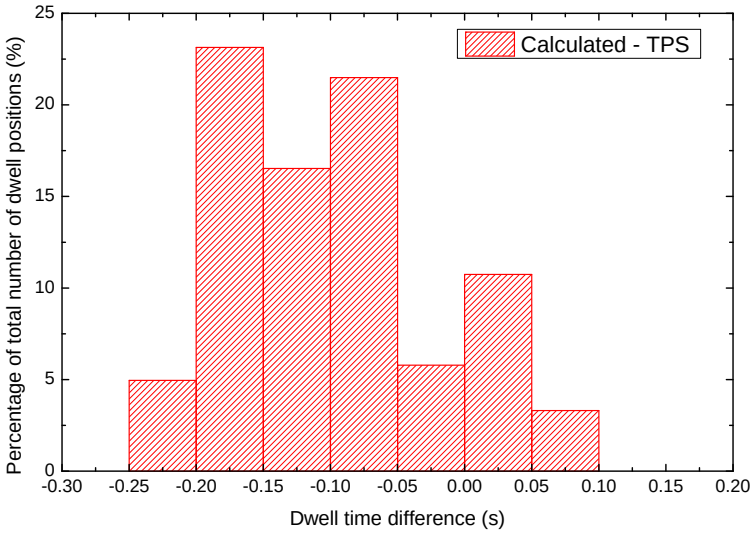

Figure 8.4: Histogram showing the difference in dwell times of the Measured and TPS.

This difference in dwell time is most likely due to a feature of the Nucletron Flexitron® HDR afterloader that reduces dwell times to compensate for additional dose delivered while the source is in transit between successive dwell points. In Figure 8.5, the differences in dwell times are plotted against the interdwell distances, showing that the difference in dwell time for the subsequent position is proportional to the distance the source had to travel. An interdwell distance of 0 mm represents the first dwell position in the catheter, where it is expected to be no change in dwell time.

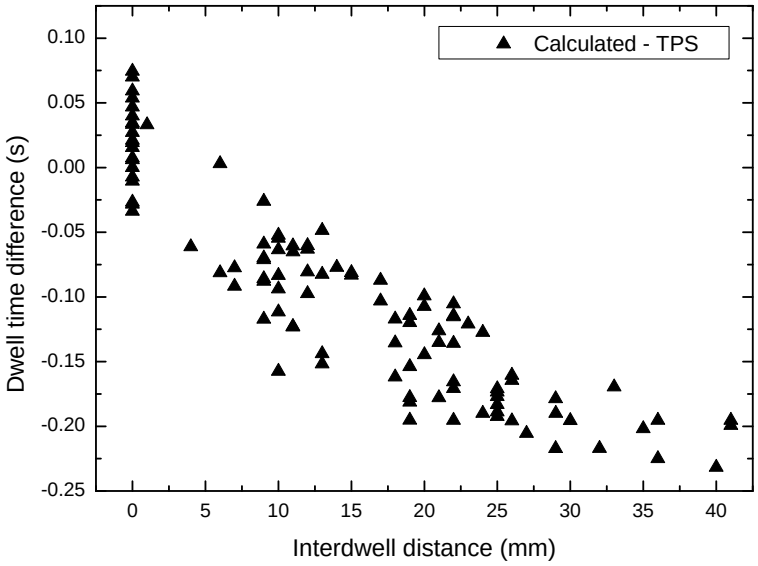

Figure 8.5: Difference between calculated and planned dwell times against interdwell distance.

According to the Nucletron ONCENTRA® TPS MasterPlan Physics and Algorithms manual [97], it is assumed that this afterloader drives the source at a speed of 50 cm/s and for an interdwell distance of 50 mm the dwell time is reduced by a maximum of 0.1 s. It is noted that this feature may not be seen in some afterloaders. The calculated dwell time differences are larger than expected, but values of the average source speed varied from 12.5 - 37.5 cm/s were previously reported by the author [16]. Although a different afterloader was used in that study, if it is assumed they share similar average source speeds, then the variation in dwell time difference can be justified.

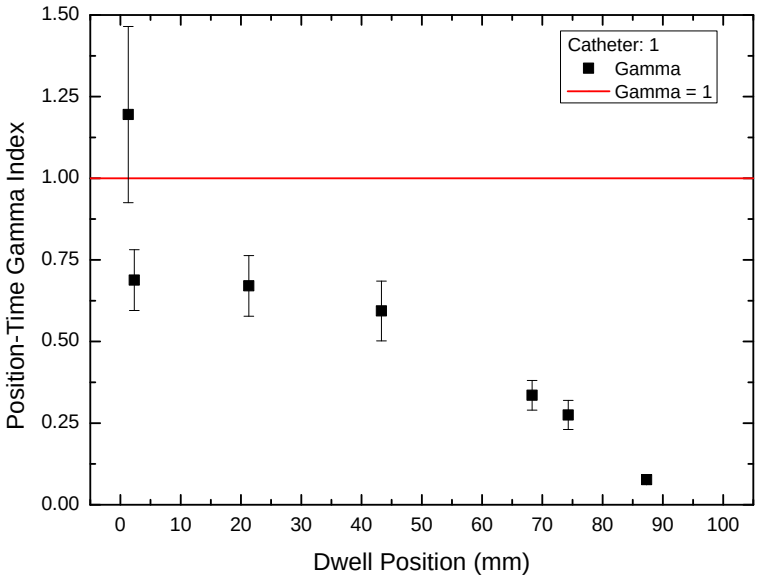

Figure 8.6: Gamma analysis for Catheter 1 (Criteria: DTA = 1.3 mm, TTA = 0.3 s).

The software suite, Brachy*Pix*, determines the dwell position and times for all the catheters and compares them against the treatment plan using the position-time gamma analysis. By applying the equations described in Table 8.1 to the dwell pattern of Catheter 1, the gamma index values for each dwell position were calculated and are shown in Figure 8.6. Taking into account the differences between the calculated dwell position and times, the DTA and TTA were set to be 1.3 mm and 0.3 s, respectively.

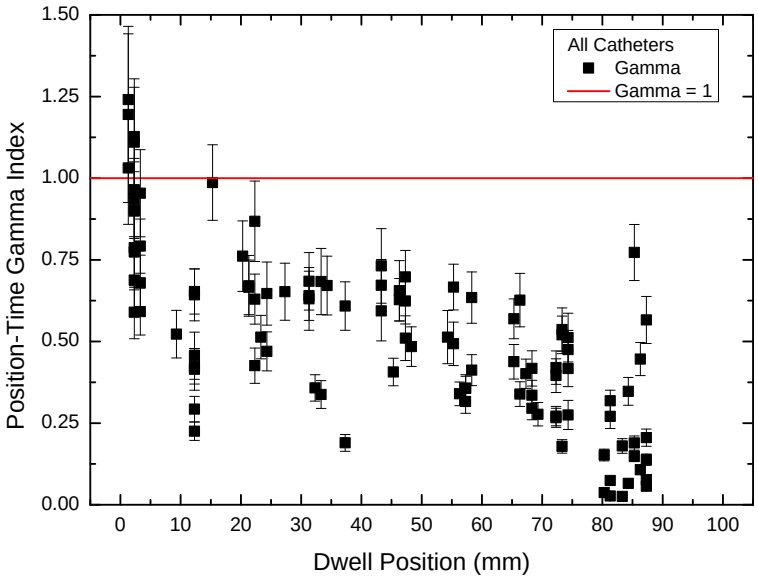

Figure 8.7: Gamma analysis for all catheters (DTA = 1.3 mm, TTA = 0.3 s).

Applying the gamma index to all 20 catheters, it can be seen from Figure 8.7 that the majority of the treatment (95%) have gamma values of less than or equal to 1. There are 5 points with gamma values greater than 1, but they are considered to pass, due to their uncertainty, derived from Equation 8.1.

8.3 Verification of the modified plan

A copy of Plan – 1 was created and modified by a member of the hospital medical physics staff, without the supervision of the authors, and an undisclosed number of changes were made. This modified version of the plan was named Plan – 2. Any differences in dwell position and time larger than the position-time gamma index criteria would result in a gamma value of greater than 1, and indicate that a simulated afterloader error had been detected.

Methods

The plan was altered by the inclusion of new dwell points, points shifted or removed; and some dwell times lengthened or shortened, to simulate a scenario where there is a misadministration by the afterloader. The plan was again delivered using the Nucletron Flexitron® HDR afterloader and calculated by the MPh.

Results

Plan –2 was measured using the MPh and based on the results from the position-time gamma analysis, an estimated 11 changes were believed to have been made to the treatment plan. One change to Catheter 3, seen in Figure 8.8, was the addition of a dwell position. This introduced position was seen to be at 17.2 ± 0.1 mm from the coordinate origin, with a dwell time of 14 s.

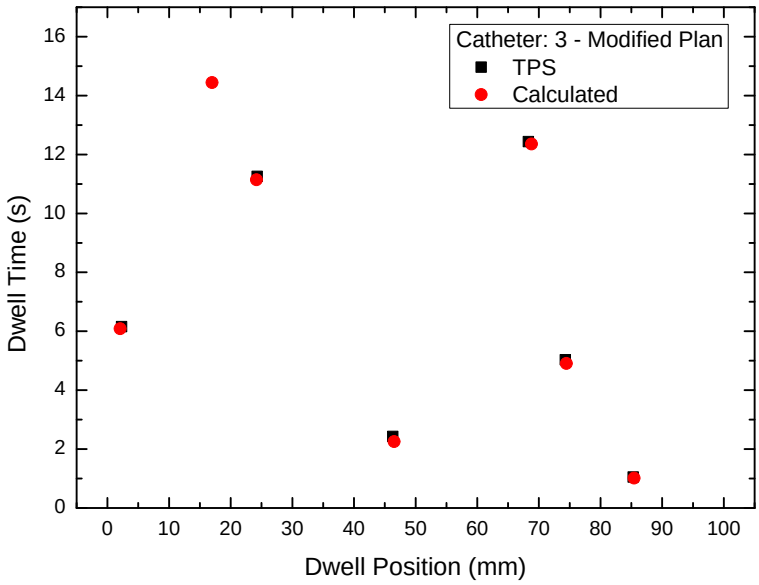

Figure 8.8: Comparison of dwell pattern for Catheter 3 against the TPS plan.

The introduction of the new dwell position causes the gamma analysis of this catheter,

seen in Figure 8.9, to fail the pass-fail criteria. A gamma value of 12.0 ± 1.9 was calculated based on the agreement between the introduced calculated position and the nearest TPS planned dwell point (position = 24.3, time = 11.3).

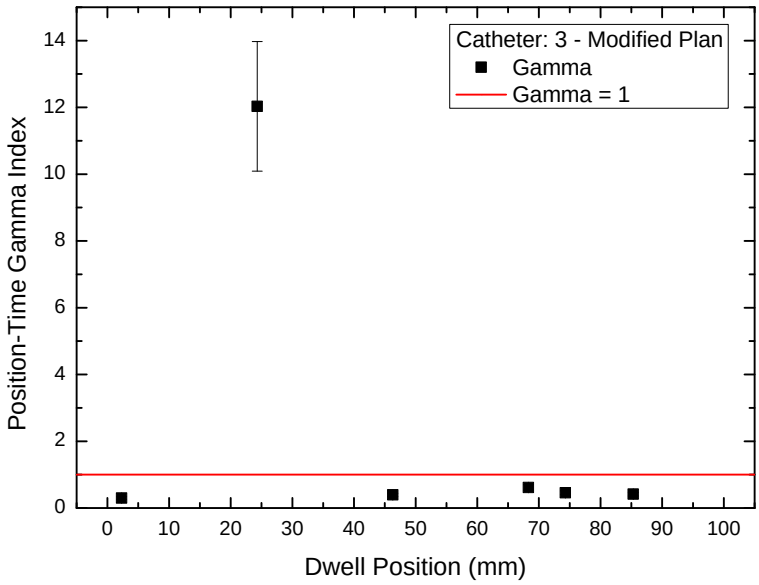

Figure 8.9: Gamma analysis for Catheter 3 for the modified plan (Criteria: DTA = 1.3 mm, TTA = 0.3 s).

Assessing the position-time gamma index for the entire modified treatment to the original plan, Figure 8.10 indicates 11 modified dwell positions. Upon analysing the modified treatment plan DICOM, these 11 alterations were verified to indeed be the introduced changes.

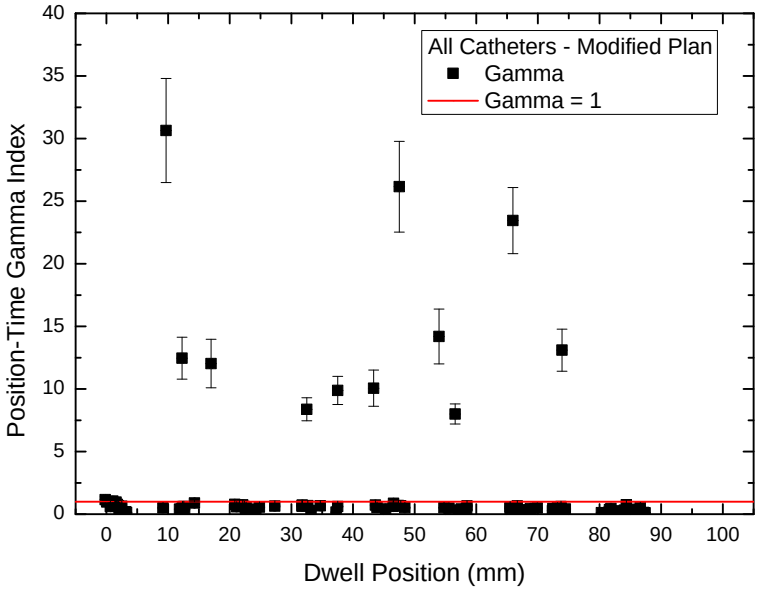

Figure 8.10: Gamma analysis for all catheters for the modified plan (Criteria: DTA = 1.3 mm, TTA = 0.3 s).

8.4 Comparisons between "Magic Phantom" calculated dose, TPS and EBT3 film dose

Brachy*Pix* performs dose calculations based upon the TG-43U1 protocol, and was tested to ensure that based upon the TPS planned dwell positions, times and dose calculation points, Brachy*Pix* agreed with doses determined by Nucletron ONCENTRA® TPS. Once Brachy*Pix* calculations were verified, two dimensional dose maps were generated based upon the measured Plan – 1 and Plan – 2 deliveries, and compared to dose maps for these plans and dose calculated using EBT3 film.

Methods

In planning, each MP detector coordinate was selected for point dose calculations and stored inside the DICOM file, along with the source dwell positions and times. The DICOM file of the original plan was read by the MPh software, and the coordinates and value of each dose calculation point were acquired. A direct comparison between the values within the DICOM was performed for 121 points using the dose calculation engine of the software.

Using the software, dose maps were generated along the MPh detector plane for the original treatment plan, Plan – 1, the measured treatment based upon the calculated dwell positions and times, and for the modified treatment plan, Plan –2. Plan – 1 was then measured by replacing the MP detector with EBT3 film. The film was cut to match the size of the MP and markings were made for alignment. Both the film and MP were later scanned using the scanner, so that the film dose map positions could be registered to those calculated by the MPh software. The change in optical density was converted to dose using the calibration curve reported in Chapter 3.

Each dose map had a size of 10×10 cm^2, with pixel dimensions of 0.5×0.5 mm^2. The maps were compared using the 2D gamma analysis, proposed by Low et al. [96], with varying dose difference and distance-to-agreements criteria.

The total transit dose for the MPh diode positions was also estimated by performing dose calculations for each calculated source position between dwell positions, assuming a discrete source movement between consecutive frames.

Results

Good agreement was found between the MPh software estimated doses for the 121 positions and the TPS, with all values within ± 0.75% (2 S.D), suggesting that the dose calculation engine based on the predetermined dwell positions and time was correct. The calculated 2D dose map for the calculated dwell positions and times of the original plan is shown in Figure 8.11. The film was irradiated using Plan – 1 and processed to create a map with the same dimensions and resolution as the others.

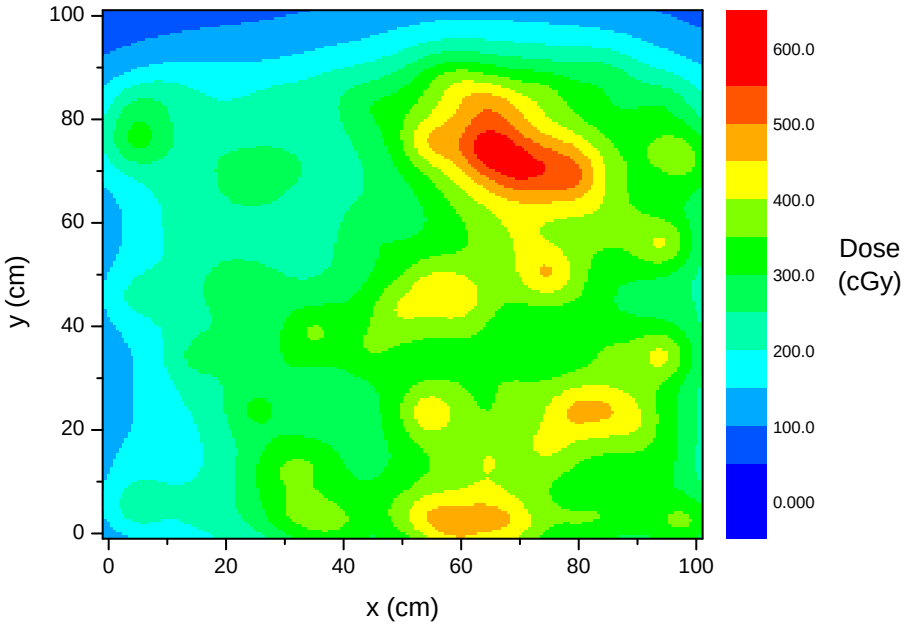

Figure 8.11: Dose to the MPh detector plane calculated using TG-43U1, based upon calculated dwell positions and times, without transit dose contribution.

Brachy*Pix* was additionally capable of estimating the contribution of the total transit dose for this plan by calculating the dose delivered for the sampled transit positions only. Seen in Figure 8.12, the total maximum transit dose was calculated to be 18 cGy for the measured plan, based on a source activity of 18 mGy.m^2.h^{-1}. This represents an average of 4.8 ± 2.3% increase in dose delivered when compared to the total dose delivered from the dwell positions only on a point-by-point comparison. This result

is dependent on the source activity and for this particular plan the transit dose contribution could double when delivered directly after a source exchange, assuming the same transit times.

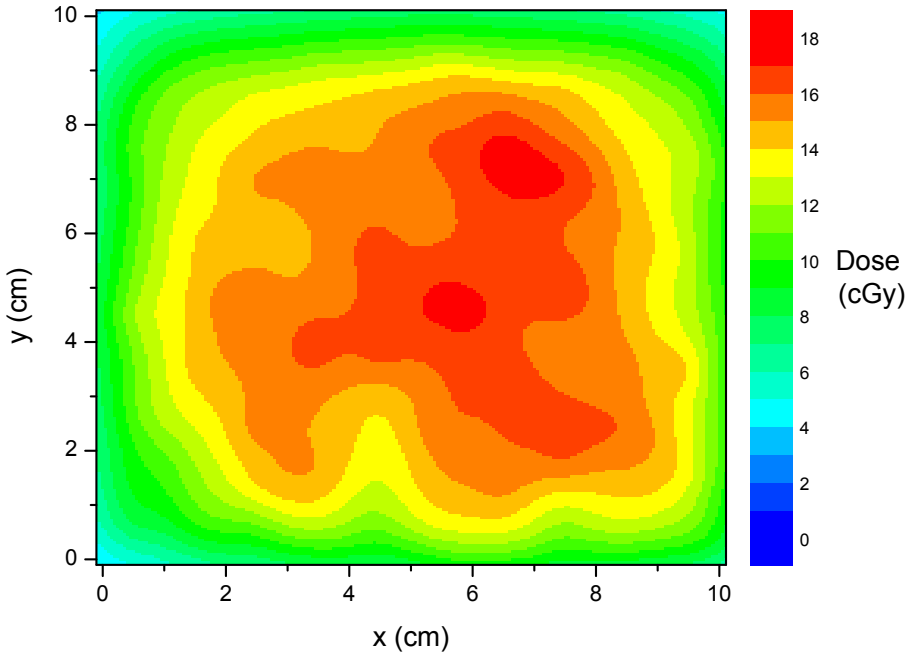

Figure 8.12: The calculated total transit dose contribution, delivered to the MPh detector plane for the unmodified treatment plan.

All dose distributions were compared using the 2D gamma analysis for varying dose difference and distance to agreement criteria, and the results are shown in Table 8.2. The global dose difference value was calculated based upon the maximum dose in the compared maps. It is seen that using a dose difference and distance to agreement of 4% and 3 mm, a pass rate of over 95% could be achieved for both the MPh dose map without the transit dose and the film for the original plan. Considering the transit dose contribution improved the pass rate, with a value of above 90% for all criteria examined, as found in Table 8.2. This suggests that the reduction of the dwell times is an appropriate method to compensate for the total transit dose when executing this plan. Using lower criteria values reduced the pass rate for film, most likely due to the

registration of the film position to the MPh and the associated uncertainty in the film dose calculation.

	Gamma pass rate (%) for DDA and DTA criteria		
Evaluated maps	2% / 2 mm	3% / 3 mm	4% / 3 mm
Measured by the MPh - Plan – 1	80.6	94.0	98.3
Measured by the MPh - Plan – 1 with transit dose correction	90.6	98.3	99.9
EBT3 film - Plan – 1	58.7	82.2	95.8
Measured by MPh - Plan – 2	30.1	40.3	49.3

Table 8.2: The comparison of calculated dose maps against the reference TPS planned dwell positions and times

Calculating the pass rate for the map of Plan – 2 gave a pass rate of 49.3% for the criteria (DDA = 4%, DTA = 3 mm), which is to be expected due to the simulated errors in afterloader delivery, confirming the gamma analysis is capable of detecting the introduced errors. Performing the dose calculations and using the 2D gamma analysis to compare the dose profiles allowed for additional verification of the treatment delivery, which could also be used to verify the dose calculations of the treatment planning system.

8.5 Discussion and conclusion

The MPh and software has demonstrated its ability to verify the created treatment plans for HDR brachytherapy in terms of dwell position and times. For the original plan, Plan – 1, the MP system was capable of measuring all dwell points and times

and the majority were found to be within 0.93 mm and 0.25 s, respectively, from the plan.

Using a distance-to-agreement and time-to-agreement criteria of 1.3 mm and 0.3 seconds, respectively, for the position-time gamma metric, all modifications made to the plan were able to be identified. This demonstrates the proof of concept of the position-time gamma metric for errors larger than the distance-to-agreement and time-to-agreement criteria, and allows for a quick and easy assessment of the afterloader performance.

When taking into account the FOV effect it was found that the difference in dwell positions was 0 ± 0.63 mm (2 S.D), agreeing with the results found in Chapter 6. When not considering this effect, this increased to 0 ± 1.30 mm, which is the basis for the distance-to-agreement criterion in the position-time gamma analysis. The use of the 0.3 second time-to-agreement criterion is based upon the afterloader reducing the dwell times to compensate for the transit time, but in afterloaders where this is not a feature, this criterion could be lowered substantially.

With adjustments to the treatment plan so that dwell positions fall between the $10 - 90$ mm length of the catheter, differences between the calculated and planned dwell times should be less than 0.7 mm. Dwell time differences that are significant and can not be explained due to the source transit time or large differences in dwell position should prompt user action to further investigate the afterloader performance. Currently, the MPh tolerances in dwell position and time are much smaller than the majority of experimental QA methods described in Chapter 2, with the additional benefit of a completely automatic software analysis.

The addition of the TG-43U1 protocol calculation to Brachy*Pix* allows for dosimetric information to be determined based upon the calculated treatment plan. This was found to be in agreement with the TPS calculated values and with experimental EBT3 film results. As dose is calculated solely on the MP plane by the software, dose to the target and to organs at risk could be recalculated by the treatment planning system based upon the calculated dwell positions and times, allowing for the an assessment of the effect of these treatment delivery errors.

Using this system, potential studies could assess the clinical implications of the determined transit dose by prospectively testing patient plans and assessing the additional dose delivered to the target volume and organs at risk. By developing Brachy*Pix* to accept planned patients treatment images, contoured volumes and catheter reconstructions, the total and transit dose could be calculated based on the MPh measured dwell positions and times, and transit motion. Analysing multiple treatments with different catheter numbers and source activities, it would be possible to determine the implications of the transit motion on the delivered dose and what amount is acceptable. If warranted, it would the be possible to assess the transit dose to be delivered to the patient yet to be treated when used for pre-treatment quality assurance.

Chapter 9

Pretreatment verification of clinical patient plans

As HDR brachytherapy plans become increasingly complex, it is important to develop pretreatment delivery verification methods that ensure the optimum treatment of patients [15]. While it would be ideal to perform an *in-vivo* verification during treatment, a pretreatment confirmation of the planned delivery could also ensure that there are no deviations between the source dwell times and positions, or incorrect lengths of catheters and step sizes used.

When estimating the total time for a pretreatment verification of a patient plan, it is necessary to consider the following factors: the time needed to set up the system, the planned prescription dose to the target, the HDR source activity at the time of measurement, the numbers of catheters planned, and the total dwell times based upon the prescription dose. As the execution of a treatment plan by the remote afterloader can take up to 30 minutes, the medical staff may not choose to deliver the full prescription dose for a pretreatment verification to the QA device when a reduced dose may result in similar outcomes within a shorter time.

This chapter seeks to evaluate the performance of the MPh QA system in evaluating real patient plans with varying numbers of catheter and prescription doses, for breast, prostate and vaginal treatments.[5] Six unique clinical patient plans were selected, based on their treatment type, and anonymized for testing in Nucletron ONCENTRA® TPS. The dwell times were set to match the patient post-treatment log, ignoring any variation in source strength between the plans.

All plans were delivered using the Nucletron Flexitron® HDR afterloader (Nucletron, an Elekta company, Elekta AB, Stockholm, Sweden) at the St George Cancer Care Centre, Sydney. Each patient plan was measured twice: first at 100% of the prescription dose and then at 20%. Measurements were analysed using Brachy*Pix*, and evaluated using the position-time gamma index to determine any changes in measurement quality.

9.1 Full plan delivery

Each of the selected treatment plans were delivered to MPh at the full prescription dose. The measured delivery was then compared to the plan and analysed using the introduced position-time gamma index.

Methods

Six patient plans (two prostate, two breast and two vaginal plans) were selected to cover a range of sites treated using brachytherapy. These types of treatments can have

[5] This chapter has been published in Biomedical Physics & Engineering Express:
A. Espinoza, M. Petasecca, D. Cutajar, I. Fuduli, A. Howie, J. Bucci, S. Corde, M. Jackson, M. Zaider, M. L. F. Lerch, and A. B. Rosenfeld, "Pretreatment verification of high dose rate brachytherapy plans using the "magic phantom" system," Biomedical Physics & Engineering Express, vol. 1, no. 2, 025201, 2015.

varying numbers of catheters: the vaginal plans used 1 catheter and an irradiation time of approximately 8 – 9 minutes, breast plans had 10 catheters and a time of 30 seconds per catheter, and the prostate plans used up to 19 catheters with a time of approximately 20 seconds per catheter. Each plan used a step size of 5 mm. The six plans were sequentially delivered, measured and analysed using the position-time gamma index.

Results

Each patient plan was measured using the MPh, and analysed using the source tracking method, with the dwell position and time calculation previously described in Chapters 5 and 6. The treatment plan DICOM file was imported into Brachy*Pix* to extract the catheter number, dwell position and timing information and perform the position-time gamma analysis.

Figure 9.1 a) shows a histogram of the difference in dwell positions between those determined by the software tool kit and the TPS. The average difference of the 363 dwell positions across the 6 plans, was found to be -0.01 ± 0.72 mm (2 S.D). The histogram of the difference in dwell times is shown in Figure 9.1 b) and has an average difference of -0.03 ± 0.11 s (2 S.D).

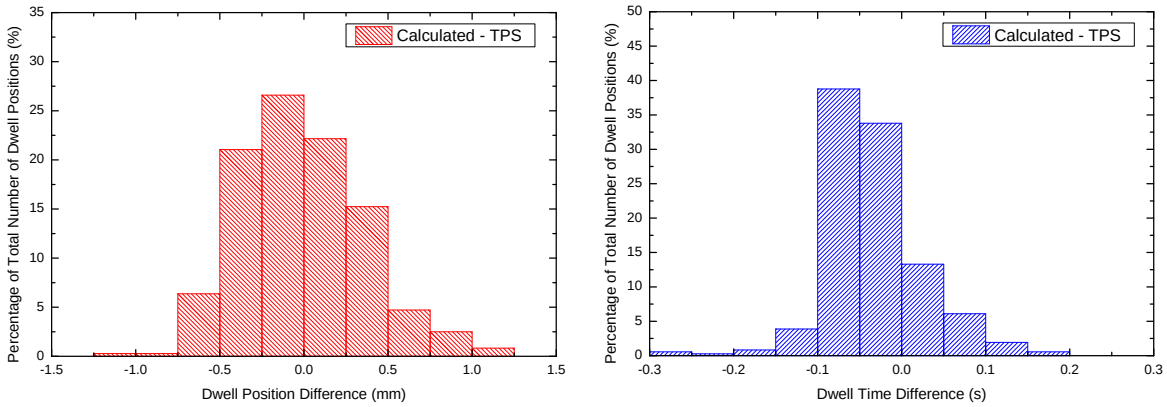

(a) Difference in dwell positions

(b) Difference in dwell times.

Figure 9.1: Histogram showing the difference in dwell positions and times between the calculated results and TPS for all the calculated dwell positions of the six patient plans.

Figures 9.2 a-f) show the results of the position-time gamma index for the six patient plans, with the origin of the dwell position axis equal to the first dwell position selectable in the TPS. Using a distance-to-agreement and time-to-agreement criteria based upon the absolute maximum differences of 1.3 mm and 0.3 s, respectively, all measurements achieved a pass rate of 100%, which showed that no delivery errors had been detected. Two plans, Breast – 2 and Prostate – 2, had gamma index values close or over 1, but were considered to pass due to the uncertainty calculated.

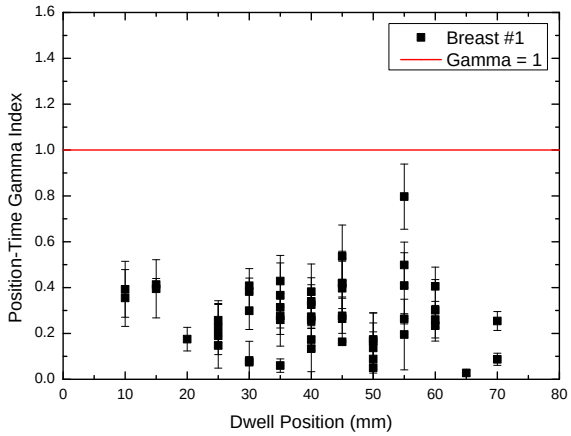

(a) Breast – 1

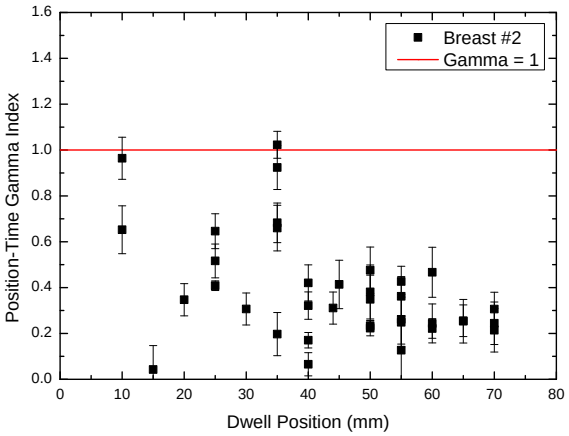

(b) Breast – 2

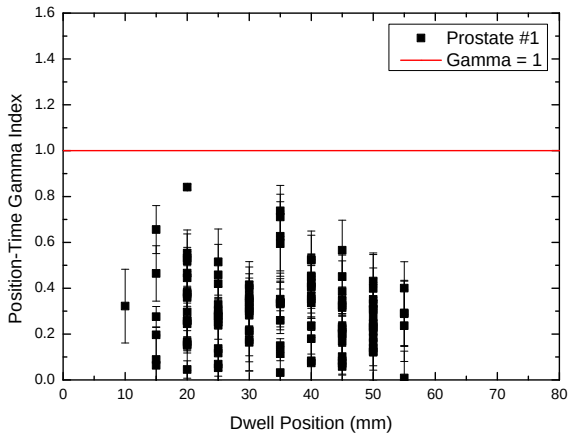

(c) Prostate – 1

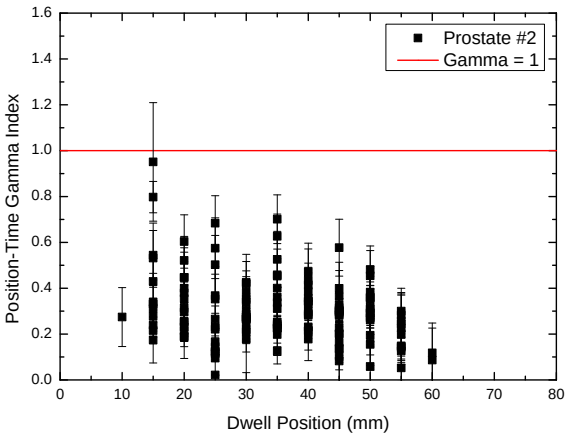

(d) Prostate – 2

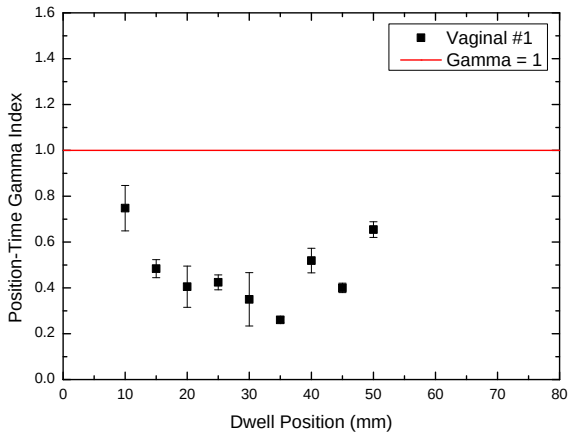

(e) Vaginal – 1

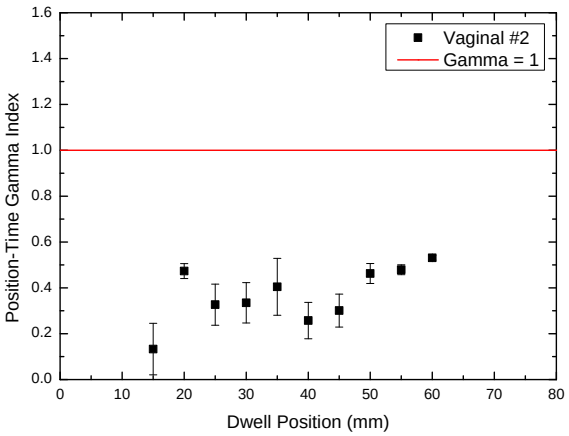

(f) Vaginal – 2

Figure 9.2: The position-time gamma analysis for the measured six patient plans (Criteria: DTA = 1.3 mm, TTA = 0.3 s).

The time structure for each measured plan is shown in 9.1 which shows how many catheters were used by the remote afterloader in treatment delivery for each plan, the total planned dwell times, the total calculated times, and the total time of irradiation from when the source is first detected by the MPh, to when it leaves the final catheter.

Treatment plan	Number of catheters	Sum of planned dwell times (s)	Sum of calculated dwell times (s)	Total treatment time (s)
Breast – 1	10	323.6	322.8	572.0
Breast – 2	10	158.4	157.5	408.8
Prostate – 1	18	355.4	352.8	810.8
Prostate – 2	19	356.4	353.4	835.9
Vaginal – 1	1	486.7	487.8	489.4
Vaginal – 2	1	518.0	519.2	520.7

Table 9.1: Planned and calculated dwell times and total time for verified plans.

Using the Nucletron Flexitron® HDR afterloader, there is a 25-30 s delay while the source is inside the afterloader safe between entering the catheters, as the afterloader drives the check cable through each catheter to test for obstructions. For safety reasons, this check cable run cannot be switched off on this afterloader in clinical operation. With a higher number of catheters the total treatment time increases, and currently cannot be avoided. The total treatment transfer time (T_{tran}) was measured and can be calculated for n-catheters ($n > 1$) by using a linear model

$$T_{tran} = a \times (n - 2) + b \tag{9.1}$$

where a = 24.8 ± 0.6 s and b = 35.1 ± 2 s, derived from the measurement analysis.

9.2 Accelerated delivery

The prescription dose for each plan was reduced to decrease the time needed for pre-treatment QA. The feasibility of this method was assessed by comparing the resulting position-time gamma analysis and any differences in afterloader delivery performance.

Methods

For each of the six patient plans, the prescription dose was decreased by a factor of 80% to reduce the total irradiation time, resulting in faster delivery execution. This reduction was selected to test the feasibility of this method, but other reductions could be used to ensure that a delivery takes no longer than a specified time, e.g., no more than 5-10 minutes. Each modified plan was measured using the MPh and the results of the position-time gamma analysis were compared to those of the full prescription dose.

Results

The prescription dose for each of the six patient plans was reduced by 80% using the TPS and measured using the MPh. A comparison of the results of the dwell position and timing analysis to the plans is seen in Figures 9.3 a) and b). The average difference between the calculated and planned dwell positions and times were found to be -0.01 ± 0.73 mm (2 S.D) and -0.05 ± 0.10 mm (2 S.D) respectively, and are in agreement with the results found in the previous section.

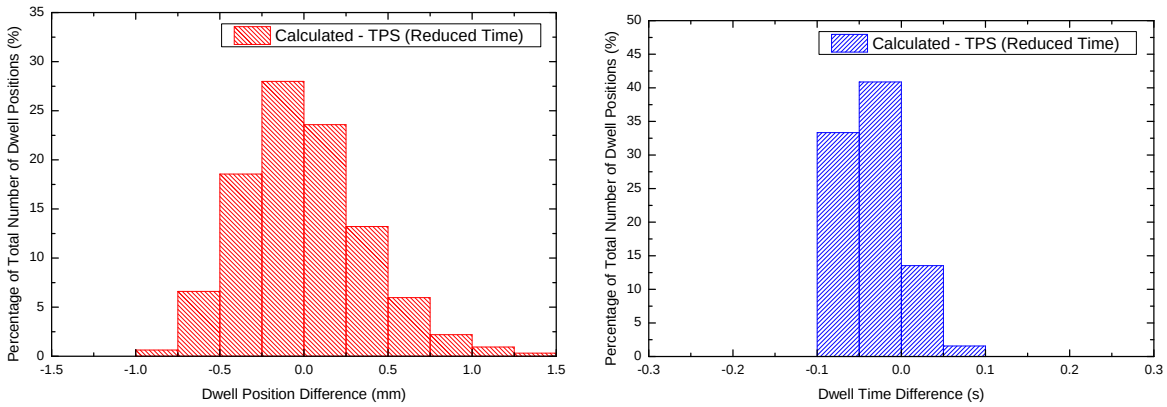

(a) Difference in dwell positions

(b) Difference in dwell times.

Figure 9.3: Histogram showing the difference in dwell positions and times between the calculated results and TPS for all the calculated dwell positions using the accelerated method.

The differences in position may be due to the accuracy of the MPh system in determining the source position but could also be due to possible shifts in the dwell position from slight variations in the individual transfer tube length, and the reported effect of the flexing of these transfer tubes [37, 38]. While the effects of the curvature of the transfer tube were not evaluated in this study, the measurements were set to replicate a clinical delivery, with the phantom placed on the treatment couch at an appropriate height and distance from the afterloader. The differences in dwell times is attributed to the Nucletron Flexitron® HDR afterloader compensating for the source transit time as described in Chapter 8.

The position-time gamma analysis of the accelerated version with the reduced prescription doses are seen in Figures 9.4 a-f). It can be seen that, although the prescription dose was reduced by 80%, the accelerated plan was able to be measured and give a comparable gamma analysis result. All treatment measurements had a pass rate of 100% using the same distance-to-agreement and time-to-agreement criteria.

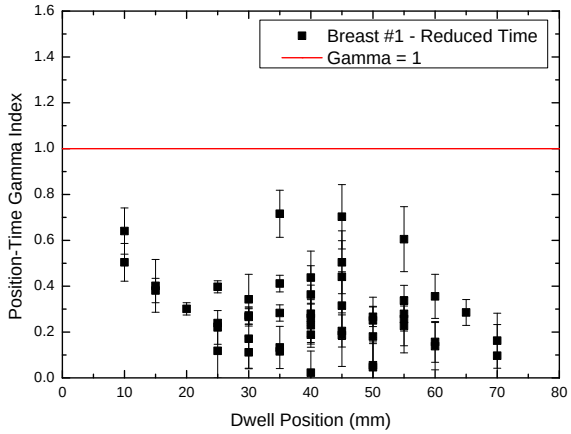

(a) Breast – 1

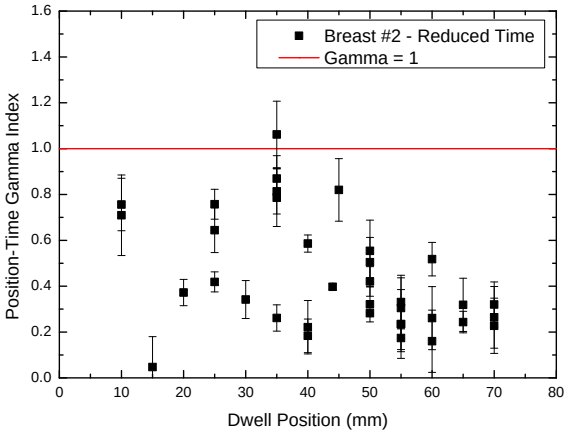

(b) Breast – 2

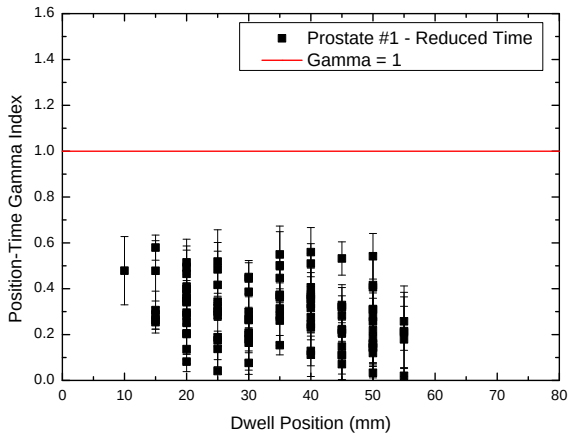

(c) Prostate – 1

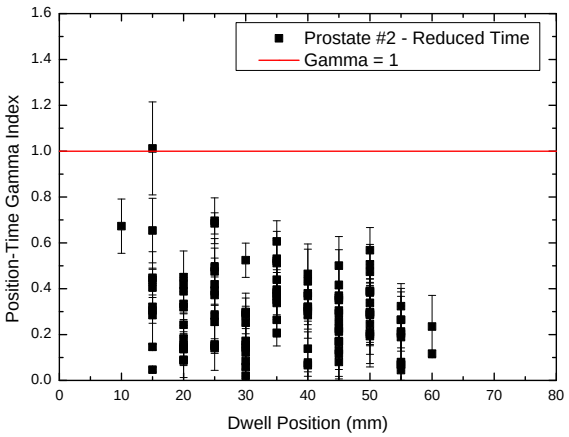

(d) Prostate – 2

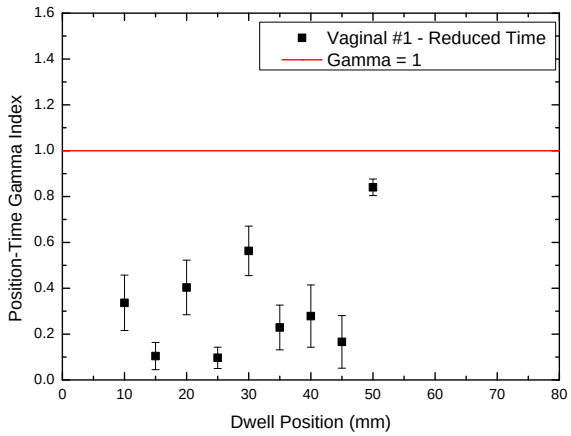

(e) Vaginal – 1

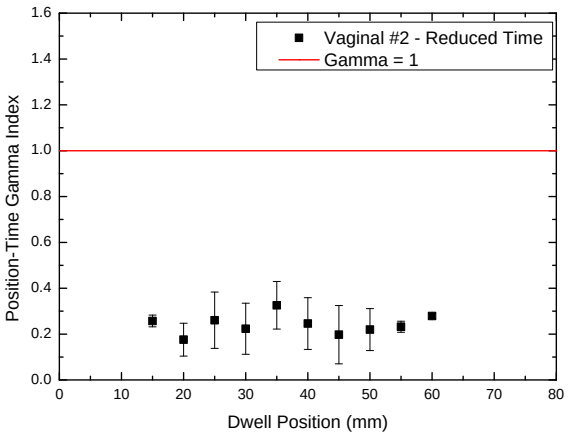

(f) Vaginal – 2

Figure 9.4: The position-time gamma analysis for the measured accelerated six patient plans (Criteria: DTA = 1.3 mm, TTA = 0.3 s).

The total treatment time reduction was found to be much less than 80% for multiple catheters, as seen in Table 9.2. Although the sum of the dwell times had decreased, the time taken for the cable check runs were the same as the full prescription dose plans. Also shown in this table, as the prescription dose was reduced, many dwell positions were neglected by the remote afterloader.

This is due to two reasons: those dwell times originally less than 0.5 seconds were rounded down to 0 by the TPS (this occurred 30 times across the 6 patient plans) and the reduced dwell times were further shortened by the afterloader compensating for time taken to step the source between dwell positions. If the time for stepping motion was larger than the reduced dwell time, the position was omitted (this occurred 15 times across the 6 patient plans). At the cost of increased total measurement time, those dwell times affected by the transit motion could be rectified by adjusting the reduction in prescription dose to ensure these dwell positions are executed.

Treatment plan	Sum of planned dwell times (s)	Sum of calculated dwell times (s)	Number of dwell positions omitted	Total treatment time (s)	Total time reduction (%)
Breast – 1	60.8	59.1	3/51	308.2	46.1
Breast – 2	31.2	29.9	1/37	281.2	31.2
Prostate – 1	69.8	67.0	16/116	551.8	31.9
Prostate – 2	68.8	66.5	25/140	575.1	31.1
Vaginal – 1	99.2	99.3	0/9	100.7	79.4
Vaginal – 2	103.6	103.51	0/10	105.2	79.8

Table 9.2: Planned and calculated dwell times and total time for accelerated plans.

The prostate – 2 plan had 25 dwell positions omitted, 7 of which were due to the afterloader compensating for the time taken to move the source between the dwell positions, and the remaining omissions due to the dwell time being rounded down to 0. From the presented data, it is possible to see that for the vaginal single catheter case, the time reduction in comparison with the original check is approximately 80%. A similar time reduction could be achieved for breast and prostate treatment if the cable run checks were avoided in service mode.

9.3 Discussion and conclusion

It has been shown that using the MPh HDR pretreatment QA device, it is possible to verify patient plans, with all calculated dwell positions and times were found to lie in 0.7 mm and 0.3 s, respectively. While treatment verification can be time consuming due to the execution of the plan by the afterloader, the presented method of reducing the time by a large reduction in the plan prescription dose may be an adequate solution. By using a reduced prescription dose, it was seen that there were no large discrepancies introduced to the dwell position when assessed by the position-time gamma analysis.

The concept of accelerated verification has the advantage that it can increase the throughput of testing multiple treatment plans, especially when using low activity sources that typically result in longer irradiation times. It can have substantially shorter measurement times with very similar outcomes to the full prescription dose plan, in terms of the differences between dwell positions and times, and the position-time gamma analysis.

If it were possible to remove the cable check run for each catheter in a special diag-

nostic QA mode of the afterloader, the practicality of this method would be greatly enhanced. This mode should perform a single complete cable check run, prior to multiple measurements, to ensure that the transfer tubes are connected correctly and that no defective catheters were used, minimizing the risk of potentially damaging the source and its cable.

The obvious drawback is that the actual patient plan is not verified. This may result in an incorrect evaluation of the quality of treatment delivery to be expected to the patient at the time of treatment. As shown in these results, a significant number of dwell positions in the plan which had short dwell times were rounded to 0 by the TPS when the reduced time was less than 0.1 of a second. The significance of these omitted dwell positions must be evaluated in the context of the rest of the treatment plan.

This method gives the operator the option of accelerating the treatment check, allowing for the verification of source dwell positions and the scaled dwell times against the treatment plan. As the MPh has each catheter numbered, it may distinguish when catheters have been incorrectly connected by the transfer tubes and identify the cause of a gamma criteria failure. Scaled dwell times below 0.1 s were omitted by the treatment planning system as a result of using the fixed 80% prescription dose reduction for this feasibility test. In practice, the user would set this reduction to ensure a more preferable execution of the plan.

Chapter 10

The feasibility of the "Magic Plate" for *in-vivo* source tracking

The previous chapters have assessed the role of the "Magic Plate" for HDR brachytherapy pretreatment quality assurance. The aim of this final experimental chapter is to project the source tracking technique into the application of *in-vivo* verification and to explore possible limitations of this method. The preliminary testing of this concept will apply the source tracking method to large distances within Solid Water®, simulating the tracking of the source inside the human body.

All plans were delivered using the Nucletron Flexitron® HDR afterloader (Nucletron, an Elekta company, Elekta AB, Stockholm, Sweden) at the St George Cancer Care Centre, Sydney.

10.1 Tracking the HDR source in body

Due to the positioning of the patient during treatment, there are few places where the placement of the MP detector could be feasible. A practical option, as seen in Figure 10.1, could be to place the MP directly beneath the patient being treated, possibly inside the treatment couch or a patient transfer system like the Zephyr HDR Patient Positioning and Transfer System [98]. A specialised gurney with the MP could be used during both the CT imaging of the patient and in treatment, to obtain accurate information about the patient anatomy and the catheter positions relative to the MP detector.

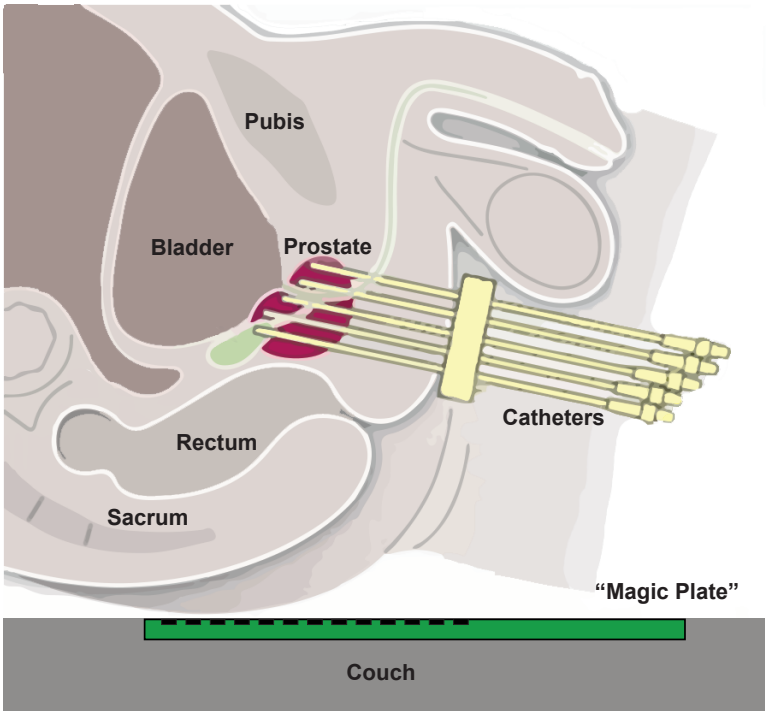

Figure 10.1: A possible placement of the MP relative to the human body.

The prostate, as described in Chapter 2, is located deep inside the pelvis, between the bladder and the penis. Placing the MP detector underneath the patient during

treatment would mean that the distance from the HDR source to the MP detector could be between 90 - 150 mm. For the verification to be accurate, the source tracking method must work at these large distances within the body.

The source tracking algorithm was designed to calculate the ^{192}Ir source position within Solid Water®. While tissue can be approximated by water, for prostate cancer in particular, there are different mediums between the source and the MP that would have to be taken into account during the source tracking procedure. Mediums such as air gaps, bones and introduced materials, could change the radiation field measured outside the body.

Air gaps, that may be inside an empty rectum, are less attenuating than tissue and result in a larger flux of photons and thus a larger current generated at the MP. This would cause the tracking algorithm to determine the source to be closer than its actual position. Bones, such as the sacrum at the end of the spine, would have a higher effective atomic number than water, and would result in a decrease in current generated due to higher radiation attenuation. This would cause the MP algorithm to calculate the source position further away.

During the surgical insertion of the catheters, a transrectal ultrasound (TRUS) probe is typically used to guide the placement of the HDR catheters into the prostate. In some clinics, the image obtained from the TRUS probe is used to perform the treatment planning, as opposed to the use of the CT image. The physical placement of the TRUS probe may lead to a distortion of the shape of the rectum and prostate, and so to ensure that the dose calculations and planning are valid, the TRUS probe is kept inside the patient during treatment. The probe, made of plastic and ceramic with a large brass backing, would also act as a attenuator of the radiation and as a source of

scatter, between the ^{192}Ir source and the MP detector.

10.2 Source tracking feasibility

The feasibility study performed in Chapter 4 showed that the ^{192}Ir source was able to generate current in the MP detector at distances up to 150 mm. In this chapter, the HDR tracking algorithm is applied to measurements of the source position at SDD of 120 mm, inside a SW phantom, with varying measurement configurations to simulate tracking in the human body.

Materials

Measurements were performed using two additional materials, a TRUS probe without it's plastic casing, and a PVC bone substitute.

The TRUS probe

The TRUS probe used in this experiment was the Endocavity Biplane Transducer Type 8848 produced by BK Medical, used for transrectal scanning for brachytherapy treatments, Figure 10.2. It features two arrays for transverse and sagittal ultrasound transducers that can be used for the separate or simultaneous imaging of both planes. It is used to determine the prostate volume, and for monitoring the insertion of catheters during the procedure.

Figure 10.2: BK Medical Endocavity Biplane Transducer Type 8848 probe.

Underneath the TRUS probe casing there are the two arrays for the ultrasound imaging, and a 110×15×3 mm^3 bar of solid brass. The brass is used as an absorber to improve the ultrasound image quality by blocking the reflections in the incorrect image plane. Brass is an alloy of copper and zinc, and thus has an effective atomic number between 29 – 30, depending on the exact composition. It is therefore assumed that the brass inside the probe would be a large attenuator of the radiation field, and a wide scattering source inside of the phantom.

The PVC bone substitute

Polyvinyl chloride (PVC) was selected as a surrogate material to investigate the effect of the sacrum on the radiation field measured by the MP detector on the surface of the body. While PVC is not a standard bone substitute in medical physics, its low cost, availability and equivalent electron stopping power and attenuation coefficient over the ^{192}Ir energy spectrum, it was selected for use in this study.

The sacrum is made of cancellous bone, which is assumed to be similar to the cortical

bone composition estimated by the International Commission on Radiological Protection (ICRP) [99]. The compositions of cortical bone, estimated by the ICRP, and PVC are presented in Tables 10.1 and 10.2.

Element	Atomic number	Fractional weight
Hydrogen	1	0.047234
Carbon	6	0.144330
Nitrogen	7	0.041990
Oxygen	8	0.446096
Magnesium	12	0.002200
Phosphorus	15	0.104970
Sulfur	16	0.003150
Calcium	20	0.209930
Zinc	30	0.000100

Table 10.1: The elemental composition of the ICRP cortical bone [99].

Element	Atomic number	Fractional weight
Hydrogen	1	0.048380
Carbon	6	0.384360
Chlorine	17	0.567260

Table 10.2: The elemental composition of PVC. Data obtain from NIST database [100].

The different elements in PVC and cortical bone have varying photon interaction cross-sections. The NIST database of x-ray mass-energy absorption coefficients features data on both PVC and the ICRP cortical bone, and these were compared over the energy range of 1 - 1000 keV [77]. Figures 10.3 a) and b) show that, over this energy range,

PVC exhibits a similar behaviour to bone at energies larger than 100 keV.

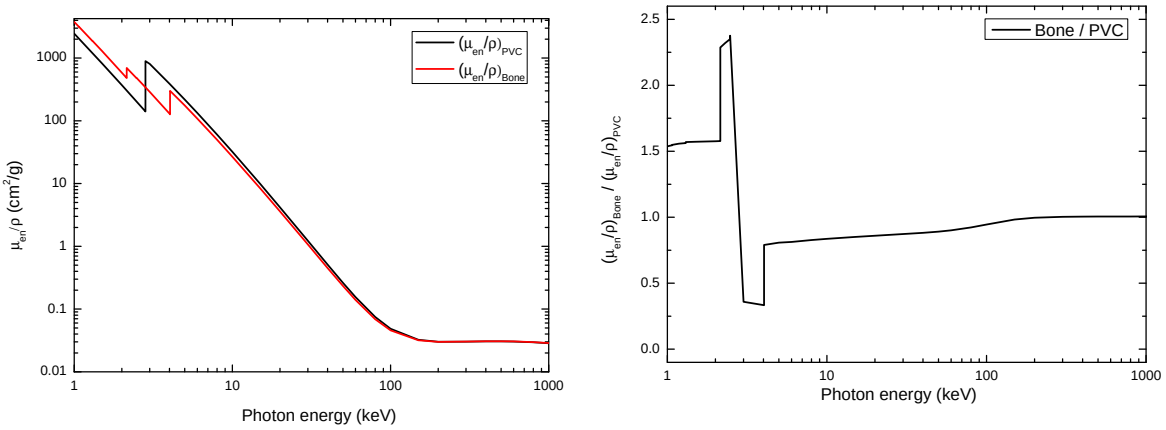

(a) μ_{en}/ρ for PVC and ICRP cortical bone. (b) Ratio μ_{en}/ρ for PVC and ICRP cortical bone.

Figure 10.3: Comparison between PVC and ICRP cortical bone mass-energy absorption coefficients.

A software tool kit was developed by Taylor et al. [101], named auto Z_{eff}, to perform a robust, energy dependent calculation of the effective atomic number, Z_{eff}, of any material. The calculation is performed by considering the photon interaction cross sections for elements Z = 1 – 100 over then energy range of 10 keV to 10 GeV, and determining the atomic cross section of composite materials. The software is capable of determining the average Z_{eff} over an energy range of 10 keV to 1 GeV, and can also give a spectrum weighted Z_{eff}. Using the compositional elements of cortical bone and PVC, the ^{192}Ir spectrum weighted Z_{eff} for each material was calculated to be 5.34 and 5.41, respectively.

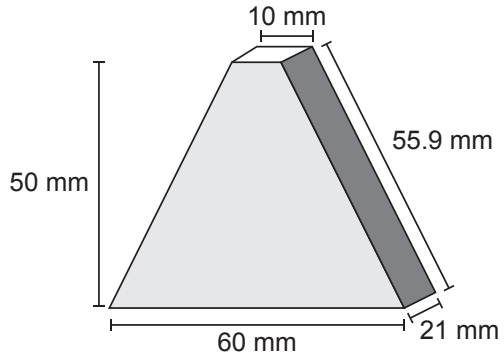

Figure 10.4: The dimensions of the PVC bone substitute.

The design of the PVC substitute is shown in Figure 10.4. The approximate shape and dimensions of the sacrum were obtained by comparing 5 CT scans of male patients treated for prostate cancer by HDR brachytherapy. It is noted that this a very simplified design, as it does not take into account the curvature of the sacrum, but is likely to be suitable for this feasibility study.

The density of cortical bone is estimated to be 1.85 g/cm^3, which differs to PVC, which is 1.30 g/cm^3. To compensate for the different densities, the thickness of the PVC substitute was increased to 21 mm, from the 15 mm thickness estimated from the CT images. A CT scan of the PVC substitute found that the material had an electron density of 1.447 relative to water, which was similar to the values of 1.473 and 1.707 for bone substitute CB2 50% CaCO3 and cortical bone substitute, part of the Gammex 467 Tissue Characterization Phantom (Gammex Inc., Middleton, WI, U.S.A), used in the QA of the CT scanner.

Methods

The MP was used to perform measurements in the four configurations shown in Figure 10.5. The HDR source was programmed to drive towards the catheter tip at a 5 mm

step size, with a dwell time of 2 seconds at each dwell position. An attempt was made to ensure that all pieces of SW were aligned on top of each other, as deviations along the catheter x- and y-coordinates would hinder the comparison between cases.

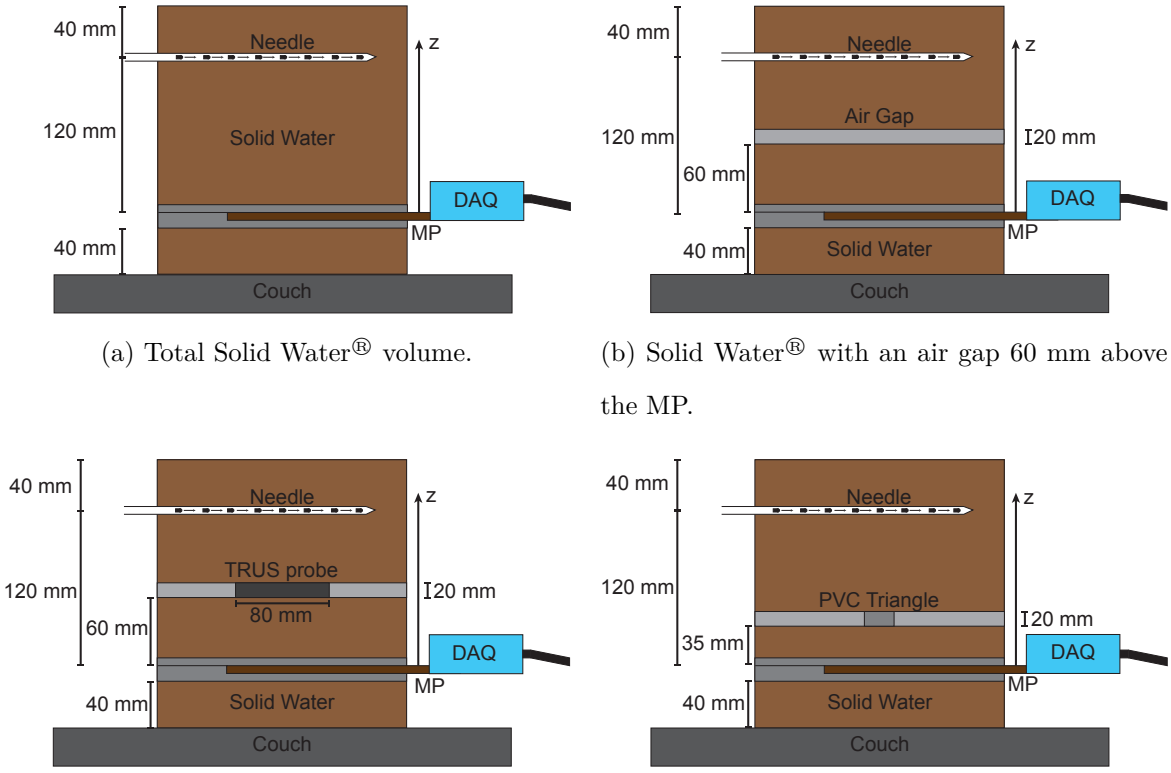

(a) Total Solid Water® volume.

(b) Solid Water® with an air gap 60 mm above the MP.

(c) Solid Water® with the TRUS probe 60 mm above the MP.

(d) Solid Water® with the PVC triangle 35 mm above the MP.

Figure 10.5: The four measurement configurations.

The air gap, Figure 10.5 b), was created by placing two 30×15×20 mm^3 pieces of SW onto the stack, and separating them perpendicular to the catheter by 20 mm. These pieces of SW allowed for the placement of both the TRUS probe in Figure 10.5 c) and the PVC triangle in Figure 10.5 d).

To minimise the statistical fluctuations in the current due to the low event rate, the integration time of the AFE DAQ system was set to 9920 μs. As a consequence, the

measurement frequency was set at 100 Hz, reducing the temporal resolution to 10 ms.

Results

The current generated in the central MP detector over the entire source movement is shown in Figure 10.6. It is seen that both the PVC bone substitute and TRUS probe attenuated the radiation field, while the air gap increased the measured current, when compared to the SW scenario. The air gap configuration measured an average current increase of 15.5 ± 2.2%, while the PVC and TRUS probe decreased the measured current by 3.7 ± 1.8% and 8.7 ± 1.7%, respectively. It is expected that this variation in response will diminish the accuracy of the source localisation procedure.

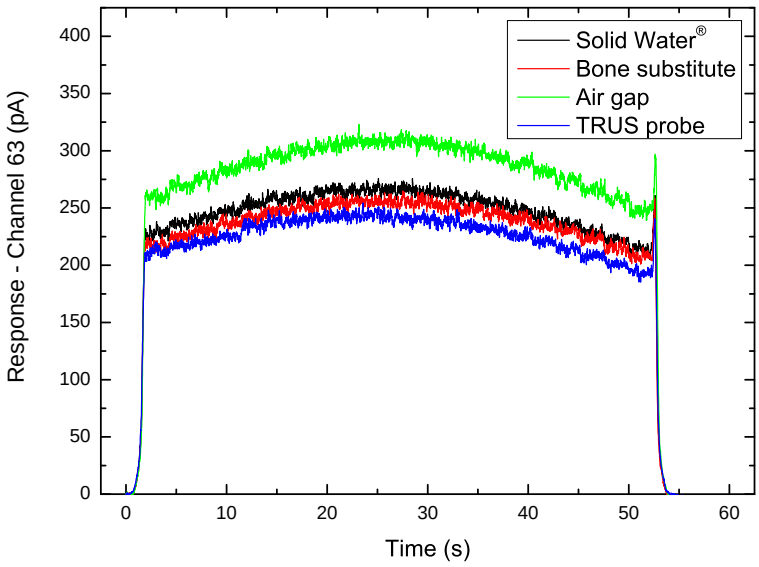

Figure 10.6: The current measured by the central MP detector for the four configurations.

The results of the source tracking along the y-coordinate are shown in Figures 10.7 a), b), c) and d). All four results seem to follow the expected position of the HDR source when the source is inside the centre of the MP FOV, while the SW case and the air gap begin to differ at the edges. The effect of the attenuating PVC bone and TRUS

probe seems to have little bearing on the y-coordinate tracking, and appears to be an improvement on the SW and air gap case.

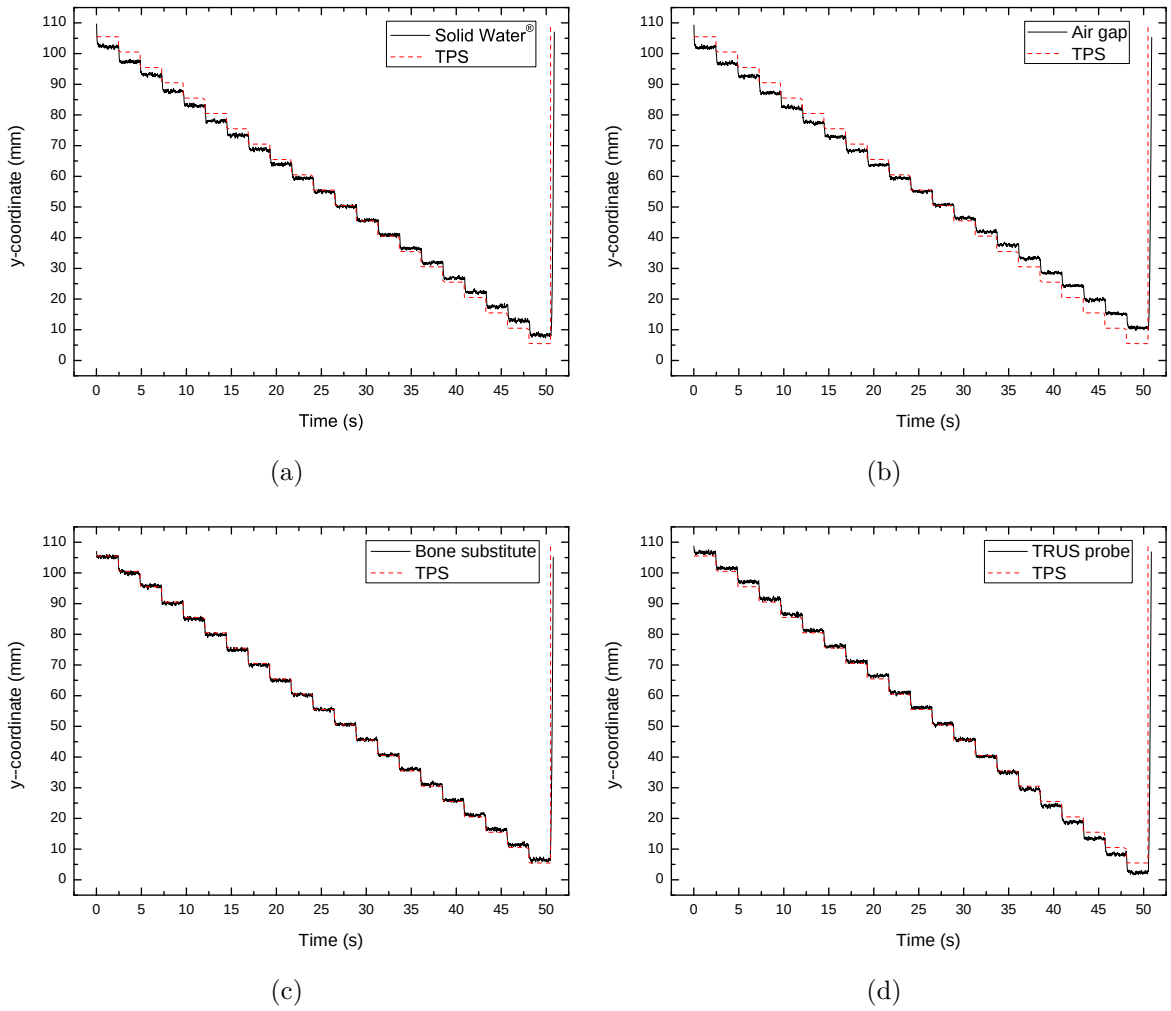

Figure 10.7: Results of the source tracking along the y-coordinate a) in SW, b) in SW with air gap, c) in SW with PVC, and d) in SW with TRUS probe.

The catheter x- and z-coordinates were fixed during the measurement to $x = 50$ mm and $z = 100$ mm, and it was assumed the source coordinates would be constant over the measurement. However, Figures 10.8 a) and b) show that the source localisation is being calculated incorrectly due to the placement of the inhomogeneous materials and their effect on the measured radiation field.

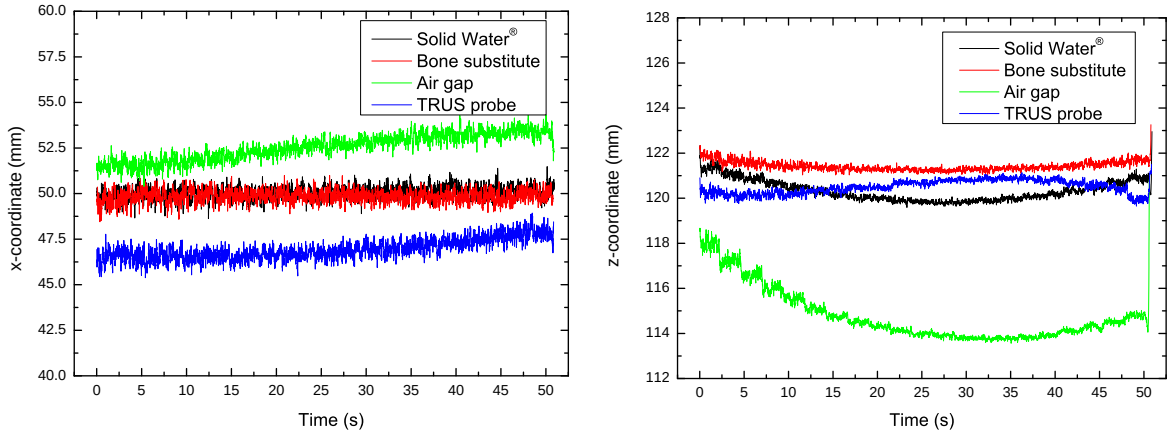

(a) The x-coordinate.

(b) The z-coordinate.

Figure 10.8: Results of the source tracking along the a) x-coordinate, and b) z-coordinate.

The most likely cause of the differences in the source tracking results is the effect of the varied detector responses due to the materials. By integrating the response in all of the MP detectors over each measurement, a comparison could be made for the PVC, air gap and TRUS probe against the SW configuration. The integral responses of the three configurations with inhomogeneities were divided, detector by detector, by that of the SW measurement, and graphed in Figure 10.9. The uncertainty of the integrals were calculated based off the standard deviation of 3 measurements per configuration and were found to be less than 1%.

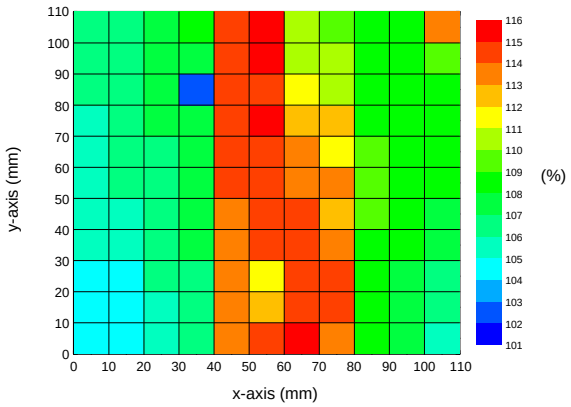

(a) The air gap/SW.

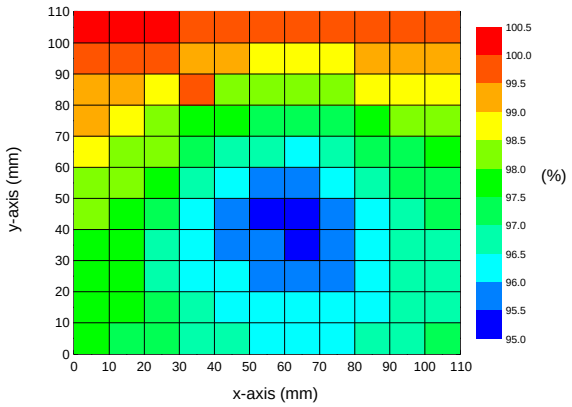

(b) The PVC bone substitute/SW.

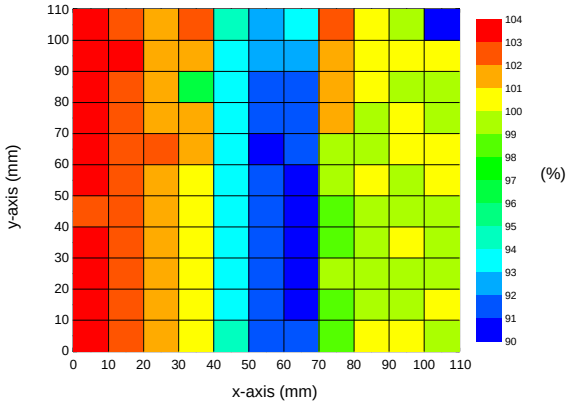

(c) The TRUS probe/SW.

Figure 10.9: The comparison of the integral MP response a) the air gap to SW, b) the PVC bone substitute to SW and c) the TRUS probe to SW.

Figure 10.9 a) compares the air gap to the SW integral and shows a large increase in signal down the middle of the MP detector, where the air gap had been placed, at approximately $x = 50$ mm. Detectors outside the direct path of the radiation from the source to the air gap also had an increase in signal of over 5 – 6%. The PVC bone substitute decreased the integral response by up to 5%, forming a projected image at the approximate placement of the material in Figure 10.9 b). The TRUS probe, in Figure 10.9 c), was seen to attenuate the radiation field up to 10%, with the effect most apparent at detectors directly underneath it.

10.3 Discussion and conclusion

The results of the *in-vivo* feasibility study show that it was possible to estimate the source position at large distances when the source was close to the centre of the MP FOV. The accuracy of the results of the estimation procedure was, however, limited by the following factors: the physical size of the MP detector array, the reduced signal-to-noise ratio at large distances, and the introduction of inhomogeneous materials between the HDR source and the detector itself.

To improve the source position calculation, the responses from the majority of the MP detectors were used to compensate for the relatively uniform dose profile when the HDR source was at large distances. Figure 10.10 shows that dose profile becomes flatter and wider for increasing source-to-detector distances, when normalised to the maximum dose calculated by the TG-43U1 protocol. By including the response of a larger number of detectors, an improvement to the calculation can be made as a better shape of the dose profile can be obtained.

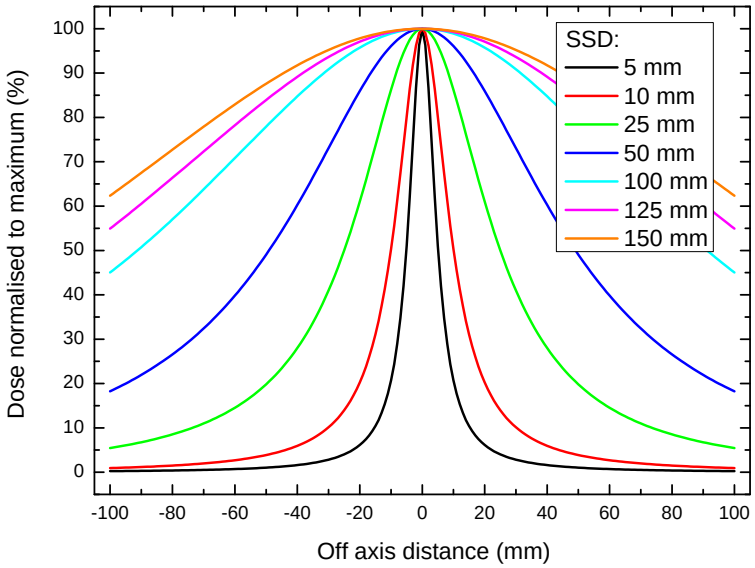

Figure 10.10: The normalised dose profile at different SDDs calculated using the TG-43U1 protocol.

When the HDR source is close to the edge of the MP FOV, the algorithm procedure cannot accurately determine the source position. While using the response of multiple detectors did improve it, a review of the procedure found that the sum of the squares of the relative error, Equation 5.4, could not be effectively minimised. A possible improvement in later generations of the MP could be to increase the number of detectors and the size of the FOV, to ensure better coverage of the lengths of the HDR catheters.

As noted earlier in the methods section of this chapter, the integration time for each measurement was set to 9920 μs, the maximum allowed by the electronics system, with a dead time of 80 μs. This was done to minimise the statistical fluctuations in the current generated in each detector by the low event rate of radiation. The low event rate is due to the amount of radiation fluence in the small cross-sectional area of the MP detector (0.6×0.6 mm^2) and the large SDD. The fluctuations in each detector response reduces the accuracy of the source localisation procedure, as large spikes can cause the algorithm to shift the estimated position closer to that particular detector. It is suggested that to minimise the fluctuations, and thus improve the signal-to-noise ratio, the detector size could be increased and also biased to increase the sensitive volume.

The non-tissue equivalent materials was found to change the MP response and hence, the source position calculation. One of the most important components of the source tracking method is the conversion of the measured detector response to the estimated source-to-detector distance. This is performed using a model that was determined from the results of the percentage depth dose measured inside of a full SW stack, presented in Chapter 4. It is clear that this model used in the localisation procedure is currently not capable of handling inhomogeneous materials placed between the source and detector.

The placement of the MP detector under the surface of the body may need to be reconsidered for patients where CT images indicate potential issues. With further research, the effect of the materials may be compensated for by using patient anatomy information from CT images to adjust the detector response. With the arrival of model-based dose-calculation algorithms in the near future, it may be possible to take into account the heterogeneous materials, and use the TPS to predict the dose rate at the MP detector for comparison.

If this method could not accurately take into account the effect of the TRUS probe, a possible solution could be to place the detector on the anterior surface of the patient, as opposed to the previously suggested posterior position. It is expected that the tissue and pelvic bone structure could be accounted for and the presence of the TRUS probe would not be an issue. The curvature of individual patients could be compensated by a moulded bolus, minimising air gaps between the patient and MP detector.

Chapter 11

Conclusion

The aim of this thesis was to develop a quality assurance system for the verification of HDR brachytherapy delivery. This was realised by adopting an 11×11 array of silicon detectors and pairing it with a fast electronic readout system. Using a source localisation algorithm, dwell positions and times were measured in phantom, and then tested for possible in-treatment monitoring.

11.1 Final summary

Chapter 2 provided a general introduction to prostate cancer and the use of high dose rate brachytherapy as a treatment option. Following that, a detailed review of the literature was presented in regards to experimental methods for performing quality assurance of the source positional and timing accuracy during treatment delivery. It concluded that while there has been much research in this area, the current state of quality assurance does not provide a comprehensive method for verifying the after-loader delivery, either for pretreatment verification or during patient treatment.

A description of the proposed HDR quality assurance system was given in Chapter 3. The prototype detector, the "Magic Plate", consisted of 121 silicon epitaxial diodes in a 2D array, coupled to the AFE DAQ system. A software tool kit, Brachy*Pix*, was designed to interact with the AFE DAQ system to perform measurements and data handling, and was also capable of real time HDR source tracking. The software featured automatic post-processing analysis, allowing for the reconstruction of the measured dwell positions and times, extracted from the source localisation results.

The feasibility of the MP for HDR quality assurance was studied in Chapter 4. The MP and AFE DAQ system exhibited a low baseline signal of 1.62 ± 1.65 pA on average. This was performed by measuring the integrated current inside the HDR treatment room, while the HDR source was inside the afterloader, with the room lights off. The source of this current was most likely generated by radio-frequency interference from the main power lines and also by the design of the AFE DAQ electronics boards. It was determined that a minimum of 50 mm of SW material above and below the MPh is necessary for backscatter material. The system was able to measure the charge generated within the MP detectors by the ^{192}Ir source over a range of 7 – 151 mm source-to-detector distance, and was found to agree with the data simulated by Taylor and Roger [28]. The MP detectors displayed an angular dependence of $\pm$ 15% between the top and bottom face of the diode, but has a less than $\pm$ 5% difference for $0 \pm 60°$ and $180 \pm 60°$.

Chapter 5 details the theory of the source localisation algorithm used in this work. The source-to-detector distances were calculated based on the response of each detector and were then compared to the geometric distance between the detector and an estimate of the source position. An iterative procedure was used to minimise the difference between the source-to-detector distances and the estimated geometric distances, until

a good agreement was found. A method for determining the dwell positions and times was presented that considered the direction of the movement of the source inside each catheter in the MPh.

The source localisation and dwell position and time calculation procedures were validated in Chapter 6. By registering EBT3 film to the MP detector and irradiating the film and detector, measured source dwell positions were compared and found to have a difference of less than 0.8 mm. It was found that using the source tracking algorithm, the HDR source transit motion could be determined and that there was a reduction in measured dwell times due to the afterloader compensating for the source movement. The MP system showed that it can be used to resolve dwell positions spaced apart by 1 mm or larger, and could be used to determine the dwell time with a 1 ms resolution, when a 1 kHz measurement frequency was used. It was also observed that, due to the size of the MP and spacing of the detectors, there was a shift in the estimated source position when close to the edge of the MP FOV.

Using the developed source tracking algorithm and an increased acquisition frequency, the instantaneous transit motion of the HDR source was characterised in Chapter 7. The transit speed was found to be non-constant, contrary to the assumptions made by the afterloader manufacturer and by some previous studies. As the TG-43U1 protocol dose calculations have been implemented into Brachy*Pix*, the transit dose was determined for the MP plane, and showed that it could be feasible to determine the additional dose to be received by the target and critical organs.

The MP, inside of the MPh, was used to verify the delivery of two HDR treatment plans in terms of dwell position and times in Chapter 8. A new metric was introduced, named the position-time gamma index, and was used to compare the measured dwell

positions and times to those expected from the treatment plan, allowing for a quick and easy assessment of the afterloader performance. For the first plan, the MP system was capable of measuring all dwell points and times and all were found to be within 0.93 mm and 0.25 s. The second plan was a modified version of the first, with simulated afterloader errors introduced to test the performance of the position-time gamma index. The gamma analysis found that all simulated dwell position and time errors with differences greater than 1.3 mm and 0.3 s, respectively, could be determined. By using The TG-43U1 protocol dose calculations based upon the measured dwell positions and times and comparing them to irradiated EBT3 film using the dose-distance gamma metric, good agreement was found between the planned and measured dose maps, when including the estimated transit dose.

Chapter 9 assessed the ability and the time taken to measure six patient plans using the MP inside of the MPh. The system was able to determine the measured dwell positions and times from the six patient plans to within 1.3 mm and 0.3 s, respectively. Using the position-time gamma analysis, the delivery of all measured patient plans were found to pass this metric with pass rates of 100%. The approach of decreasing prescription dose gave equal pass rates to the full dose plan when evaluated using the criteria. It was identified that the total time for treatment verification of the Nucletron Flexitron® HDR afterloader is dependent on the number of catheters used, and that a substantial decrease in the total time for verification could be made by reducing the prescription dose for plans containing a low number of catheters. The application of this method may have the ability to streamline pretreatment verification of the afterloader delivery within the clinical setting.

The final experimental chapter, Chapter 10, detailed the feasibility of *in-vivo* tracking of the HDR source while inside of the human body. The study focused on determining

the source position inside a water equivalent volume at large distances, and by placing materials between the HDR catheter and the MP detector. The study concluded that it could be possible to track the source inside of the body, but care was needed when deciding on detector placement, as the effects of inhomogeneous materials could be substantial.

11.2 Future Work

The concept of using a multiple diode array detector was tested for high dose rate brachytherapy quality assurance. This study showed that the prototype detector has the potential to be a comprehensive quality assurance solution, with further development and optimisations. There are a number of potential improvements that could be made to the system to increase its accuracy and usability.

The first recommended improvement is to the design of the MP diode element. The angular dependence of the epitaxial diode, while it was characterised, needed to be compensated for by the source tracking algorithm. Minimising the angular dependence, at least in the top face of the detector, could improve the reliability of the source tracking method. Another improvement that could be made to the diode element, is to increase the sensitive area of the detector. With increased area, and by applying a small reverse bias, the sensitive volume of each detector could be increased, improving the sensitivity during *in-vivo* measurements. A larger detector element area would reduce the ability to perform pinpoint measurements when used in sharp dose gradients, however, for the *in-vivo* case this should not be an issue due to the flat dose profiles.

The second recommendation is to increase the total number of diode elements and the field of view of the detector system. Current technology at the Centre for Medical Radiation Physics is utilising up to 512 detector elements in a single system, with development into systems with larger numbers. By increasing the number of detectors up to 512, the area of the MP could be quadrupled and still achieve a decrease in the detector spacing. An illustration of a possible future design is shown in Figure 11.1.

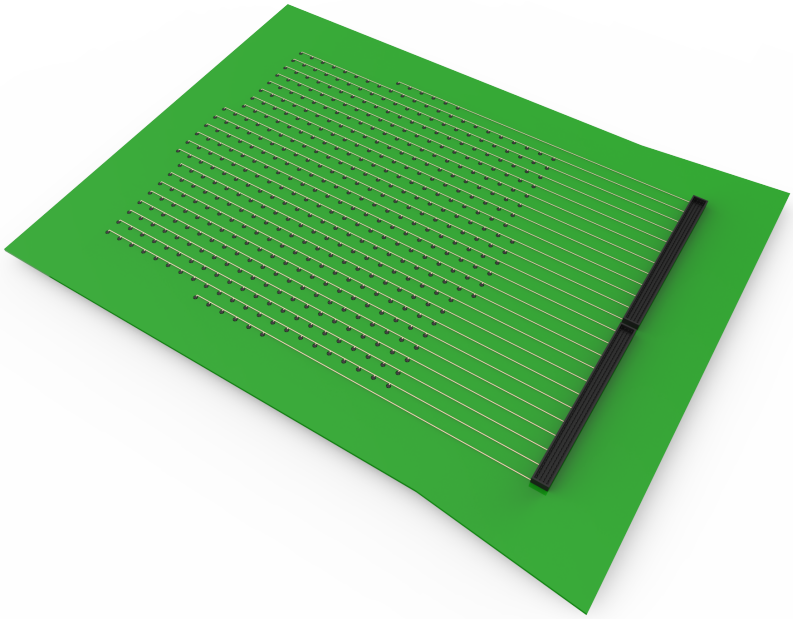

Figure 11.1: An illustration of a possible design of the HDR specific MP-512.

The larger field of view could improve the source tracking ability for the entire length of the HDR treatment catheter, and also improve the source tracking itself with increased detector redundancy. With a larger field of view, it would not be necessary to place HDR catheters beneath the MP detector. Instead, all could be placed inside of a newer designed MPh, above the MP-512 detector, again reducing the effect of the angular dependence.

The final recommendation is the further development of the Brachy*Pix* software. The

software, constructed for this study, was made to be flexible in its use and easily changeable, such as to perform TG-43U1 dose calculations or to optimise the source tracking procedure. Later versions of this software should be more targeted to be used by clinical medical physicists, by being easier to use and provide only clinically relevant results. It could feature the full integration of patient treatment plans and CT images, with 3D rendering in real time of the source position inside of the patients' tumour. Giving the clinical team the ability to see the position of the source inside of the tumour could be invaluable for *in-vivo* verification, and could potentially prevent incorrect treatments.

Bibliography

[1] Australian Institute of Health and Welfare, "Prostate cancer in Australia.," tech. rep., Australian Institute of Health and Welfare, Canberra, Australia, 2013.

[2] N. Alam, H. You, C. Banks, D. Baker, and J. F. Bishop, "Prostate Cancer in New South Wales," Tech. Rep. June, Cancer Institute NSW, Sydney, 2009.

[3] National Health and Medical Research Council, *Clinical Practice Guidelines: Evidence-based Information and Recommendations for the Management of Localised Prostate Cancer*. Canberra: NHMRC, 2002.

[4] A. A. Martinez, G. Gustafson, J. Gonzalez, E. Armour, C. Mitchell, G. Edmundson, W. Spencer, J. Stromberg, R. Huang, and F. Vicini, "Dose escalation using conformal high-dose-rate brachytherapy improves outcome in unfavorable prostate cancer," *International Journal of Radiation Oncology Biology Physics*, vol. 53, pp. 316–327, jun 2002.

[5] J. Valentin, "Prevention of high-dose-rate brachytherapy accidents. ICRP Publication 97.," *Annals of the ICRP*, vol. 35, no. 2, pp. 1–51, 2005.

[6] P. Ortiz, *Lessons learned form accidental exposures in radiotherapy.* No. 17, Vienna: IAEA, 2000.

[7] ICRP, "Prevention of accidental exposures to patients undergoing radiation therapy. A report of the International Commission on Radiological Protection.," *Annals of the ICRP*, vol. 30, no. 3, pp. 7–70, 2000.

[8] B. R. Thomadsen, B. A. Erickson, P. J. Eifel, I.-C. Hsu, R. R. Patel, D. G. Petereit, B. A. Fraass, and M. J. Rivard, "A review of safety, quality management, and practice guidelines for high-dose-rate brachytherapy: Executive summary," *Practical Radiation Oncology*, vol. 4, pp. 65–70, mar 2014.

[9] H. Okamoto, A. Aikawa, A. Wakita, K. Yoshio, N. Murakami, S. Nakamura, M. Hamada, Y. Abe, and J. Itami, "Dose error from deviation of dwell time and source position for high dose-rate 192Ir in remote afterloading system," *Journal of Radiation Research*, vol. 55, pp. 780–787, mar 2014.

[10] H. D. Kubo, G. P. Glasgow, T. D. Pethel, B. R. Thomadsen, and J. F. Williamson, "High dose-rate brachytherapy treatment delivery: report of the AAPM Radiation Therapy Committee Task Group No. 59.," *Medical Physics*, vol. 25, pp. 375–403, apr 1998.

[11] R. Nath, L. L. Anderson, J. A. Meli, A. J. Olch, J. A. Stitt, and J. F. Williamson, "Code of practice for brachytherapy physics: report of the AAPM Radiation Therapy Committee Task Group No. 56. American Association of Physicists in Medicine.," *Medical Physics*, vol. 24, no. 10, pp. 1557–1598, 1997.

[12] G. J. Kutcher, L. Coia, M. Gillin, W. F. Hanson, S. Leibel, R. J. Morton, J. R. Palta, J. A. Purdy, L. E. Reinstein, and G. K. Svensson, "Comprehensive QA

for radiation oncology: report of AAPM Radiation Therapy Committee Task Group 40.," *Medical Physics*, vol. 21, no. 4, pp. 581–618, 1994.

[13] Z. Li, T. P. Mitchell, J. R. Palta, and C. Liu, "A quality assurance test tool for high dose-rate remote afterloading brachytherapy units.," *Medical Physics*, vol. 25, pp. 232–235, feb 1998.

[14] D. W. Rickey, D. Sasaki, and J. Bews, "A quality assurance tool for high-dose-rate brachytherapy.," *Medical Physics*, vol. 37, pp. 2525–2532, jun 2010.

[15] A. Palmer, D. Bradley, and A. Nisbet, "Physics-aspects of dose accuracy in high dose rate (HDR) brachytherapy: Source dosimetry, treatment planning, equipment performance and in vivo verification techniques," *Journal of Contemporary Brachytherapy*, vol. 4, pp. 81–91, jun 2012.

[16] A. A. Espinoza, B. Beeksma, M. Petasecca, I. Fuduli, C. Porumb, D. Cutajar, S. Corde, M. Jackson, M. L. F. Lerch, and A. B. Rosenfeld, "The feasibility study and characterisation of a two dimensional diode array in "magic phantom" for high dose rate brachytherapy quality assurance .," *Medical Physics*, vol. 40, pp. 1–10, nov 2013.

[17] A. A. Espinoza, M. Petasecca, I. Fuduli, A. Howie, J. Bucci, S. Corde, M. Jackson, M. L. F. Lerch, and A. B. Rosenfeld, "The evaluation of a 2D diode array in "magic phantom" for use in high dose rate brachytherapy pretreatment quality assurance," *Medical Physics*, vol. 42, no. 2, pp. 663–673, 2015.

[18] A. A. Espinoza, M. Petasecca, D. Cutajar, I. Fuduli, A. Howie, J. Bucci, S. Corde, M. Jackson, M. Zaider, M. L. F. Lerch, and A. B. Rosenfeld, "Pretreatment verification of high dose rate brachytherapy plans using the âĂŸmagic

phantomâĂŹ system," *Biomedical Physics & Engineering Express*, vol. 1, no. 2, p. 025201, 2015.

[19] J. Ferlay, I. Soerjomataram, M. Ervik, R. Dikshit, S. Eser, C. Mathers, M. Rebelo, D. M. Parkin, D. Forman, and F. Bray, "GLOBOCAN 2012 v1.0, Cancer Incidence and Mortality Worldwide: IARC CancerBase No. 11," tech. rep., International Agency for Research on Cancer, Lyon, France, 2013.

[20] D. A. Wilkinson, "High dose rate (HDR) brachytherapy quality assurance: a practical guide.," *Biomedical imaging and intervention journal*, vol. 2, p. e34, apr 2006.

[21] S. Nag, *Principles and Practice of Brachytherapy*. Armonk, NY: Wiley-Blackwell, first edit ed., 1997.

[22] a. Challapalli, E. Jones, C. Harvey, G. O. Hellawell, and S. a. Mangar, "High dose rate prostate brachytherapy: An overview of the rationale, experience and emerging applications in the treatment of prostate cancer," *British Journal of Radiology*, vol. 85, no. SPEC. ISSUE 1, 2012.

[23] M. D. C. Evans, S. Devic, and E. B. Podgorsak, "High dose-rate brachytherapy source position quality assurance using radiochromic film," *Medical Dosimetry*, vol. 32, pp. 13–15, jan 2007.

[24] P. J. Hoskin, A. Colombo, A. Henry, P. Niehoff, T. Paulsen Hellebust, F. A. Siebert, and G. Kovacs, "GEC/ESTRO recommendations on high dose rate afterloading brachytherapy for localised prostate cancer: An update," *Radiotherapy and Oncology*, vol. 107, no. 3, pp. 325–332, 2013.

[25] *MicroSelectron HDR User Manual*. 292515ENG-00, Stockholm, Sweden: Nucletron, an Elekta company, Elekta AB.

[26] R. Van Der Laarse and Y. Niatsetski, "Flexitron and microSelectron-HDR/PDR afterloadersâĂŹ transit time and dose.," tech. rep., Stockholm, Sweden, Elekta AB, 2014.

[27] "National Nuclear Data Center, information extracted from the NuDat 2 database, http://www.nndc.bnl.gov/nudat2/ -."

[28] R. E. P. Taylor and D. W. O. Rogers, "EGSnrc Monte Carlo calculated dosimetry parameters for 192Ir and 169Yb brachytherapy sources.," *Medical Physics*, vol. 35, no. 11, pp. 4933–4944, 2008.

[29] J. A. Meli, A. S. Meigooni, and R. Nath, "On the choice of phantom material for the dosimetry of 192Ir sources.," *International journal of radiation oncology, biology, physics*, vol. 14, pp. 587–594, mar 1988.

[30] R. Nath, L. L. Anderson, G. Luxton, K. A. Weaver, J. F. Williamson, and A. S. Meigooni, "Dosimetry of interstitial brachytherapy sources: recommendations of the AAPM Radiation Therapy Committee Task Group No. 43. American Association of Physicists in Medicine.," *Medical Physics*, vol. 22, no. 2, pp. 209–234, 1995.

[31] M. J. Rivard, B. M. Coursey, L. A. DeWerd, W. F. Hanson, M. S. Huq, G. S. Ibbott, M. G. Mitch, R. Nath, and J. F. Williamson, "Update of AAPM Task Group No. 43 Report: A revised AAPM protocol for brachytherapy dose calculations.," *Medical Physics*, vol. 31, no. 3, pp. 633–674, 2004.

[32] L. Beaulieu, A. Carlsson Tedgren, J.-F. Carrier, S. D. Davis, F. Mourtada, M. J. Rivard, R. M. Thomson, F. Verhaegen, T. A. Wareing, and J. F. Williamson, "Report of the Task Group 186 on model-based dose calculation methods in

brachytherapy beyond the TG-43 formalism: Current status and recommendations for clinical implementation," *Medical Physics*, vol. 39, p. 6208, oct 2012.

[33] M. J. Rivard, J. L. M. Venselaar, and L. Beaulieu, "The evolution of brachytherapy treatment planning.," *Medical Physics*, vol. 36, no. 6, pp. 2136–2153, 2009.

[34] United States Nuclear Regulatory Commission, "Loss of an Iridium-192 Source and Therapy Misadministration at Indiana Regional Cancer Center, Indiana, Pennsylvania on November 16, 1992," tech. rep., United States Nuclear Regulatory Commission, Washington, D.C, 1993.

[35] C. Dempsey, R. Smith, T. Nyathi, A. Ceylan, L. Howard, V. Patel, R. Das, and A. Haworth, "ACPSEM brachytherapy working group recommendations for quality assurance in brachytherapy," *Australasian Physical and Engineering Sciences in Medicine*, vol. 36, no. 4, pp. 387–396, 2013.

[36] J. Venselaar and J. Pérez-Calatayud, *A practical guide to quality control of brachytherapy equipment*, vol. 8. 2004.

[37] A. Palmer and B. Mzenda, "Performance assessment of the BEBIG MultiSource high dose rate brachytherapy treatment unit.," *Physics in medicine and biology*, vol. 54, no. 24, pp. 7417–7434, 2009.

[38] P. Pittet, P. Jalade, J. Balosso, L. Gindraux, P. Guiral, R. Wang, A. Chaikh, A. Gaudu, J. Ribouton, J. Rousseau, J.-M. Galvan, A. Rivoire, J.-Y. Giraud, and G.-N. Lu, "Dosimetry systems based on Gallium Nitride probe for radiotherapy, brachytherapy and interventional radiology," *IRBM*, vol. 36, no. 2, pp. 92–100, 2015.

[39] M. D. C. Evans, C. l. J. Arsenault, and M. B. Podgorsak, "Quality assurance for variable-length catheters with an afterloading brachytherapy device.," *Medical Physics*, vol. 20, no. 1, pp. 251–253, 1993.

[40] D. Sheikh-Bagheri and P. Munro, "A Monte Carlo study of verification imaging in high dose rate brachytherapy.," *Medical Physics*, vol. 25, no. 4, pp. 404–414, 1998.

[41] J. Duan, D. J. Macey, P. N. Pareek, and I. A. Brezovich, "Real-time monitoring and verification of in vivo high dose rate brachytherapy using a pinhole camera.," *Medical Physics*, vol. 28, no. 2, pp. 167–173, 2001.

[42] T. Nakano, N. Suchowerska, M. M. Bilek, D. R. McKenzie, N. Ng, and T. Kron, "High dose-rate brachytherapy source localization: positional resolution using a diamond detector.," *Physics in medicine and biology*, vol. 48, pp. 2133–2146, jul 2003.

[43] T. Nakano, N. Suchowerska, D. R. McKenzie, and M. M. Bilek, "Real-time verification of HDR brachytherapy source location: implementation of detector redundancy.," *Physics in medicine and biology*, vol. 50, pp. 319–327, jan 2005.

[44] L. Liu, S. C. Prasad, D. A. Bassano, J. Heavern, B. Keshler, and S. S. Hahn, "A dwell position verification method for high dose rate brachytherapy.," *Journal of applied clinical medical physics / American College of Medical Physics*, vol. 5, no. 1, pp. 1–5, 2004.

[45] P. Kohr and F.-A. Siebert, "Quality assurance of brachytherapy afterloaders using a multi-slit phantom.," *Physics in medicine and biology*, vol. 52, pp. N387–N391, sep 2007.

[46] H. Song, J. Bowsher, S. Das, and F.-F. Yin, "Tracking brachytherapy sources using emission imaging with one flat panel detector.," *Medical Physics*, vol. 36, no. 4, pp. 1109–1111, 2009.

[47] J. Lambert, D. R. McKenzie, S. Law, J. Elsey, and N. Suchowerska, "A plastic scintillation dosimeter for high dose rate brachytherapy.," *Physics in medicine and biology*, vol. 51, pp. 5505–5516, nov 2006.

[48] H. Kojima, T. Hanada, S. Katsuta, A. Yorozu, and K. Maruyama, "New method for obtaining position and time structure of source in HDR remote afterloading brachytherapy unit utilizing light emission from scintillator.," *Journal of applied clinical medical physics / American College of Medical Physics*, vol. 10, p. 2983, jan 2009.

[49] C. E. Andersen, S. K. Nielsen, S. Greilich, J. Helt-Hansen, J. C. Lindegaard, and K. Tanderup, "Characterization of a fiber-coupled Al2O3:C luminescence dosimetry system for online in vivo dose verification during 192Ir brachytherapy.," *Medical Physics*, vol. 36, no. 3, pp. 708–718, 2009.

[50] M. Batič, J. Burger, V. Cindro, G. Kramberger, I. Mandić, M. Mikuž, A. Studen, and M. Zavrtanik, "A system for localization of high dose rate 192Ir source during brachytherapy treatment with silicon detectors," in *IEEE Nuclear Science Symposium Conference Record*, pp. 3794–3800, IEEE, oct 2009.

[51] F. Therriault-Proulx, T. M. Briere, F. Mourtada, S. Aubin, S. Beddar, and L. Beaulieu, "A phantom study of an in vivo dosimetry system using plastic scintillation detectors for real-time verification of 192Ir HDR brachytherapy.," *Medical Physics*, vol. 38, no. 5, pp. 2542–2551, 2011.

[52] G. Kertzscher, C. E. Andersen, F. A. Siebert, S. K. Nielsen, J. C. Lindegaard, and K. Tanderup, "Identifying afterloading PDR and HDR brachytherapy errors using real-time fiber-coupled Al 2O 3:C dosimetry and a novel statistical error decision criterion," *Radiotherapy and Oncology*, vol. 100, pp. 456–462, sep 2011.

[53] G. Kertzscher, C. E. Andersen, and K. Tanderup, "Adaptive error detection for HDR/PDR brachytherapy: Guidance for decision making during real-time in vivo point dosimetry.," *Medical Physics*, vol. 41, p. 052102, may 2014.

[54] A. Manikandan, S. Biplab, P. A. David, R. Holla, T. R. Vivek, and N. Sujatha, "Relative dosimetrical verification in high dose rate brachytherapy using two-dimensional detector array IMatriXX.," *Journal of medical physics / Association of Medical Physicists of India*, vol. 36, no. 3, pp. 171–175, 2011.

[55] M. Safavi-Naeini, Z. Han, D. Cutajar, S. Guatelli, M. Petasecca, M. L. F. Lerch, D. R. Franklin, J. Jakubek, S. Pospisil, J. Bucci, M. Zaider, and A. B. Rosenfeld, "BrachyView, a novel inbody imaging system for HDR prostate brachytherapy: design and Monte Carlo feasibility study.," *Medical Physics*, vol. 40, no. 7, pp. 1–10, 2013.

[56] M. Petasecca, K. J. Loo, M. Safavi-Naeini, Z. Han, P. E. Metcalfe, S. Meikle, S. Pospisil, J. Jakubek, J. Bucci, M. Zaider, M. L. F. Lerch, Y. Qi, and A. B. Rosenfeld, "BrachyView: proof-of-principle of a novel in-body gamma camera for low dose-rate prostate brachytherapy.," *Medical Physics*, vol. 40, no. 4, p. 041709, 2013.

[57] J. Dammer, P. M. Frallicciardi, J. Jakubek, M. Jakubek, S. Pospisil, E. Prenerova, D. Vavrik, L. Volter, F. Weyda, and R. Zemek, "Real-time in-vivo μ-imaging with Medipix2," *Nuclear Instruments and Methods in Physics Research,*

Section A: Accelerators, Spectrometers, Detectors and Associated Equipment, vol. 607, no. 1, pp. 205–207, 2009.

[58] Z. Han, M. Safavi-Naeini, S. Alnaghy, D. Cutajar, S. Guatelli, M. Petasecca, D. Franklin, A. Malaroda, M. Carrara, J. Bucci, M. Zaider, M. L. F. Lerch, and A. B. Rosenfeld, "Radiation dose enhancement at tissue-tungsten interfaces in HDR brachytherapy," *Physics in Medicine and Biology*, vol. 59, no. 21, pp. 6659–6659, 2014.

[59] M. Safavi-Naeini, Z. Han, D. Cutajar, S. Guatelli, M. Petasecca, M. Lerch, D. Franklin, J. Bucci, M. Zaider, and A. Rosenfeld, "BrachyView, A novel in-body imaging system for HDR prostate brachytherapy: Experimental evaluation," *Medical Physics*, no. Accepted 16/9/2015, 2015.

[60] R. L. Smith, M. L. Taylor, L. N. McDermott, A. Haworth, J. L. Millar, and R. D. Franich, "Source position verification and dosimetry in HDR brachytherapy using an EPID.," *Medical Physics*, vol. 40, p. 111706, nov 2013.

[61] R. Wang, J. Ribouton, P. Pittet, P. Guiral, P. Jalade, and G. N. Lu, "Implementation of GaN based real-time source position monitoring in HDR brachytherapy," *Radiation Measurements*, pp. 2–5, may 2014.

[62] P. A. Jursinic, "Quality assurance measurements for high-dose-rate brachytherapy without film," *Journal of Applied Clinical Medical Physics*, vol. 15, pp. 246–261, jan 2014.

[63] K. T. Bastin, M. B. Podgorsak, and B. R. Thomadsen, "The transit dose component of high dose rate brachytherapy: direct measurements and clinical implications.," *International journal of radiation oncology, biology, physics*, vol. 26, pp. 695–702, jul 1993.

[64] P. V. Houdek, J. G. Schwade, X. Wu, V. Pisciotta, J. A. Fiedler, C. F. Serago, A. M. Markoe, A. A. Abitbol, A. A. Lewin, and P. G. Braunschweiger, "Dose determination in high dose-rate brachytherapy.," *International journal of radiation oncology, biology, physics*, vol. 24, pp. 795–801, jan 1992.

[65] N. Sahoo, "Measurement of transit time of a remote after-loading high dose rate brachytherapy source.," *Medical Physics*, vol. 28, no. 8, pp. 1786–1790, 2001.

[66] T. P. Wong, W. Fernando, P. N. Johnston, and I. F. Bubb, "Transit dose of an Ir-192 high dose rate brachytherapy stepping source.," *Physics in medicine and biology*, vol. 46, pp. 323–331, feb 2001.

[67] G. P. Fonseca, R. S. S. Viana, M. Podesta, R. A. Rubo, C. P. de Sales, B. Reniers, H. Yoriyaz, and F. Verhaegen, "HDR 192Ir source speed measurements using a high speed video camera," *Medical Physics*, vol. 42, no. 1, pp. 412–415, 2015.

[68] R. A. Minamisawa, R. A. Rubo, R. M. Seraide, J. R. O. Rocha, and A. Almeida, "Direct measurement of instantaneous source speed for a HDR brachytherapy unit using an optical fiber based detector.," *Medical Physics*, vol. 37, no. 10, pp. 5407–5411, 2010.

[69] G. P. Fonseca, R. A. Rubo, R. A. Minamisawa, G. R. dos Santos, P. C. G. Antunes, and H. Yoriyaz, "Determination of transit dose profile for a (192)Ir HDR source.," *Medical Physics*, vol. 40, p. 051717, may 2013.

[70] G. P. Fonseca, G. Landry, B. Reniers, A. Hoffmann, R. A. Rubo, P. C. G. Antunes, H. Yoriyaz, and F. Verhaegen, "The contribution from transit dose for (192)Ir HDR brachytherapy treatments.," *Physics in medicine and biology*, vol. 59, pp. 1831–44, apr 2014.

[71] M. Petasecca, A. Cullen, I. Fuduli, A. A. Espinoza, C. Porumb, C. Stanton, a. H. Aldosari, E. Bräuer-Krisch, H. Requardt, A. Bravin, V. Perevertaylo, a. B. Rosenfeld, and M. L. F. Lerch, "X-Tream: a novel dosimetry system for Synchrotron Microbeam Radiation Therapy," *Journal of Instrumentation*, vol. 7, pp. P07022–P07022, jul 2012.

[72] G. F. Knoll, *Radiation Detection and Measurement*. New York, NY, USA: John Wiley & Sons, third edit ed., 2010.

[73] G. Lutz, "Silicon radiation detectors," *Nuclear Instruments and Methods in Physics Research Section A: Accelerators, Spectrometers, Detectors and Associated Equipment*, vol. 367, no. 1-3, pp. 21–33, 1995.

[74] G. Rikner and E. Grusell, "Effects of radiation damage on p-type silicon detectors," *Physics in Medicine and Biology*, vol. 28, pp. 1261–1267, nov 2000.

[75] F. H. Attix, *Introduction to Radiological Physics and Radiation Dosimetry*. John Wiley & Sons, 2008.

[76] A. B. Rosenfeld, "Electronic dosimetry in radiation therapy," *Radiation Measurements*, vol. 41, pp. S134–S153, dec 2006.

[77] J. H. Hubbell and S. M. Seltzer, "Tables of X-Ray Mass Attenuation Coefficients and Mass Energy-Absorption Coefficients from 1 keV to 20 MeV for Elements Z = 1 to 92 and 48 Additional Substances of Dosimetric Interest," 2004.

[78] M. Moll, *Radiation Damage in Silicon Detectors*. PhD thesis, Hamburg University, 1999.

[79] M. Bruzzi, M. Bucciolini, M. Casati, D. Menichelli, C. Talamonti, C. Piemonte, and B. G. Svensson, "Epitaxial silicon devices for dosimetry applications," *Applied Physics Letters*, vol. 90, no. 17, p. 172109, 2007.

[80] S. M. Sze and K. K. Ng, "Physics of Semiconductor Devices, 3rd Edition - Simon M. Sze, Kwok K. Ng," in *Physics of Semiconductor Devices, 3rd Edition.; John Wiley & Sons, Inc.; NJ*, pp. 164, 682, 2007.

[81] J. H. D. Wong, I. Fuduli, M. Carolan, M. Petasecca, M. L. F. Lerch, V. L. Perevertaylo, P. Metcalfe, and A. B. Rosenfeld, "Characterization of a novel two dimensional diode array the "magic plate" as a radiation detector for radiation therapy treatment," *Medical Physics*, vol. 39, no. 5, p. 2544, 2012.

[82] I. S. Kwan, D. Wilkinson, D. Cutajar, M. Lerch, a. Rosenfeld, a. Howie, J. Bucci, Y. Chin, and V. L. Perevertaylo, "The effect of rectal heterogeneity on wall dose in high dose rate brachytherapy," *Medical Physics*, vol. 36, no. 1, p. 224, 2009.

[83] A. H. Aldosari, A. A. Espinoza, D. Robinson, I. Fuduli, C. Porumb, S. Alshaikh, M. Carolan, M. L. F. Lerch, V. Perevertaylo, A. B. Rosenfeld, and M. Petasecca, "Characterization of an innovative p-type epitaxial diode for dosimetry in modern external beam radiotherapy," *IEEE Transactions on Nuclear Science*, vol. 60, pp. 4705–4712, dec 2013.

[84] I. Fuduli, M. Newall, A. Espinoza, C. Porumb, M. Carolan, M. Lerch, P. Metcalfe, A. Rosenfeld, and M. Petasecca, "Multichannel Data Acquisition System comparison for Quality Assurance in external beam radiation therapy," *Radiation Measurements*, vol. 71, pp. 338–341, dec 2014.

[85] I. Fuduli, C. Porumb, A. A. Espinoza, A. H. Aldosari, M. Carolan, M. L. F. Lerch, P. Metcalfe, A. B. Rosenfeld, and M. Petasecca, "A comparative analysis of multichannel Data Acquisition Systems for quality assurance in external beam radiation therapy," *Journal of Instrumentation*, vol. 9, pp. T06003–T06003, jun 2014.

[86] D. Granero, J. Pérez-Calatayud, E. Casal, F. Ballester, and J. Venselaar, "A dosimetric study on the Ir-192 high dose rate flexisource.," *Medical Physics*, vol. 33, no. 12, pp. 4578–4582, 2006.

[87] A. L. Palmer, A. Nisbet, and D. A. Bradley, "Semi-3D dosimetry of high dose rate brachytherapy using a novel Gafchromic EBT3 film-array water phantom," *Journal of Physics: Conference Series*, vol. 444, p. 012101, jun 2013.

[88] T. A. D. Brown, K. R. Hogstrom, D. Alvarez, K. L. Matthews, K. Ham, and J. P. Dugas, "Dose-response curve of EBT, EBT2, and EBT3 radiochromic films to synchrotron-produced monochromatic x-ray beams," *Medical Physics*, vol. 39, p. 7412, dec 2012.

[89] G. Massillon-JL, S.-T. Chiu-Tsao, I. Domingo-Munoz, and M. F. Chan, "Energy Dependence of the New Gafchromic EBT3 Film:Dose Response Curves for 50 KV, 6 and 15 MV X-Ray Beams," *International Journal of Medical Physics, Clinical Engineering and Radiation Oncology*, vol. 01, no. 02, pp. 60–65, 2012.

[90] L. A. DeWerd, G. S. Ibbott, A. S. Meigooni, M. G. Mitch, M. J. Rivard, K. E. Stump, B. R. Thomadsen, and J. L. M. Venselaar, "A dosimetric uncertainty analysis for photon-emitting brachytherapy sources: report of AAPM Task Group No. 138 and GEC-ESTRO.," *Medical Physics*, vol. 38, no. 2, pp. 782–801, 2011.

[91] M. Westermark, J. Arndt, B. Nilsson, and A. Brahme, "Comparative dosimetry in narrow high-energy photon beams," *Physics in Medicine and Biology*, vol. 45, pp. 685–702, mar 2000.

[92] P. A. Jursinic, "Angular dependence of dose sensitivity of surface diodes.," *Medical Physics*, vol. 36, no. 6, pp. 2165–2171, 2009.

[93] A. B. Rosenfeld and M. Zaider, "Method and apparatus for real time dosimetry, Patent: 7,361,134," 2008.

[94] A. B. Rosenfeld and M. Zaider, "Method and apparatus for real time dosimetry, Patent: 7,972,259," 2011.

[95] P. L. DeVries, *A First Course in Computational Physics*. New York, NY, USA: John Wiley & Sons, 1st ed., 1993.

[96] D. A. Low, W. B. Harms, S. Mutic, and J. A. Purdy, "A technique for the quantitative evaluation of dose distributions.," *Medical Physics*, vol. 25, pp. 656–661, may 1998.

[97] *Oncentra MasterPlan v3.2, Physics and Algorithms Manual*. 192.739ENG-02, Stockholm, Sweden: Nucletron, an Elekta company, Elekta AB.

[98] *Image Guided Brachytherapy - Zephyr HDR Patient Positioning and Transfer System*. http://diacorinc.com/transfer/Zephyr_HDR, date accessed 02/09/2015.

[99] ICRP, "Basic anatomical and physiological data for use in radiological protection - the skeleton. ICRP Publication 70," *Annals of the ICRP*, vol. 25, no. 2, pp. 1–80, 1995.

[100] M. Berger, J. Coursey, M. Zucker, and J. Chang, *Stopping-Power and Range Tables for Electrons, Protons, and Helium Ions*. http://www.nist.gov/pml/data/star/, 2005.

[101] M. L. Taylor, R. L. Smith, F. Dossing, and R. D. Franich, "Robust calculation of effective atomic numbers: The Auto-Zeff software," *Medical Physics*, vol. 39, no. 4, p. 1769, 2012.